HPP Lattice-Gas Automata for Computational Electromagnetics

by

Dino Cule

A thesis
presented to the University of Manitoba
in fulfilment of the
thesis requirement for the degree of
Master of Science
in
Electrical Engineering

Winnipeg, Manitoba, Canada 1998

THE UNIVERSITY OF MANITOBA

FACULTY OF GRADUATE STUDIES

*****

COPYRIGHT PERMISSION PAGE

HPP LATTICE-GAS AUTOMATA FOR COMPUTATIONAL ELECTROMAGNETICS

BY

DINO CULE

A Thesis/Practicum submitted to the Faculty of Graduate Studies of The University of Manitoba in partial fulfillment of the requirements of the degree of

MASTER OF SCIENCE

Abstract

A Lattice-Gas Automaton (LGA) is an unconditionally stable discrete system in which particles with a small and finite number of states move about on a regular lattice. The dynamics of this system are governed by a reversible and deterministic rule which is applied to the entire system simultaneously. An LGA is a discreet approximation to molecular dynamics. This study was partially motivated by the possibility of exploiting alternative computer architectures.

Using a two-dimensional HPP-LGA model, electromagnetic fields in homogeneous and inhomogeneous media have been simulated on a special-purpose computing device, referred to as a Cellular Automata Machine (CAM-8). The quantitative analysis of an HPP-LGA absorbing boundary condition is presented. Quantitative numerical results for scattering of electric fields from various homogeneous and inhomogeneous regions are provided. For most simulations, comparisons with the Symmetric-Condensed Transmission-Line method (TLM) or analytical solutions are provided. An example of the possible application of HPP-LGA to the analysis of electromagnetic wave interaction with biological media is submitted.

Acknowledgements

I would like to thank the following:

Professor Greg Bridges for his patience, guidance and faith throughout this research. The staff of the electrical engineering department were particularly helpful during times of great panic.

The staff of the (former) Directorate of Antennas and Integrated Electronics at the Communications Research Centre. Although most had little to do with the actual research concerning this thesis, they often provided illuminating and thought-provoking discussions. I would like to thank Neil Simons for his guidance and supervision during my (lengthy) stay at CRC, and Wilf Lauber for his understanding and use of facilities.

Grad students of various forms and states of completion. I would like to thank those who have completed (Mark, Elvis, Nikhil) for paving a path and proving that it can indeed be done, those who are about to finish (Jeff, Krista, Dave, Paul, Riaz, Ming) because misery loves company, and those who have fallen by the wayside (Tim, Kevin, Cam) for keeping everything in perspective.

Special shouts go out to Paul Godavari for *jobs, beer, chicks and stuff*, Nikhil Adnani for the phat beats and encouragement, Gary Gray for long distance roots, and Tim Dickinson for showing me how to keep it real, east-coast style.

My family: my mother, father and sister for faith and understanding. Most importantly I would like to thank my wife Kerry, who at times must have felt like a widow. Her assistance in the final edit of the system (during the late evening of her birthday) was wonderful.

Contents

List of Figures

List of Tables

Chapter 1

Introduction

1.1 Lattice-Gas Automata

A Lattice-Gas Automaton (LGA) is a system in which particles with a small and finite number of states move about on a regular lattice, with their dynamics governed by a deterministic and reversible rule. This rule is applied to the entire system simultaneously, and is most efficiently implemented on a parallel architecture [1]. An LGA can be considered a discrete approximation of molecular dynamics. Already in use in the field of fluid mechanics and physics [2], LGAs have begun to be applied to the modelling of two-dimensional electromagnetic field problems, as demonstrated in [3].

In contrast to traditional floating-point differential-equation based approaches to the modelling of electromagnetic fields, such as Finite-Difference Time-Domain (FDTD) [4] or Transmission-Line (TLM) [5] methods, LGAs use only a few bytes of memory per cell and simple binary logic to manipulate information, without any loss of information due to numerical roundoff. This fundamental difference results in, among other things, unconditionally stable behavior.

Two-dimensional electromagnetic wave phenomena can be described by the linear wave equation with the application of appropriate boundary conditions and sources. A fluid encompasses linear wave behavior, and therefore a system which is capable of simulating a fluid can also be used to simulate electromagnetics in two dimensions. The Navier-Stokes equation, used to describe fluid flow, can therefore be used as a foundation for the simulations of electromagnetics in two dimensions.

1.2 CAM-8

This study into the feasibility of HPP-LGA[1] for the modelling of electromagnetic fields was motivated by a desire to use an alternative computational architecture. The evolution of parallel computers has not matched the rate of development of serial machines. Additionally, conventional computers are not optimized for the simulation of LGA systems. Therefore the possible application of various LGA methods to computational physics problems has not been studied.

Simulations in this thesis were conducted on a special-purpose computing device called the CAM-8. Developed by the Information Mechanics Group at the Massachusetts Institute of Technology, the CAM-8 is a parallel computer ideally suited for Lattice-Gas simulations. Although CAM is an abbreviation for "Cellular Automata Machine", the CAM-8 is more accurately described as a lattice-gas machine.

The CAM-8 was developed using early 1990's electronic technology which can be found in low-end workstations. The core of the computer is comprised of a system clock derrived from a workstation, and 66 Megabytes of RAM (64 Megabytes DRAM, 2 Megabytes SRAM). The lattice portion of the LGA is resident in the DRAM. The lattice is assigned an overall size and shape, number of bits per site, and number

[1] Named after it's inventors: Hardy, Pazzis and Pomeau [6]

of dimensions. Updating of the lattice mimics the evolution of the lattice through the use of a lookup table stored in the SRAM. Data comes out of the lattice, passes through the lookup table, and the result is then routed back to the exact location in the lattice. Data is then propagated in the necessary direction. A CAM-8 update schematic is presented in Figure 1.1.

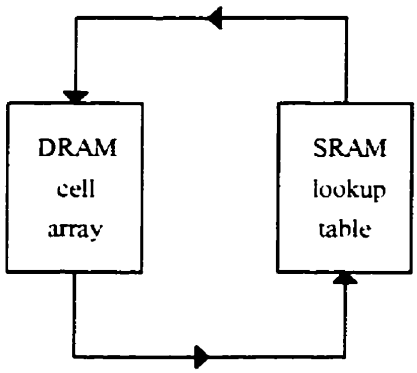

Figure 1.1: CAM-8 system update schematic

The CAM-8 can run simulations at a rate of about 3 billion cell updates per second on spaces of up to half a billion cells with a single bit per cell; with 16 bits per cell, simulations run at about 200 million site updates per second on spaces of up to 32 million cells. As of 1993, the performance of the CAM-8 was equal or better than that of serial supercomputers [1].

1.3 Summary

This thesis is in many ways a continuation of Nikhil Adnani's M.Sc. thesis "Cellular Automata Models for the Two Dimensional Scalar Wave Equation" [7]. Although a prior knowledge of Adnani's work is useful, comparisons have been kept to a minimum.

The remainder of this thesis is broken into four chapters. The first chapter deals

with the theory describing the dynamics of the HPP-LGA model. It begins by describing the standard HPP-LGA model, and moves on to explain the changes which were made to it in order to model dielectric materials. The next two chapters deal with the application of HPP-LGA to the simulation of two-dimensional electromagnetic phenomena. The scattering of electric fields by homogeneous and inhomogeneous dielectric regions is predicted in order to validate the presented theory. The HPP-LGA method is extended to the prediction of field distributions inside a dielectric cylinder, and then to the interaction of electromagnetic waves with biological media. The thesis concludes with a summary of the major developments and recommendations for future study.

Chapter 2

Lattice Gas Automata

A Lattice-Gas Automaton (LGA) is a system in which particles with a small and finite number of states move about on a regular lattice, with their dynamics governed by a deterministic and reversible rule. This rule is applied to the entire system simultaneously. An LGA can be considered a discrete approximation to molecular dynamics.

This chapter will focus on the HPP-LGA model in two dimensions and the modifications that have been made in order to model dielectric media. Improvements over the Adnani [7] rest particle model, which allows for the modelling of higher values of ϵ_r in a more efficient manner are presented. Differences between the two models are described briefly in this chapter.

The first part of the chapter deals with the general concept of HPP-LGA and the relationship between microscopic particle dynamics, fluid flow and electromagnetics. The second part provides details regarding the initialization of HPP-LGA lattices, the dynamics of the two classes of rest-particles and the manner in which they are used to simulate discrete propagation speeds. The ability to model a wide range of propagation speeds is introduced through the concept of rest-particle mixing.

2.1 HPP-LGA Overview

2.1.1 Standard HPP-LGA Model

The standard HPP-LGA model in two dimensions consists of cells, or sites, which are located on a regular cartesian lattice. These cells are connected by four links[1] upon which particles of mass m propagate. The cells themselves can hold up to four moving particles which obey an exclusion principle: there can be no more than one particle for each direction. A cell has a total of 2^4 possible states which it can be in at any time.

The dynamics of the system are governed by a simple rule which, at each timestep, conserves mass and momentum at a cellular level. The HPP-LGA rule states that a particle will propagate in its respective direction unless it collides with an isolated particle propagating in the opposite direction. When collision occurs the two particles are scattered orthogonally. Figure 2.1 illustrates two cases of particles streaming, where by convention north is at the top of the lattice. Cells are represented by squares and particles by filled circles.

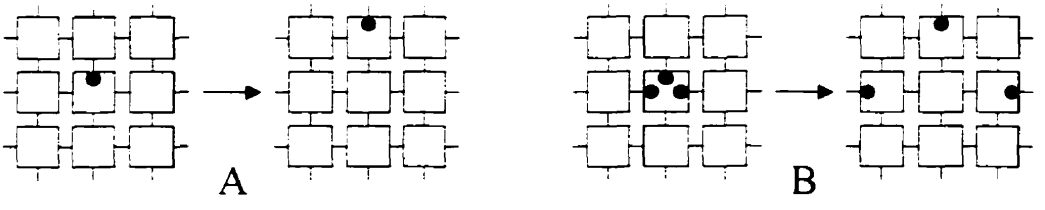

Figure 2.1: HPP-LGA rule: particle streaming

In Figure 2.1, example **A** shows a particle moving north from one cell to another, while example **B** shows three particles colliding but not scattering. Particle interac-

[1] North, south, east and west.

tion is introduced with the HPP-LGA collision as shown in Figure 2.2. In Figure 2.2, an east and west moving particle collide giving rise to north and south moving particles. In a similar manner, a collision between a north and south moving particle would produce east and west moving particles.

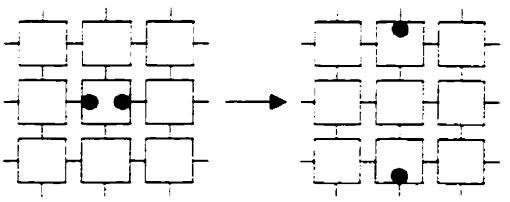

Figure 2.2: Standard HPP-LGA collision

Without the head-on collision, a single lattice could be decomposed into two lattices with particles moving in the x and y directions independent of each other. The HPP-LGA collision, while not necessary for the conservation of mass and momentum on a cellular level, couples these two lattices through the transfer of energy. Moreover, the trivial rule consisting of simple particle streaming yields no significant insight into wave propagation.

Movement of particles through the lattice actually takes place over two separate steps: *collision* and *advection*. In the *collision* stage, cells are examined for local particle interactions, and the HPP-LGA collision is applied as necessary. In the *advection* stage, particles are passed to the neighboring cells. The two step process is shown in Figure 2.3.

Figure 2.3 shows the states of the moving particles in a lattice of 16 HPP-LGA cells. The initial states are shown in **A**, and in **B** the particles within the cells are manipulated according to the HPP-LGA rule as previously shown in Figure 2.2. Finally, the particles are propagated in their appropriate directions as shown in **C**. The aforementioned HPP-LGA collision takes place in the highlighted cell, located

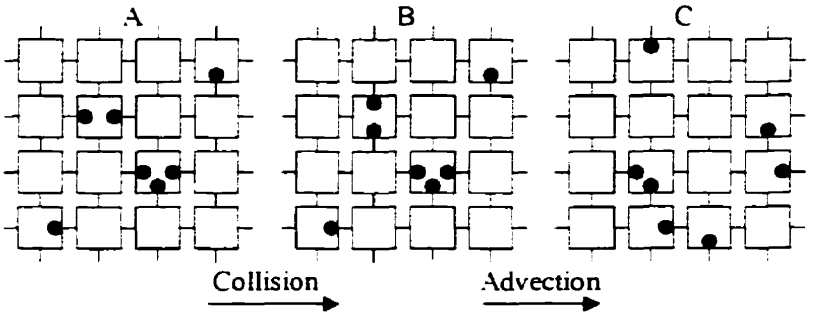

Figure 2.3: HPP-LGA collision and advection

in the upper left corner of the lattice.

At this point a common misconception on the relationship between LGAs and Cellular Automatons (CA) can be clarified. Although commonly associated with CAs, LGAs are not a natural extension of this method. To summarize [8], evolution in CAs takes place through a series of generations, where the state of a cell is a function of the state of itself and of its neighbors in the previous generation. In this manner, a CA proceeds from generation to generation in single steps. This contrasts with LGAs, which as described earlier are defined in a two step collision/advection sense.

> A confusion of the two fields distorts our thinking, hiding the special properties of lattice gases, and makes it harder to develop a good intuition.
> *M. Hénon*

2.1.2 HPP-LGA Dynamics

Two-dimensional electromagnetic wave phenomena can be described by the linear scalar wave equation with the application of appropriate boundary conditions and sources. A fluid encompasses linear wave behavior, and therefore a system which is

capable of simulating a fluid can also be used to simulate electromagnetics in two dimensions. The two-dimensional Navier-Stokes equation (Equation 2.1 [9]) together with the continuity equation[2] (Equation 2.2) can be used to model a fluid, where ρ is the density, $\mathbf{u}$ is the flow velocity, p is the pressure, and η, ζ are the shear and bulk viscosities [10].

$$\frac{\partial}{\partial t}\rho\mathbf{u} + \rho(\mathbf{u}\cdot\nabla)\mathbf{u} = -\nabla p + \eta\nabla^2\mathbf{u} + (\zeta + \frac{\eta}{2})\nabla(\nabla\cdot\mathbf{u}) \tag{2.1}$$

$$\frac{\partial\rho}{\partial t} + \nabla\cdot(\rho\mathbf{u}) = 0 \tag{2.2}$$

For isothermal flow and low flow velocity $\mathbf{u}$, the pressure and density can be related by Equation 2.3, where c_s is the propagation velocity for sound waves [9].

$$p = c_s^2\rho \tag{2.3}$$

For equilibrium distributions with $\mathbf{u} \to 0$ and small perturbations to a uniform background density ρ_0, (ie. $\rho = \rho_0 + \rho_{small}$), the non-linear and viscous terms in Equation 2.1 can be neglected, yielding the linear wave equation for ρ_{small} as shown in Equation 2.4. Equation 2.4 can also be expressed as a small perturbation of the pressure or velocity.

$$\nabla^2\rho_{small} = \frac{1}{c_s^2}\frac{\partial^2\rho_{small}}{\partial t^2} \tag{2.4}$$

The HPP-LGA method only approximates the Navier-Stokes equation. The FHP-LGA, which uses a hexagonal lattice, can simulate the Navier-Stokes equation exactly [11].

[2] Also a statement of the conservation of mass.

Assuming $e^{-j\omega t}$ time dependence, a two-dimensional time-harmonic plane wave can be expressed in the form:

$$A \exp(jk_x x + jk_y y) \tag{2.5}$$

where (k_x, k_y) are components of the propagation vector $\mathbf{k}$ as shown in Figure 2.4 and A is an arbitrary constant. The vector $\mathbf{k}$ incorporates the wavelength of the propagating wave through its magnitude ($|\mathbf{k}| = \frac{2\pi}{\lambda} = \frac{\omega}{c}$) and the direction of the wave o. From Figure 2.4, the propagation components are defined as:

$$k_x = |\mathbf{k}| \cos o, \quad k_y = |\mathbf{k}| \sin o \tag{2.6}$$

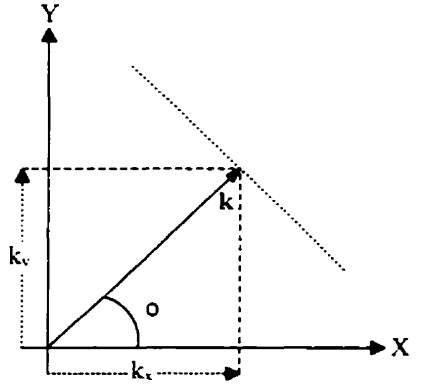

Figure 2.4: Propagation vector definition

The pressure fields of Figure 2.5 can be expressed in the form of Equation 2.5, resulting in Equations 2.7 - 2.9. The constants A, B and C are dependent on the properties of the respective media, and the subscripts i, r and t refer to the incident, reflected and transmitted waves.

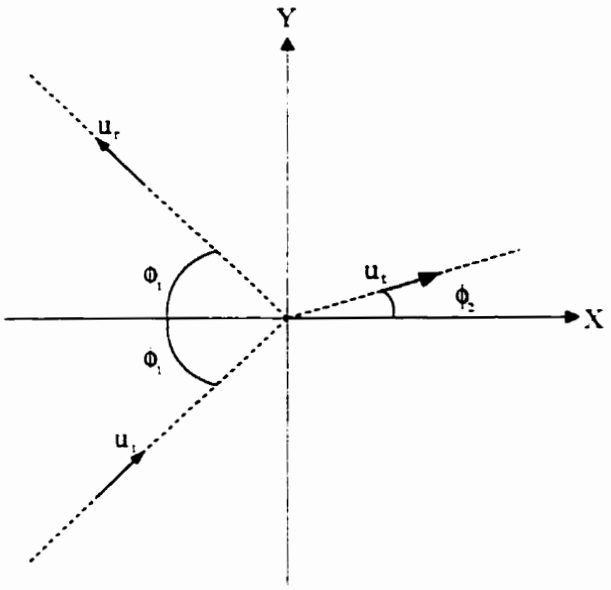

Figure 2.5: Reflection of an acoustic wave at a boundary

$$p_i = A \exp(j\, k_{1x}\, x + j\, k_{1y}\, y) \tag{2.7}$$

$$p_r = B \exp(-j\, k_{1x}\, x + j\, k_{1y}\, y) \tag{2.8}$$

$$p_t = C \exp(j\, k_{2x}\, x + j\, k_{2y}\, y) \tag{2.9}$$

The reflection and transmission coefficients Γ and τ are defined in terms of the wave impedances ($Z = \rho c$) as shown in 2.10.

$$\Gamma = \frac{Z_2 \cos o_1 - Z_1 \cos o_2}{Z_2 \cos o_1 + Z_1 \cos o_2}, \quad \tau = \frac{2\, Z_2 \cos o_1}{Z_2 \cos o_1 + Z_1 \cos o_2} \tag{2.10}$$

For a transverse-magnetic (TM) wave in two dimensions, the density perturbation ρ_{small} represents an electric field E_z ($\rho_{small}(x, y) \equiv E_z(x, y)$). Using the analogy in [12] between acoustics and electromagnetics, the flow velocity $\mathbf{u} = (u_x, u_y)$ is equated to the magnetic field $\mathbf{H} = (-H_y, H_x)$. The x and y components of $\mathbf{u}$ and $\mathbf{H}$ are

defined according to the transverse nature of longitudinal electromagnetic wave flow ($\mathbf{u} = \mathbf{E} \times \mathbf{H}$).

$$E_z \rightarrow \begin{cases} \mathbf{u} = u_x \hat{\mathbf{x}} + u_y \hat{\mathbf{y}} \\ \mathbf{H} = H_x \hat{\mathbf{x}} - H_y \hat{\mathbf{y}} \end{cases} \tag{2.11}$$

To analyze fields at the boundary of two media, it is necessary to examine the relationship between the flow velocity $\mathbf{u}$ and density perturbation ρ. As with the pressure fields of Figure 2.5, the electric fields of Figure 2.6 can be expressed in the form of Equation 2.5. The constants A', B' and C' are once again dependent on the properties of the respective media, and the subscripts i, r and t refer to the incident, reflected and transmitted waves.

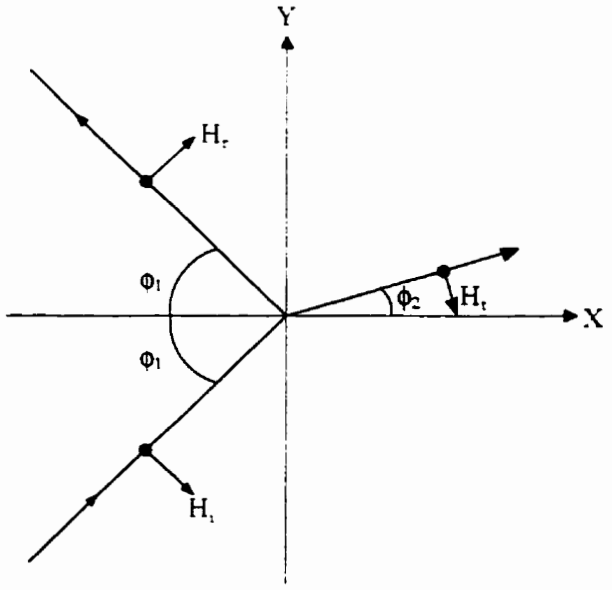

Figure 2.6: Reflection of an electromagnetic wave at a boundary

$$E_{iz} = A' \exp(j k_{1x} x + j k_{1y} y) \tag{2.12}$$

$$E_{rz} = B' \exp(-j k_{1x} x + j k_{1y} y) \tag{2.13}$$

$$E_{tz} = C' \exp(j k_{2x} x + j k_{2y} y) \tag{2.14}$$

The reflection and transmission coefficients Γ and τ are once again defined in terms of the wave impedances ($Z = \sqrt{\frac{\mu}{\epsilon}}$) as shown in 2.15. The form of these equations are the same as those of for the acoustic waves as shown previously in Equation 2.10.

$$\Gamma = \frac{Z_2 \cos o_1 - Z_1 \cos o_2}{Z_2 \cos o_1 + Z_1 \cos o_2}, \quad \tau = \frac{2 Z_2 \cos o_1}{Z_2 \cos o_1 + Z_1 \cos o_2} \tag{2.15}$$

The electric and magnetic fields of a TE or TM electromagnetic plane wave lie in a plane perpendicular to the direction of propagation. The E_z fields of Figure 2.6 have been defined in Equations 2.12 - 2.14, and in order to complete the analogy between acoustic and electromagnetic waves, the magnetic field components H_x, H_y are defined as Equations 2.16 - 2.18.

$$H_{tx} = \frac{E_{tz}}{Z_1} \sin o_1 \quad , \quad H_{ty} = -\frac{E_{tz}}{Z_1} \cos o_1 \tag{2.16}$$

$$H_{rx} = \frac{E_{rz}}{Z_1} \sin o_1 \quad , \quad H_{ry} = \frac{E_{rz}}{Z_1} \cos o_1 \tag{2.17}$$

$$H_{tx} = \frac{E_{tz}}{Z_2} \sin o_2 \quad , \quad H_{ty} = -\frac{E_{tz}}{Z_2} \cos o_2 \tag{2.18}$$

In order to extract numerical information from the lattice, statistical averaging must be performed over an area of space in the lattice[3]. This is essentially the summing of the cellular quantities. Two forms of density are defined: a microscopic or *cell* density, and a macroscopic or *spatial* density. A cell density in the HPP-LGA is simply the density of moving particles in a particular cell:

[3]This is similar to a thermometer measuring a temperature in a small area in space rather than at a single point.

$$\rho_{cell} = \frac{1}{4}\sum_{i=1}^{4} N_i(x_j, y_j) \tag{2.19}$$

N_i, whose value is either 0 or 1, represents the presence or absence of a particle moving in direction i, while x_j and y_j define the position of the cell within a lattice of characteristic spacing $\Delta\ell$. Figure 2.7 shows an arbitrary HPP-LGA lattice. The spatial density at a point (x, y) is found by averaging the cell densities which are located inside a region $\mathbf{R}$. The averaging region can be of any shape, although circles tend to work best as they are not biased towards propagation in any particular direction. If the number of cells in the averaging region $\mathbf{R}$ is N_T, then the spatial density is defined as:

$$\rho(x, y) = \frac{1}{4N_T}\sum_{x,y}^{\mathbf{R}}\left[\sum_{i=1}^{4} N_i(x_R, y_R)\right] \tag{2.20}$$

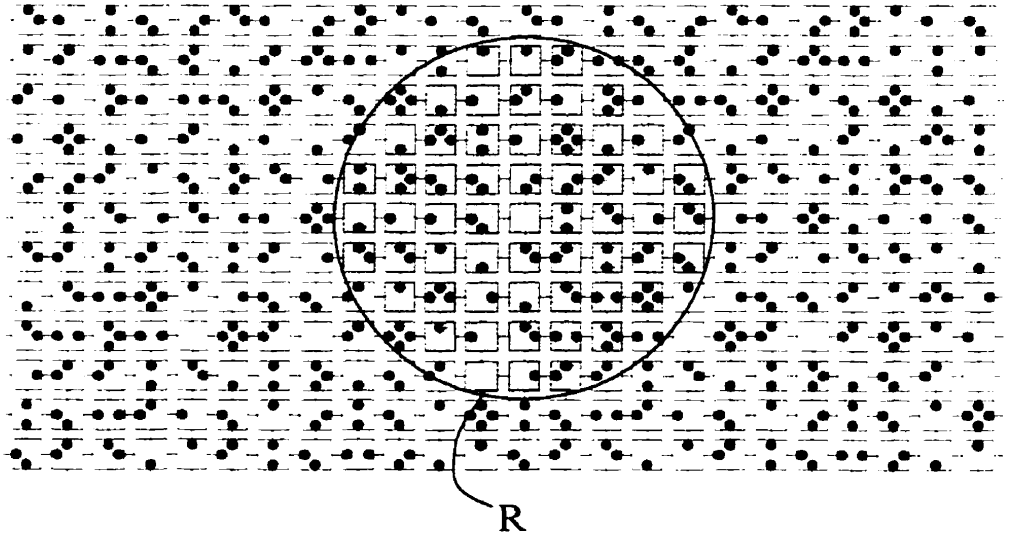

Figure 2.7: Method of calculating field values

The cell to which particle i will propagate to is determined by the velocity state, $\mathbf{c}^i$, of the particle as shown in equation 2.21.

$$\mathbf{c}^i = \cos\left[\frac{\pi}{2}(i-1)\right]\Delta\ell\,\hat{\mathbf{x}} + \sin\left[\frac{\pi}{2}(i-1)\right]\Delta\ell\,\hat{\mathbf{y}} \qquad i = 1,2,3,4 \tag{2.21}$$

The initialization of a lattice of moving particles is a straightforward operation. The lattice has an equilibrium particle density of f, (also known as *background density*), with each moving particle having an equal probability of existing. This condition is essentially satisfied for lattices with $f > 0$ or $f < 1$.

The speed of propagation c_s of a wave through a lattice is independent of the background density in systems where the lattice is large as compared to the mean free path [13], and is given in Equation 2.22.

$$c_s = \frac{1}{\sqrt{2}} \tag{2.22}$$

Measurement of the Speed of Propagation

The method used in this thesis for validating c_s involves observing the propagation of a pulse though a lattice. Once observation points have been chosen, the number of timesteps between consecutive pulse peaks is measured. Dividing the size of the lattice by the amount of time it takes to traverse the lattice yields c_s.

The determination of the exact peak of a measured pulse is complicated by the spatial averaging effect of the sampling window. The viscosity (dissipation) inherent in HPP-LGA also broadens the pulse as it propagates through the lattice, increasing the difficulty in accurately determining the pulse peak. Therefore when examining measured c_s values, these sources of error must be considered.

Although the measurement of less than the total density decreases the resolution of the pulse as it propagates through the lattice, a coarse estimate of c_s can be made by observing any combination of the available particles. An alternate method for

determining c_s involves measuring the resonant frequency of a cavity once a specific mode has been imposed.

2.1.3 Binary Collision Operators

In order to derive the equilibrium particle concentrations for a lattice-gas, it must obey semi-detailed balance [7]. If we represent the transition from state s to state s' by a Boolean transition matrix A, a lattice-gas will obey semi-detailed balance if its transition matrix satisfies:

$$\sum_{s} A(s \rightarrow s') = 1 \tag{2.23}$$

The semi-detailed balance condition ensures that every output configuration is equally likely to occur. The more general condition of detailed balance as expressed in Equation 2.24, ensures that forward and backward transitions occur with equal probability.

$$A(s \rightarrow s') = A(s' \rightarrow s) \tag{2.24}$$

Criteria 2.23 should not be confused with the conservation of probability, expressed in Equation 2.25.

$$\sum_{s'} A(s \rightarrow s') = 1 \tag{2.25}$$

For an n-bit HPP-LGA model, the microscopic collision details can be specified by a 2^n by 2^n Boolean transition matrix. Figure 2.8 shows all 16 possible configurations for a 4-bit HPP-LGA cell. Each input configuration leads to exactly one output

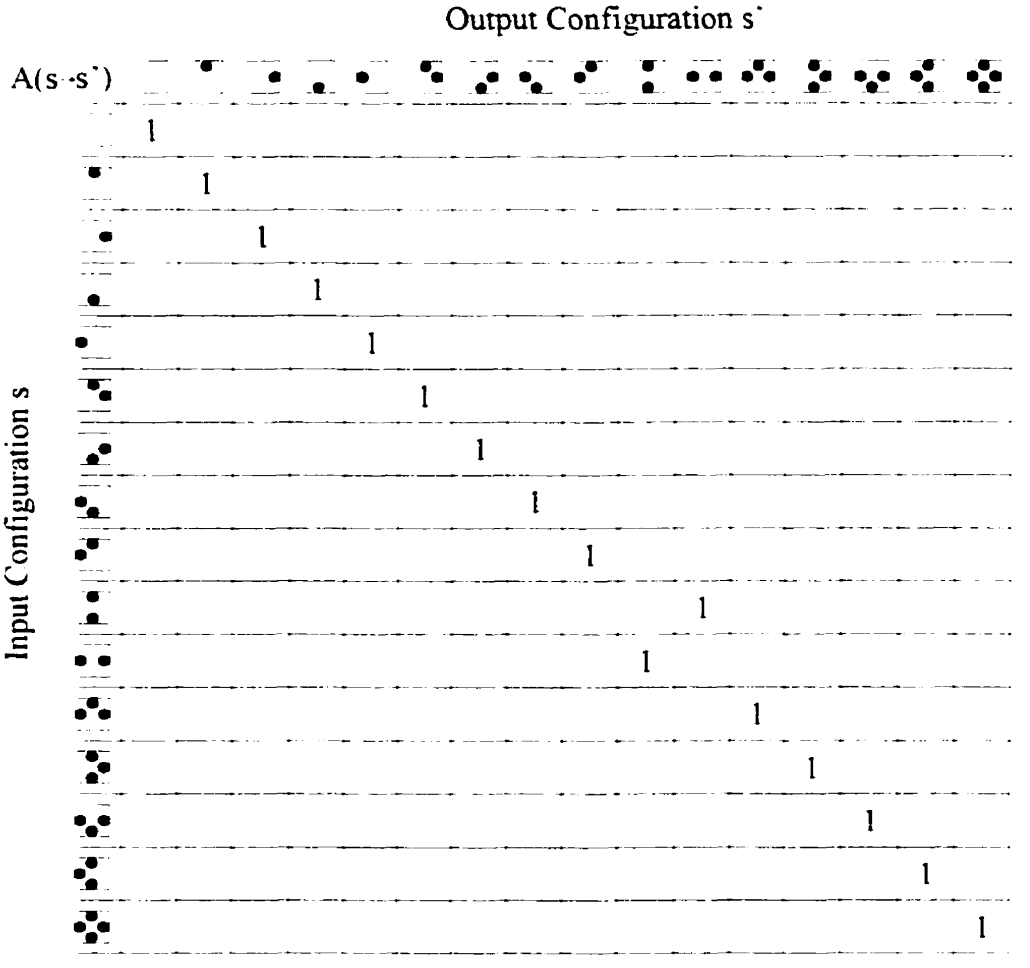

Figure 2.8: Boolean transition matrix for standard HPP-LGA model

configuration, which is denoted by a 1. Except for the HPP-LGA collision, all input configurations lead to themselves as output configurations.

The dynamics of a HPP-LGA can also be completely described by a set of boolean equations known as Binary Collision Operators (BCOs). BCOs can be viewed as a algebraic representation of the Boolean transition matrix. If $b_i(\mathbf{x}, t)$ represents the presence or absence of a particle (denoted by a 1 or a 0), then the presence of a particle in an adjacent cell at the next time step can be expressed as:

$$b_i(\mathbf{x} + \mathbf{c}^i, t + \Delta t) = b_i(\mathbf{x}, t) + C_i[\mathbf{b}(\mathbf{x}, t)] \qquad i = 1, 2, 3, 4 \tag{2.26}$$

where $b_i(\mathbf{x}, t)$ represents the presence or absence of a particle propagating in one of the four directions, represented by velocity state i, in cell $\mathbf{x}$ at time t. $C_i[\mathbf{b}(\mathbf{x}, t)]$ is the microscopic collision operator for direction i, which examines the cell for HPP-LGA collisions. Its input is $\mathbf{b}(\mathbf{x}, t)$, which is a vector of all the particles in cell $\mathbf{x}$ at time t. With this information it is possible to determine $b_i(\mathbf{x} + \mathbf{c}^i, t + \Delta t)$ which is the presence or absence of a particle propagating in direction i, in cell $\mathbf{x} + \mathbf{c}^i$ at the next time-step $(t + \Delta t)$. Equations 2.27 - 2.30 can be used to describe the dynamics of the standard HPP-LGA model as described in Section 2.1.1. These equations may also be found again in Appendix A along with the BCOs for most of the models used in this thesis.

$$\begin{aligned} b_N(x, y + \Delta\ell, t + \Delta t) &= b_N + C_N \\ &= b_N + \overline{b_N b_S} b_E b_W - b_N b_S \overline{b_E b_W} \qquad (2.27) \\ b_S(x, y - \Delta\ell, t + \Delta t) &= b_S + C_S \\ &= b_S + \overline{b_N b_S} b_E b_W - b_N b_S \overline{b_E b_W} \qquad (2.28) \\ b_E(x + \Delta\ell, y, t + \Delta t) &= b_E + C_E \end{aligned}$$

$$= b_E + b_N b_S \overline{b_E b_W} - \overline{b_N b_S} b_E b_W \quad (2.29)$$

$$b_W(x - \Delta\ell, y, t + \Delta t) = b_W + C_W$$

$$= b_W + b_N b_S \overline{b_E b_W} - \overline{b_N b_S} b_E b_W \quad (2.30)$$

In the case of the HPP-LGA in two dimensions, there are three conserved quantities: the number of particles, the x momentum and the y momentum. The x and y momenta are conserved at the cellular level. From equations 2.27–2.30 it can be shown that mass (2.31) and momentum (2.32 and 2.33) are conserved.

$$Mass: \quad C_E + C_N + C_W + C_S = 0 \quad (2.31)$$

$$p_x: \quad C_E - C_W = 0 \quad (2.32)$$

$$p_y: \quad C_N - C_S = 0 \quad (2.33)$$

2.1.4 Modified HPP-LGA

The speed of propagation of a wave must be altered in order to model dielectric materials. This can be done in HPP-LGA through the use of *rest-particles*, which transform the kinetic energy propagating through a lattice into potential energy.

The standard HPP-LGA model of Section 2.1.1 was modified to include the creation of rest-particles in the following manner [14]: When a cell contains exactly 4 moving particles (each of mass m), a rest-particle will be created, replacing the four moving particles. Similarly, this new particle will break back down into four moving particles when the cell is completely empty of moving particles. The rest-particle will have a mass of $4m$ and no velocity component, such that mass and momentum are conserved.

The initial states of 9 HPP-LGA cells are shown in Figure 2.9, with the centre cell in both cases containing all four moving particles. At the next time step, the

four standard HPP-LGA particles have propagated to their respective cells, while the four modified HPP-LGA particles have combined to form a single rest-particle (RP) of mass $4m$.

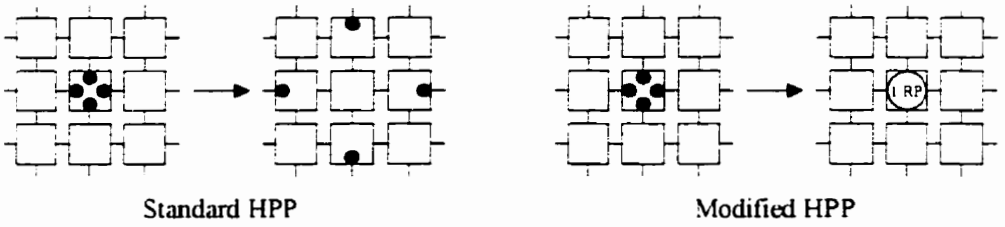

Figure 2.9: Creation of a HPP-LGA rest-particle

This model is not limited to one rest-particle. Figure 2.10 shows the increase from two rest-particles in **A** to three rest-particles in **B**.

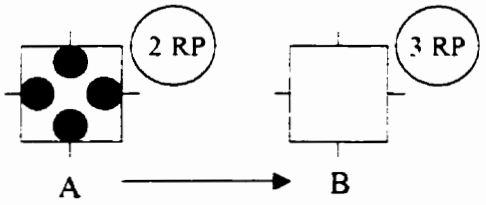

Figure 2.10: HPP-LGA rule with three rest-particles

With the addition of rest-particles, the BCOs as described in the Section 2.1.3 must be modified. Each additional rest-particle adds another level of complexity to these equations. Equations 2.34 to 2.38 represent the BCOs for the HPP-LGA rule with one rest-particle, b_R.

$$\begin{aligned} b_N(x, y + \Delta\ell, t + \Delta t) &= b_N + C_N \\ &= b_N + \overline{b_N} b_S b_E b_W - b_N b_S \overline{b_E} b_W \end{aligned}$$

$$+ \overline{b_N b_S b_E b_W} b_R + b_N b_S b_E b_W \overline{b_R} \tag{2.34}$$

$$\begin{aligned} b_S(x, y - \Delta\ell, t + \Delta t) &= b_S + C_S \\ &= b_S + \overline{b_N b_S} b_E b_W - b_N b_S \overline{b_E b_W} \\ &\quad - \overline{b_N b_S b_E b_W} b_R + b_N b_S b_E b_W \overline{b_R} \end{aligned} \tag{2.35}$$

$$\begin{aligned} b_E(x + \Delta\ell, y, t + \Delta t) &= b_E + C_E \\ &= b_E + b_N b_S \overline{b_E b_W} - \overline{b_N b_S} b_E b_W \\ &\quad + \overline{b_N b_S b_E b_W} b_R + b_N b_S b_E b_W \overline{b_R} \end{aligned} \tag{2.36}$$

$$\begin{aligned} b_W(x - \Delta\ell, y, t + \Delta t) &= b_W + C_W \\ &= b_W + b_N b_S \overline{b_E b_W} - \overline{b_N b_S} b_E b_W \\ &\quad + \overline{b_N b_S b_E b_W} b_R + b_N b_S b_E b_W \overline{b_R} \end{aligned} \tag{2.37}$$

$$\begin{aligned} b_R(x, y, t + \Delta t) &= b_R + C_R \\ &= b_R + b_N b_S b_E b_W \overline{b_R} - \overline{b_N b_S b_E b_W} b_R \end{aligned} \tag{2.38}$$

Since rest-particles do not have any momentum, the x and y momentum conservation equations remain the same. The mass conservation equation does however change. The modifications to the standard HPP-LGA conservation equations are shown in Equations 2.39, 2.40 and 2.41.

$$Mass: \quad C_E + C_N + C_W + C_S + 4C_R = 0 \tag{2.39}$$

$$p_x: \quad C_E - C_W = 0 \tag{2.40}$$

$$p_y: \quad C_N - C_S = 0 \tag{2.41}$$

2.1.5 Viscosity

A wave propagating through the HPP-LGA lattice will be subject to a damping of its magnitude, which is a function of its frequency. This damping is due to anisotropic

viscosity present in HPP-LGA. The quantification of the dissipation in integer lattice-gas automatons (ILGAs) which have been combined with TLM has been conducted in [15], which is an extension of [16] where some multi-bit lattice-gas automatons were examined. It was shown that the effects of viscosity can be significantly reduced by increasing the number of bits involved in particle representation.

In this thesis the effects of viscosity are not studied. Viscosity is mentioned throughout the results section as a possible source of error. This approach was justified by focusing the thesis primarily on the evaluation of HPP-LGA for the simulation of electromagnetic wave phenomena with the use of rest-particles for the modelling of dielectric regions. Errors resulting from unwanted dissipation are to be dealt with at a future time.

2.2 HPP-LGA Rest-Particles

Before examining the dynamics of rest-particles and their relationship to moving particle density, it is important to have an understanding of how rest-particles are represented in the CAM-8 during simulation. A typical HPP-LGA CAM-8 cell has 16 bits[4] allocated to it for the representation of moving particles, rest-particles and markers. A sample template and corresponding bit-cell is shown in Figure 2.11. The cell in Figure 2.11 has three moving particles (north, south and west), one rest-particle and two random bits. Although there are groupings of similar particles (moving, rest, random) this is for convenience only, and not a CAM-8 requirement.

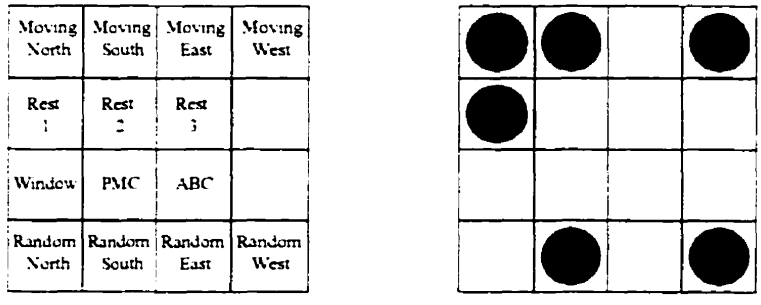

Figure 2.11: Sample cell template

The maximum number of rest-particles, R_{Max}, which a cell can contain is determined by the number of bits associated with it. Using a binary scheme, R_{Max} is determined by Equation 2.42, where n_b is the number of bits allocated to rest-particle storage.

$$R_{Max} = 2^{n_b} - 1 \tag{2.42}$$

[4]For more complex experiments it is possible to increase the effective number of bits at a cell through the swapping of bits in and out of the CAM's DRAM. For more information on this see Appendix B.

Assuming a moving particle mass of m, the first rest-bit represents a mass of $4m$. Each successive bit represents twice as much mass as compared to the rest-bit before. Therefore the mass which the n^{th} rest-bit represents is given by Equation 2.43.

$$m_n = 2^{n+1} m \tag{2.43}$$

A rest-bit of mass m_n can be thought of as either representing a single particle of mass m_n or a number of particles, each with mass $4m$. Although the capability to model regions of R_{Max} particles (using n bits) exists, there is no condition which requires that exactly R_{Max} particles must be used. In other words, although a region of $n_b = 2$ (three rest-particles) can hold up to three rest-particles, there is no reason why it cannot be limited to only two. The next two sections deal with regions where all R_{Max} particles are used (Full R_{Max}) and regions where less than R_{Max} particles are used (Partial R_{Max}).

2.2.1 Full R_{Max} Regions

The initialization of rest-particles is dependent on the background density f_m, and the ratio of the rest and moving particle masses. Assuming a Fermi-Dirac distribution, Equation 2.44 describes the non-linear equilibrium relationship between rest-particle density f_r and moving particle density f_m [7]. The mass ratio z is defined in Equation 2.45.

$$f_r(z) = \frac{{f_m}^z}{{f_m}^z + (1 - f_m)^z} \tag{2.44}$$

$$\frac{m_{rest}}{m_{moving}} = \frac{m_r}{m_m} = z \tag{2.45}$$

The rest and moving particle equilibrium concentrations were verified by initializing a homogeneous $512\Delta\ell \times 512\Delta\ell$ HPP-LGA lattice with various background densities f_m and the corresponding rest-particle densities as predicted by Equation 2.44 for 1, 3 and 7 rest-particles. Individual particle initialization was accomplished by producing a random number and comparing it with the predicted density. Once each system had been initialized, it would be run for $100\Delta T$ and particle levels would be examined: if particle levels remained at the same levels as when the system started, the system would have been properly initialized.

Figures 2.12 and 2.13 show the theoretical and simulated equilibrium densities for a homogeneous $n_b = 2$ region (three rest-particles). The exact fit is representative of the other equilibrium equation simulations which are shown in Appendix K. Since two bits are needed to represent three rest-particles, Figure 2.12 compares the values for the first ($4m$) rest-bit, and Figure 2.13 for the second ($8m$) rest-bit.

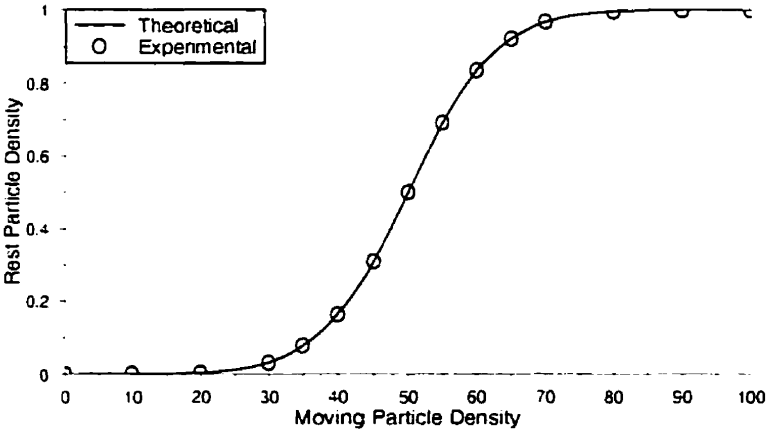

Figure 2.12: Theoretical and simulated equilibrium concentration for a three rest-particle Full R_{Max} model, $4m$ bit

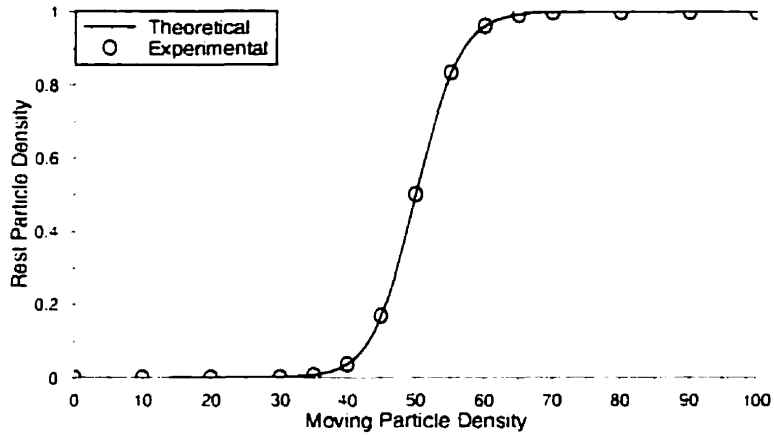

Figure 2.13: Theoretical and simulated equilibrium concentration for a three rest-particle Full R_{Max} model, $8m$ bit

The speed of propagation for a wave through a HPP-LGA lattice with rest-particles is a function of the background density, and is given in Equation 2.46 [17].

$$c_s = \sqrt{\frac{4f_m(1-f_m)}{2\left[4f_m(1-f_m) + \sum_{k=1}^{M} m_k^2 f_k(1-f_k)\right]}} \tag{2.46}$$

where the summation in the denominator is over the rest-particle masses and equilibrium densities.

The dielectric constant of a region of rest-particles is defined as the square of the ratio of the speeds of wave propagation through the region (Equation 2.46) and free-space (Equation 2.22) as shown in Equation 2.47. The resulting equilibrium dependent equation is presented in Equation 2.48

$$\epsilon_r = \left(\frac{c_0}{c_s}\right)^2 \tag{2.47}$$

$$\epsilon_r = \frac{4f_m(1-f_m) + \sum_{k=1}^{M} m_k^2 f_k(1-f_k)}{4f_m(1-f_m)} \tag{2.48}$$

All of the simulations in this thesis were conducted with only R_{Max} regions, and with background densities of 50%. This simplifies Equation 2.48 to Equation 2.49.

$$\epsilon_r = 1 + \sum_{k=1}^{M} 4^k \tag{2.49}$$

An alternative rest-particle model was presented in the Adnani M.Sc. thesis [7]. Instead of using the exponentially increasing definition of rest-particle mass as shown in Equation 2.43, each Adnani rest-particle had an equal mass of $4m$. Figure 2.14 contrasts the resulting ϵ_r from both models with respect to the number of rest-particles. Equation 2.48 is valid for the Adnani model, as long as the appropriate rest-particle mass is used. There is a dramatic increase in the ability to model higher dielectric constants resulting from the exponentially increasing rest-particle model presented in this thesis as opposed to the linear Adnani model.

To illustrate that the Fermi-Dirac equilibrium equation allows for the initialization of multiple rest-particle model regions in equilibrium, half of a $256\Delta\ell \times 256\Delta\ell$ HPP-LGA lattice was initialized with a single rest-particle, while the other half was set to free-space. A 50% moving particle density was used, with the rest-particles initialized to the requisite 50% rest-particle density. A diagram of this system is show in Figure 2.15.

The system was run for $100\Delta T$ and particle levels inside and outside the dielectric region were checked with a $17\Delta\ell \times 17\Delta\ell$ square window to see if initialized levels had been maintained, which would indicate equilibrium. Figure 2.16 shows the total particle density on both sides of the interface in terms of an electric field E_z. The very small variation in the two fields as indicated by the vertical axis indicate that the two regions are in equilibrium with each other.

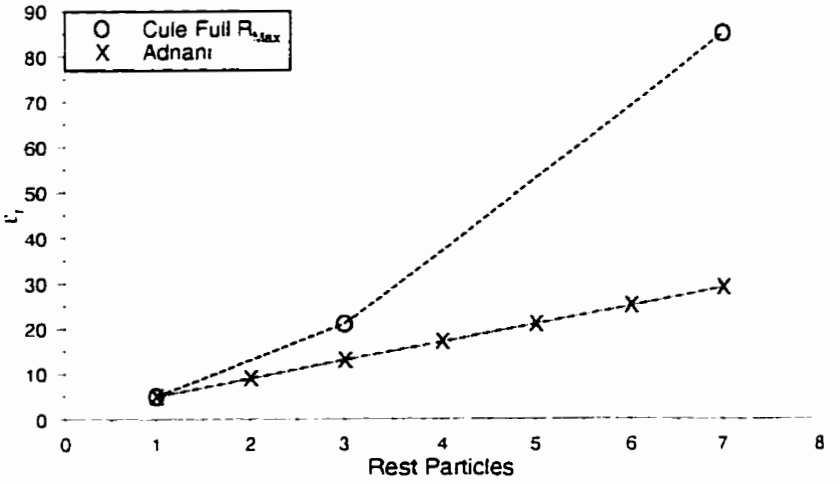

Figure 2.14: Full R_{Max} and Adnani theoretical ϵ_r with respect to rest particles used

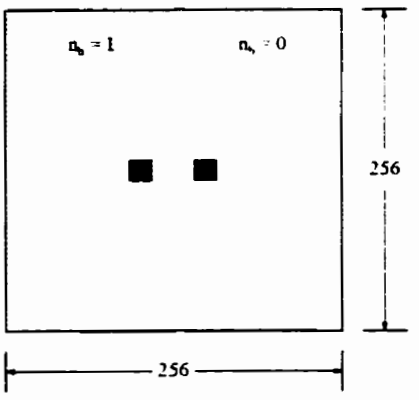

Figure 2.15: Two region equilibrium simulation schematic

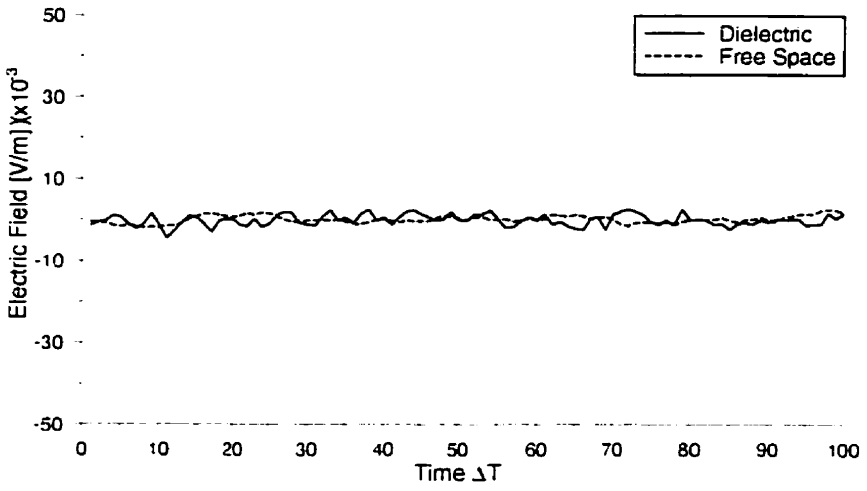

Figure 2.16: Total particle density on either side of a dielectric interface at equilibrium

The existence of rest-particles must be incorporated into the definitions of cell and spatial density. Instead of summing over the number of particles, the density of a cell is defined in terms of the number of *bits* assigned to that cell. For the general case of a cell located at (x_j, y_j) with n_b rest-bits, the cell density is a function of the moving and rest particles, and is defined as:

$$\rho_{cell} = \frac{1}{4 + n_b} \sum_{i=1}^{4+n_b} N_i(x_j, y_j) \tag{2.50}$$

N_i, which represents the presence or absence of a particle in velocity state i is also expanded to include rest-particles.

$$c^i = \cos\left[\tfrac{\pi}{2}(i-1)\right] \Delta\ell \cdot \hat{\mathbf{x}} + \sin\left[\tfrac{\pi}{2}(i-1)\right] \Delta\ell \cdot \hat{\mathbf{y}} \quad i = 1, 2, 3, 4 \tag{2.51}$$

$$c^i = 0 \quad i > 4 \tag{2.52}$$

The spatial density for homogeneous regions of rest-particles, with reference to Figure 2.7, changes to:

$$\rho(x,y) = \frac{1}{N_T(4+n_b)} \sum_{x,y}^{\mathbf{R}} \left[\sum_{i=1}^{4+n_b} N_i(x_R, y_R) \right] \tag{2.53}$$

which is a straightforward modification of Equation 2.50. This definition of density combines the spatial averaging as introduced in Equation 2.20 with the definition of cellular density for a rest-particle cell in Equation 2.50.

2.2.2 Partial R_{Max} Regions

In regions where less than R_{Max} particles are used, the initialization of rest-bits is no longer independent of the other bits. Instead of initializing each rest-bit individually, a single random number is used to determine the states of all the rest-bits.

Let the probability of rest-particle n (RP_n) being created be f_n, and the probability that it will not be created $(1-f_n)$. A table can be constructed which shows all the possible rest-particle combinations, and the probabilities that each will be created. Table 2.1 shows such a table for all the states which three rest-bits can represent.

A Partial R_{Max} correction factor C_r is determined by summing the rest-bit probabilities up to the desired number of rest-particles. The correction factors for Partial R_{Max} regions $n = 2, 4, 5, 6$ is shown in Table 2.2 where $n = 2$ is the correction factor for two rest-bits, and $n = 4, 5, 6$ are for three bits.

The correction factor C_r is used to re-normalize the initialization probabilities due to the initialization interdependence of rest-bits. Equation 2.44 is first used to determine the independent rest-particle densities f_r. Once all necessary densities have been calculated, a re-normalized rest-particle density f'_r is obtained as shown in Equation 2.54.

Table 2.1: Rest-particle probability

RP_1	RP_2	RP_3	Probability	Total Mass
0	0	0	$(1-f_1)(1-f_2)(1-f_3)$	$0m$
1	0	0	$f_1(1-f_2)(1-f_3)$	$4m$
0	1	0	$(1-f_1)f_2(1-f_3)$	$8m$
1	1	0	$f_1f_2(1-f_3)$	$12m$
0	0	1	$(1-f_1)(1-f_2)f_3$	$16m$
1	0	1	$f_1(1-f_2)f_3$	$20m$
0	1	1	$(1-f_1)f_2f_3$	$24m$
1	1	1	$f_1f_2f_3$	$28m$

Table 2.2: Partial R_{Max} correction factors C_r

RP_1	RP_2	RP_3	C_r	Total Mass
0	0	0	None	$0m$
1	0	0	None	$4m$
0	1	0	$1-f_1f_2$	$8m$
1	1	0	None	$12m$
0	0	1	$1+f_3(f_1f_2-f_1f_2)$	$16m$
1	0	1	$1-f_2f_3$	$20m$
0	1	1	$1-f_1f_2f_3$	$24m$
1	1	1	None	$28m$

$$f'_r = \frac{f_r}{C_r} \tag{2.54}$$

The final step involves creating a continuous range for initialization. For two rest-particles this would look like:

$$0 \leq \quad x \quad < f'_0 \qquad\qquad 0\ RPs \tag{2.55}$$

$$f'_0 \leq \quad x \quad < f'_0 + f'_1 \qquad\qquad 1\ RP \tag{2.56}$$

$$f'_0 + f'_1 \leq \quad x \quad \leq f'_0 + f'_1 + f'_2 = 1 \qquad\qquad 2\ RPs \tag{2.57}$$

Partial R_{Max} Dynamics

To show that the correction factor C_r enables Partial R_{Max} regions to be initialized in equilibrium, a $512\Delta\ell \times 512\Delta\ell$ HPP-LGA lattice was initialized with a certain moving particle density and the corresponding rest-particle density. The systems were run for $100\Delta T$ and particle levels were checked to see if initialized levels had been maintained, which would indicate equilibrium. Figures 2.17 and 2.18 show the theoretical and simulated values for both rest-bits in a two rest-particle region.

The theory regarding the speed of propagation for waves through Partial R_{Max} regions has not been developed yet, but values for c_s and ϵ_r have been obtained through simulation.

The pulse method of measuring c_s (as described in Section 2.1.2) was used to determine the ϵ_r values for Partial R_{Max} regions. A $2048\Delta\ell \times 512\Delta\ell$ HPP-LGA lattice was initialized with a moving particle density of 50% and the corresponding rest-particle density for 2, 4, 5 and 6 rest-particles as described earlier. Figure 2.19 shows the values obtained as well as the Full R_{Max} values (1, 3 and 7 rest-particles) from Section 2.2.1. The Adnani values are provided once again for reference [7].

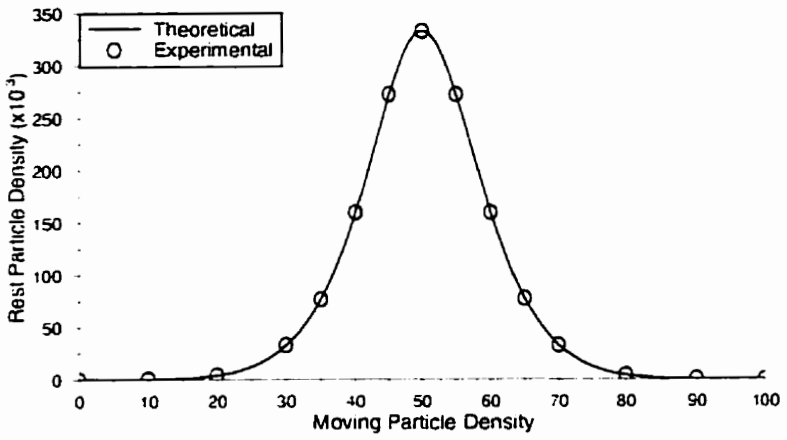

Figure 2.17: Theoretical and simulated equilibrium concentration for a two rest-particle Partial R_{Max} model. $4m$ bit

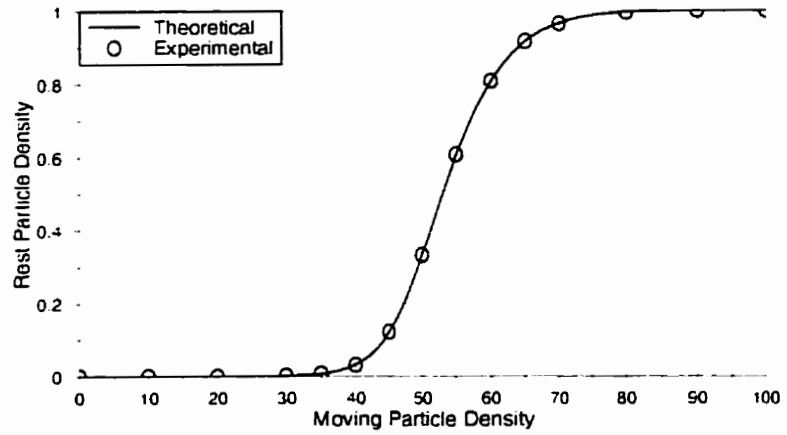

Figure 2.18: Theoretical and simulated equilibrium concentration for a two rest-particle Partial R_{Max} model. $8m$ bit

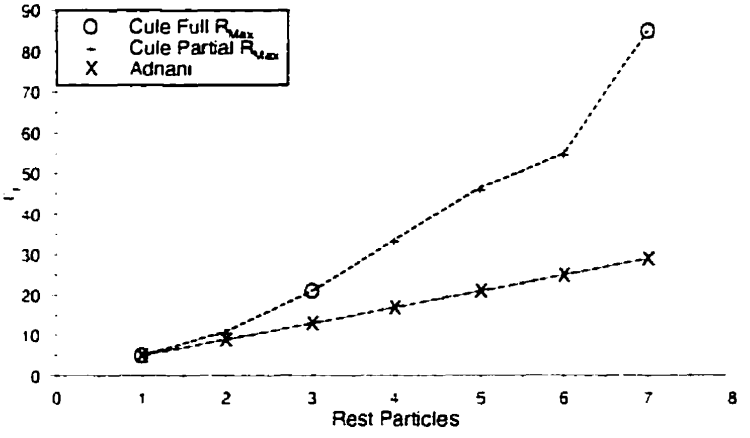

Figure 2.19: Theoretical Full R_{Max}, simulated Partial R_{Max} and theoretical Adnani ϵ_r with respect to rest-particles used

2.2.3 Spatial Combinations of Rest-Particle Models

The use of rest-particle models as presented in the previous two section allow for the modelling of specific values of ϵ_r. In order to model an arbitrary ϵ_r value, the three Full R_{Max} models (Section 2.2.1) are combined spatially to create a region with the desired dynamics. Figure 2.20 shows an arbitrary lattice which has a mixture of 50% single rest-particle cells and 50% three rest-particle cells. As commented earlier, if each individual cell is initialized with the correct equilibrium density as predicted by Equation 2.44, the lattice will remain in equilibrium.

Regions with desired ϵ_r values are created by probabilistically assigning cells a rest-particle mass based on a fill factor p_k. Let the probability that a cell will be assigned a rest-particle mass m_k be p_k. The speed of a wave through that region is then given by Equation 2.58 [17]. The corresponding value of ϵ_r is given in Equation 2.59.

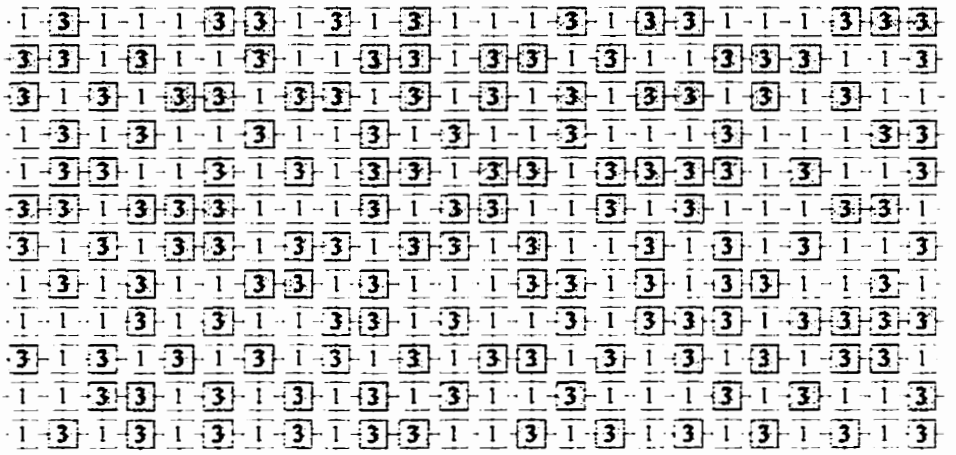

Figure 2.20: Spatial mixing of rest-particle models

$$c_s = \left[\frac{4f_m(1-f_m)}{2\left[4f_m(1-f_m) + \sum_{k=1}^{M} m_k^2\, p_k\, f_k(1-f_k)\right]} \right]^{\frac{1}{2}} \tag{2.58}$$

$$\epsilon_r = \frac{4f_m(1-f_m) + \sum_{k=1}^{M} m_k^2\, p_k\, f_k(1-f_k)}{4f_m(1-f_m)} \tag{2.59}$$

The pulse method of measuring c_s (as described in Section 2.1.2) was used to verify the ϵ_r values as predicted by Equation 2.59. A $2048\Delta\ell \times 512\Delta\ell$ HPP-LGA lattice was initialized with a moving particle density of 50% while the fill factor p_k was increased from 0% to 100% for combinations of rest-particle models. Figure 2.21 shows the agreement between predicted and simulated values for the mixture model. The fill factor p_k corresponds to the amount of the heavier model mixed with $1 - p_k$ of the lighter as indicated in the legend. The lines indicate the predicted ϵ_r values as defined in Equation 2.59, while the Xs on the lines correspond to values obtained from simulation. The slight discrepancy between the predicted and simulated values can be attributed to the difficulty in determining the exact position of the peak of a propagating pulse.

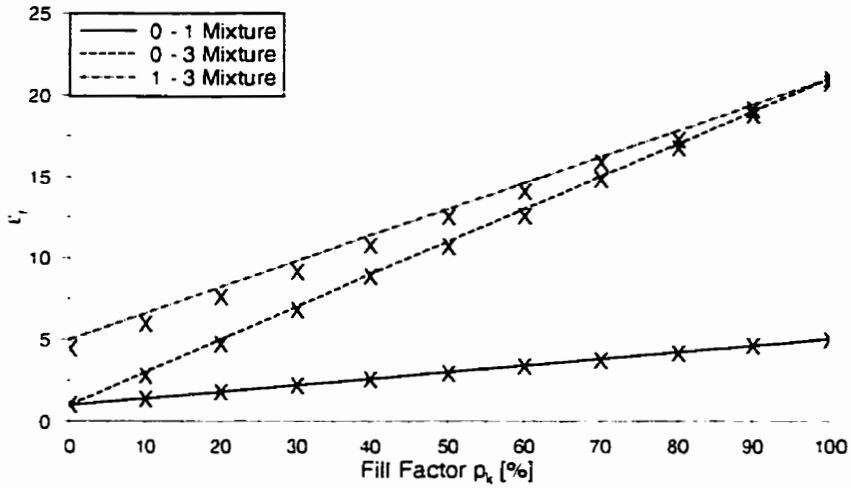

Figure 2.21: Comparison between predicted and simulated ϵ_r values for various fill factor mixtures

The method of calculating the spatial density changes once again due to the inhomogeneous nature of the regions with respect to the cellular models. With reference to Figure 2.7, the method of calculating $\rho(x, y)$ becomes:

$$\rho(x, y) = \frac{1}{N_T} \sum_{x,y}^{R} \left[\frac{1}{M} \sum_{i=1}^{M} N_i(x_R, y_R) \right] \tag{2.60}$$

The combination of two different rest-particle models is represented by the notation $x\%$ (A,B) such that a mixture of x% A rest-particles exists in a background of B rest-particles. The mixture method is not confined to the combination of only two models. Multiple rest-particle models can be mixed together, providing a large number of options for the modelling of dielectric regions. The number of possible mixtures increases if the Partial R_{Max} models are included. In this thesis, only combinations of two different rest-particle rules are used.

Selection Of Fill Factors

For large regions, the relative composition of the dielectric region is of low importance: different mixtures will all perform equally with regards to the desired dynamics. As the size of the region decreases, the ratio of the respective rest-particles becomes of greater importance.

No study was conducted on the relative performance of different mixtures for the modelling of the same value of ϵ_r in small regions. In this thesis, all fill factors were chosen according their Full R_{Max} ϵ_r neighbor values. Once the need for a mixture was identified, the ϵ_r values which bounded it as defined in Equation 2.49 were combined in the appropriate ratio.

The merits of modelling a particular region with a two, three or four rest-particle mixture is left for the next stage of analysis. A possible method is to attempt to

fill the regions with p_k values which are as close as possible to 50%. while another possibility is to minimize the range of dielectric values involved in the mixing.

2.3 Boundary Conditions and Source Excitation

2.3.1 Boundary Conditions

The default CAM-8 periodic boundary condition connects the cells located along the perimeter of a lattice to the cells directly opposite them. For a lattice with horizontal and vertical periodic boundary conditions, a rectangular lattice such as Figure 2.7 can be visualized as torus, as shown in Figure 2.22.

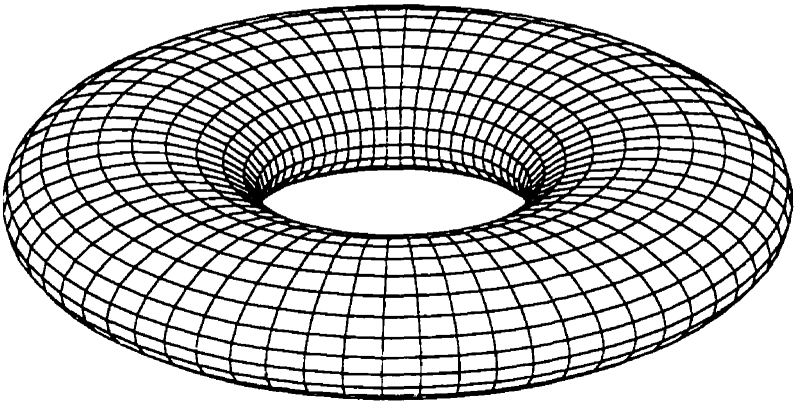

Figure 2.22: HPP-LGA lattice with vertical and horizontal periodic boundary conditions

A perfect magnetic conducting boundary (PMC) has been used to bound the HPP-LGA lattice as an alternative to periodic boundaries. Particles incident on a PMC are reflected back into the lattice as shown in Figure 2.23. This is similar to the HPP-LGA collision as explained in Section 2.1.1 in that particles enter a cell which has been designated as a PMC, and at the next time step are returned to the

originating cell moving in the opposite direction.

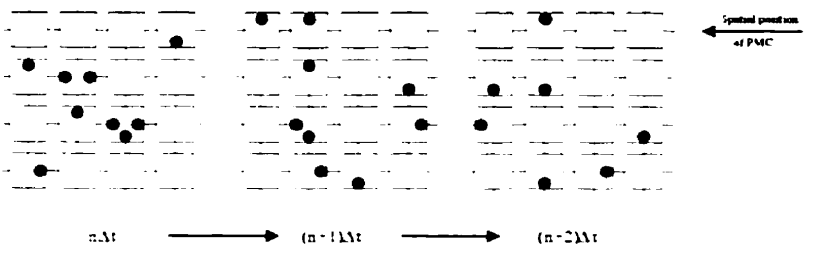

Figure 2.23: Perfect magnetic conductor boundary condition

An absorbing boundary condition (ABC) has also been developed. The details regarding the implementation and performance of the ABC are presented in the next chapter.

2.3.2 Source Excitation

Two types of sources were used in this thesis. The majority of the simulations used a Gaussian pulse as the source term to simulate transients for wideband analysis. Steady-state simulations were accomplished by illuminating an object with a continuous waveform.

Gaussian Pulses

A Gaussian pulse was created by superimposing a Gaussian distribution of particles on top of the existing background distribution. For pulses propagating along the x axis, the distribution of particles takes the form of Equation 2.61, where the centre of the pulse with magnitude M and standard deviation σ is located at x_c.

$$\rho_p = M \exp[\frac{x-x_c}{\sigma}]^2 \tag{2.61}$$

Each cell in the lattice is examined and initialized according to the probability ρ_p, taking care that the initialized cell locations are symmetric about the pulse centre[5]. The resulting pulse will split into two equal pulses traveling in opposite directions. There already exists a background density of particles, and therefore each individual pulse will have a magnitude which is a combination of the background density and the initial Gaussian distribution.

A single pulse can be created by using a PMC in conjunction with Equation 2.61. Instead of superimposing a complete Gaussian pulse on top of the background density, only those cells to one side of the centre of the pulse have particles associated with the Gaussian pulse added. A PMC is then placed along the centre of the pulse. As time evolves, the pulse will launch in one direction only. This method of illuminating an object was used in order to remove the effect of the unwanted secondary pulse created from a full Gaussian implementation. When comparing predicted responses obtained from other computational methods with a single-pulse HPP-LGA source, it is important to include the aforementioned PMC in the simulation space.

Continuous Time-Domain Sources

A continuous waveform is launched by defining a waveform in a separate bit-space, and then injecting the pattern into the simulation space at a predetermined spot. At each timestep, the bit-space containing the discretized waveform increments a single cell, and the next set of particles is inserted.

Figure 2.24 illustrates the manner in which a west propagating waveform is formulated. The top portion shows a HPP-LGA lattice with a column of cells identified as the spatial source for the continuous waveform. The centre section shows the desired waveform which is to be injected into the lattice above it. The bottom portion

[5]This is in specific reference to pulses which may be centered close to the edge of the lattice.

illustrates the bit-space discretization of the waveform above it.

As the lattice evolves in time, the spatial location in the HPP-LGA lattice remains fixed, while the discretized lattice is shifted one cell per timestep in the direction of propagation. In an attempt to reduce the chance of introducing correlated patterns in the input waveform, the waveform bit-space is randomly shifted in the transverse direction. The magnitude of the discretized waveform as shown in Figure 2.24 is 50%, which operates on a background of 50%. This magnitude is far too large for use in an actual simulation, but is used to illustrate the concept.

In order to maintain a continuous wave, the bit-space wavelength, λ_{BS}, must be an integer fraction of the lattice in the direction of propagation. The wavelength of the wave which propagates through the lattice is larger than λ_{BS} by a factor of $\sqrt{2}$ [6]. Only single frequency waveforms were used in this thesis. A waveform consisting of any combination of frequencies can be used as long as the resulting waveform is continuous and periodic with the lattice size.

[6] The speed of propagation.

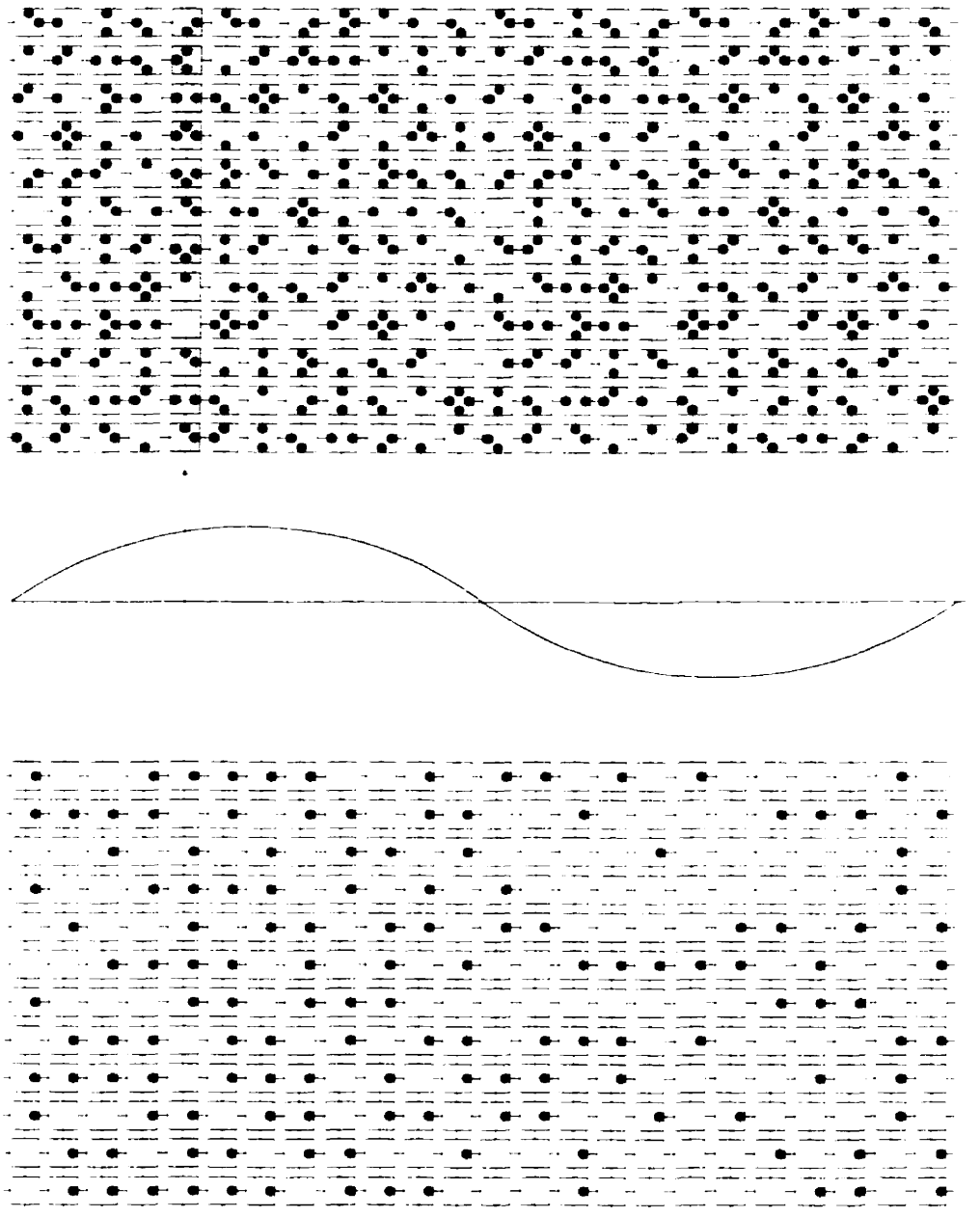

Figure 2.24: Continuous waveform formulation schematic

Chapter 3

Elementary HPP-LGA Experiments

The application of HPP-LGA to the prediction of two-dimensional electromagnetic wave phenomena is presented in this chapter. The scattering of electric fields by homogeneous and inhomogeneous dielectric regions is examined for validation of the theory presented in Chapter 2. Comparisons with analytical values provides an absolute measure of the accuracy of the HPP-LGA method, while similarities with TLM predictions provides a relative measure of performance.

3.1 Absorbing Boundary Condition

The default periodic CAM-8 boundary condition as described in Section 2.3 is not suitable for the simulation of problems where the finite HPP-LGA lattice represents an infinite space. Given the CAM-8's finite resources, it is necessary to bound the lattice with an absorbing boundary condition (ABC), which will provide the appearance of an infinite space and make it possible to simulate this class of problems without causing errors to the predicted response via reflections from the truncated space.

The use of ABCs in the modelling of electromagnetic wave propagation is well documented. A general review of the concept and various implementations can be found in [18]. A body of literature does not exist on the topic of HPP-LGA ABCs, although the fundamental concept has been identified by Wolfram in [13]:

> Random boundary fluxes imitate an infinite region: a regular pattern of incoming particles nevertheless also suffices ...

and extended in [9]:

> An absorbing boundary condition has also been implemented. The algorithm injects particles back into the lattice at an appropriate rate to maintain the initial background density. Although the accuracy of this absorbing boundary condition is quite poor, it demonstrates the applicability of the concept to the lattice gas automata.

While the accuracy of an ABC is commented on in [9], no numerical results are provided. In this section the implementation details of an HPP-LGA ABC are discussed and the performance is quantified. The concept of a graded ABC is introduced and the improvement over the basic HPP-LGA ABC is computed.

A rudimentary ABC was created by defining a vertical wall of cells within the lattice, a single cell in width. These cells injected random particles back into the lattice as described by [13]. A graded ABC was produced by creating a transition from free-space to the solid column of ABC cells. The overall width of the ABC was increased, with the density of ABC cells for each column a function of its relative position in the ABC. An example of a graded ABC is shown in Figure 3.1, where the width of the ABC is 4 cells.

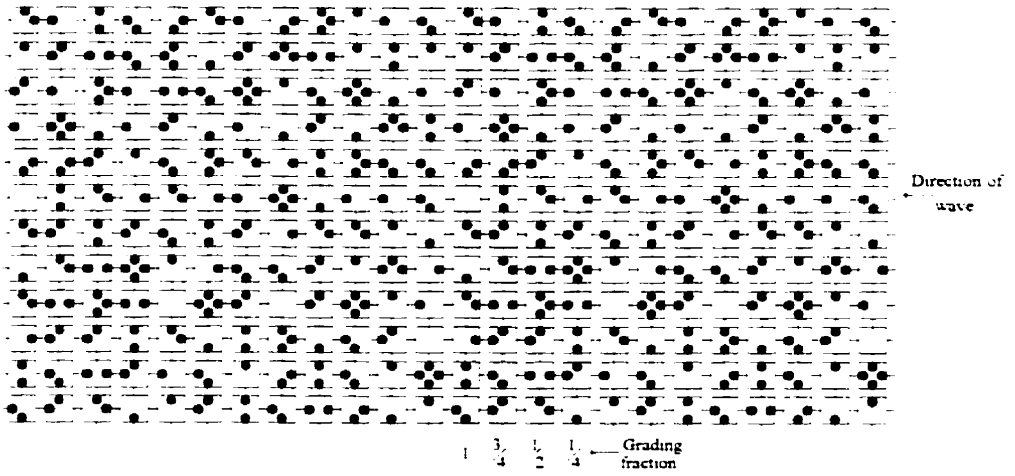

Figure 3.1: Schematic of a graded absorbing boundary condition in an HPP-LGA lattice

A normally incident Gaussian pulse was used to test the performance of the ABC. The size of the lattice used for implementing and evaluating the HPP-LGA ABC was $2048\Delta\ell \times 512\Delta\ell$, with vertical and horizontal periodic boundary conditions, and a background density of 50%. The Gaussian pulse had a magnitude of 20%, $\sigma = 100\Delta\ell$, and its centre was located at $x = 1024\Delta\ell$. A circular sampling window was located at $x = 800\Delta\ell$ with a radius of 25 cells. The ABC began at $x = 512\Delta\ell$, and as it broadened it grew towards the sampling window, with the column of cells located at $x = 512\Delta\ell$ always terminating the graded ABC. The calculated fields from 50

simulations were averaged to create the analyzed waveform for each individual case.

The accurate simulation of a wave in the presence of an ABC requires the maintenance of the initial background density. This was satisfied by employing a separate lattice of random particles for injection with the same density as the background. Figure 3.1 shows the averaged time-domain sampled electric field for the normal incidence of a Gaussian pulse on a single column of ABC cells, and a graded ABC with a width of 10 cells.

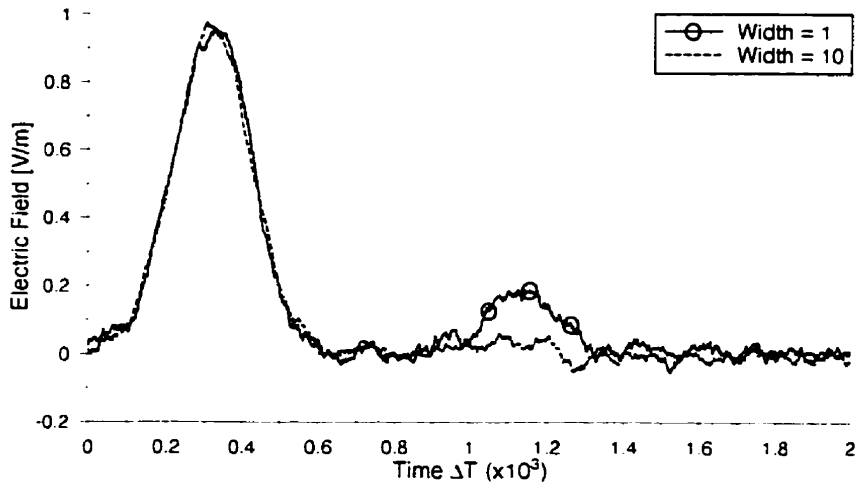

Figure 3.2: HPP-LGA ABC averaged time-domain waveforms. ABC width = $1\Delta\ell$ and $10\Delta\ell$

For a pulse incident on the ABC, the reflection coefficient Γ was defined as the ratio of the magnitudes of the reflected pulse to the incident pulse. A lower value of Γ represents a better performing ABC. In the search for an optimal graded ABC thickness, the width of the ABC was varied from a single cell to 29 cells. The resulting values of Γ for this set of widths is shown in Figure 3.3.

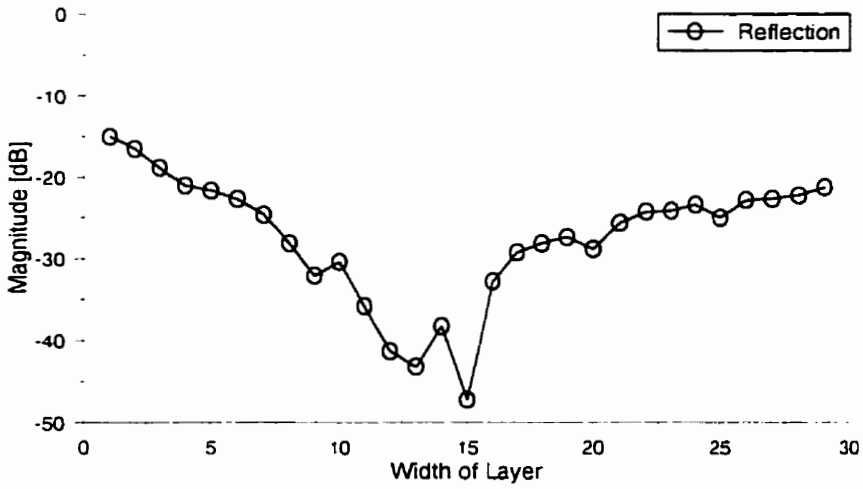

Figure 3.3: HPP-LGA graded ABC reflection coefficients as a function of ABC width

The HPP-LGA single column ABC is effective in absorbing normally incident waves, and its performance improves with the introduction of the free-space grading. For a single column ABC, Γ was determined to be -15dB. As the ABC broadened, Γ decreased steadily to a value of -40dB for a width of 15 cells. For widths greater than 15 cells, Γ increased from -40dB to -22dB. A graded ABC width greater than 29 cells was not simulated because there was no indication that Γ would improve. The Γ values corresponding to graded ABC widths of 10, 14, 20 and 25 cells deviate from the general trends around them. These inconsistencies cannot be explained.

The performance of the HPP-LGA ABC for obliquely incident waves was investigated, but results were difficult to interpret. It would appear that any ABC formulation performs poorly for waves with non-normal incidence. The characterization of the ABC in this section involved lattice truncation in regions without rest-particles, and thus the performance of an ABC which terminates a rest-particle region has not

been developed yet.

The ABC as described above was used in the simulations described in this and the next chapter. The performance of the HPP-LGA ABC is not as accurate as the HPP-LGA implementation of a PMC, as described in Section 2.3. Further in this chapter, TLM predictions of system responses are provided. For systems where no analytical solution has been provided, a more precise comparison between TLM and HPP-LGA could have been accomplished by replacing the HPP-LGA ABCs with more accurate HPP-LGA PMCs, and making the necessary changes to the TLM simulations.

3.2 Normal Incidence at a Plane Dielectric Boundary

In this section the reflected and transmitted electric fields for an HPP-LGA Gaussian pulsed plane wave incident on a plane dielectric boundary is investigated in order to verify the performance of the modified HPP-LGA rest-particle models as presented in Section 2.1.4. The analytical reflection and transmission coefficients are determined and used for comparison with the predicted values obtained from simulations. Homogeneous dielectric regions are modelled using the Full R_{Max} rest-particle rules as described in Section 2.2.1.

A normally incident Gaussian pulse was used to test the performance of the rest-particle models. A $4096\Delta\ell \times 256\Delta\ell$ lattice with a background density of 50% and periodic boundary conditions was used for all simulations. The Gaussian pulse was centered at $x = 2047\Delta\ell$ with a magnitude of 15%, and $\sigma = 100\Delta\ell$. The dielectric region was located from $x = 0\Delta\ell$ to $x = 1023\Delta\ell$ with a dielectric constant $\epsilon_r = 5.21$ or 85. Two sampling windows of radius $50\Delta\ell$ were used: one located inside the dielectric region at $x = 511\Delta\ell$ and the other outside at $x = 1355\Delta\ell$. The calculated fields from 20 simulations were averaged to create the representative waveform for each individual case.

Figure 3.4 shows the averaged time-domain predicted electric field at the two window locations for an $\epsilon_r = 5.0$ region. The three pulses represent the incident, reflected and transmitted fields, respectively.

When a wave is incident on a dielectric medium that has a different dielectric constant than the one through which it is currently propagating, a portion of the wave will be reflected. The reflection coefficient Γ is a ratio of the reflected wave to the incident wave, and is analytically determined by Equation 3.1. The region

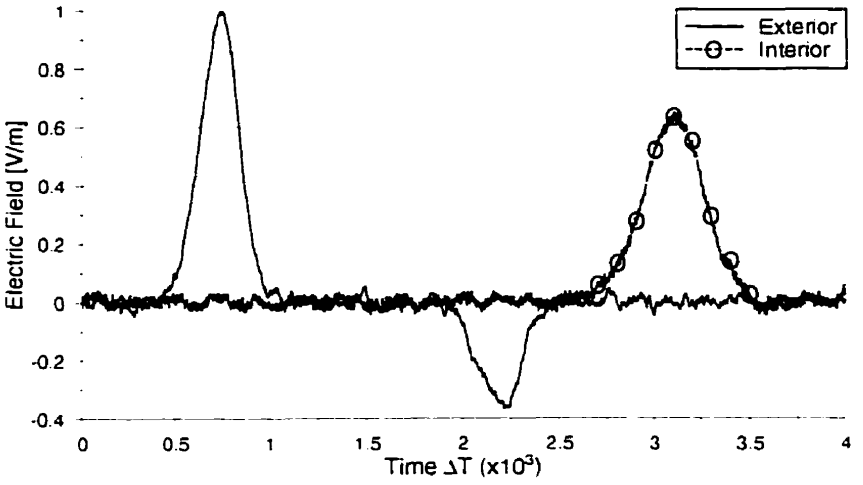

Figure 3.4: Averaged time-domain plot of predicted incident, reflected and transmitted pulses in an $\epsilon_r = 5$ plane dielectric boundary

Table 3.1: Comparison of predicted and analytical results for Gaussian pulsed plane waves normally incident on a plane dielectric boundary

ϵ_r	Parameter	Predicted	Analytical	% Error
5	Γ	-0.3697	-0.3820	3.22 %
	τ	0.6479	0.6180	4.83 %
21	Γ	-0.6066	-0.6418	5.48 %
	τ	0.3265	0.3582	8.85 %
85	Γ	-0.7799	-0.8043	3.03 %
	τ	0.1816	0.1957	7.20 %

from which the wave is propagating from is represented by ϵ_1, while the region which the wave is incident on is represented by ϵ_2. Having determined Γ, the transmission coefficient τ is calculated from the relation: $\tau = 1 + \Gamma$.

$$\Gamma = \frac{\frac{1}{\sqrt{\epsilon_2}} - \frac{1}{\sqrt{\epsilon_1}}}{\frac{1}{\sqrt{\epsilon_2}} + \frac{1}{\sqrt{\epsilon_1}}} \tag{3.1}$$

The coefficients Γ and τ were calculated by taking the ratio of the magnitudes of the reflected and transmitted pulses to the incident pulse. Table 3.2 summarizes the values for Γ and τ for the three dielectric constants used. Given the analytical values from Equation 3.1, and the predicted values, the percentage error was calculated by dividing the absolute value of the difference between the predicted and analytical values by the analytical value.

Table 3.2 shows that the percentage error in both Γ and τ remains under 10% for all three dielectric regions. The errors do not appear to be dependent on the region being modelled. Γ is consistently more accurate than τ, which can be attributed to

the HPP-LGA dielectric region modelling characteristics.

The HPP-LGA windows inside and outside the dielectric region are the same size with respect to the lattice dimensions. However, the interior window is larger in terms of electrical dimensions due to the reduced propagation velocity inside the dielectric region. This results in a greater physical area over which the window samples, reducing the maximum predicted value. In addition to window size, the effect of viscosity on the propagation of the pulse is different in the dielectric region than in free space. The effect of viscosity will be a general reduction in the magnitude of the propagating wave.

3.3 Normal Incidence at a Thin Dielectric Boundary

In this section, the accuracy of reflected and transmitted waves for an HPP-LGA Gaussian pulsed plane wave normally incident on a thin dielectric region of varying width is investigated. TLM predictions of corresponding systems are provided for comparison, and both methods are compared to analytical values. In accordance with the findings in [19], the ratio of HPP-LGA cells to TLM cells is set at 10:1.

3.3.1 Geometry Description

A $4096\Delta\ell \times 256\Delta\ell$ HPP-LGA lattice with vertical and horizontal periodic boundary conditions was used for the simulation of the system. A single Gaussian pulsed plane wave[1] propagating left to right with a magnitude of 10% and $\sigma = 50\Delta\ell$ was incident on the dielectric region. Thin planes with a width of 1 mm, 2 mm and 3 mm were modelled with HPP-LGA cells which had a resolution of 0.1 mm. Each region had a dielectric constant $\epsilon_r = 5.0$. The centre of each sampling window was located $35\Delta\ell$ from the nearest dielectric interface, with a radius of $25\Delta\ell$. The calculated fields from 20 simulations were averaged to create the resulting waveform for each individual case.

The relationship between the incident, reflected and transmitted waves was determined by solving a system of equations comprised of the electric and magnetic field intensity vectors in all three regions, with the application of the appropriate boundary conditions. For a z-directed electric field (as in Figure 2.6) the system looks like Figure 3.5. Regions 1 and 3 are the same. The three regions were assumed to be dissipationless in the derivations of the transmission and reflection coefficients Γ and

[1] As described in Section 2.3.

τ. In the following equations, η_1 and η_2 represent the intrinsic impedance of regions 1 and 2.

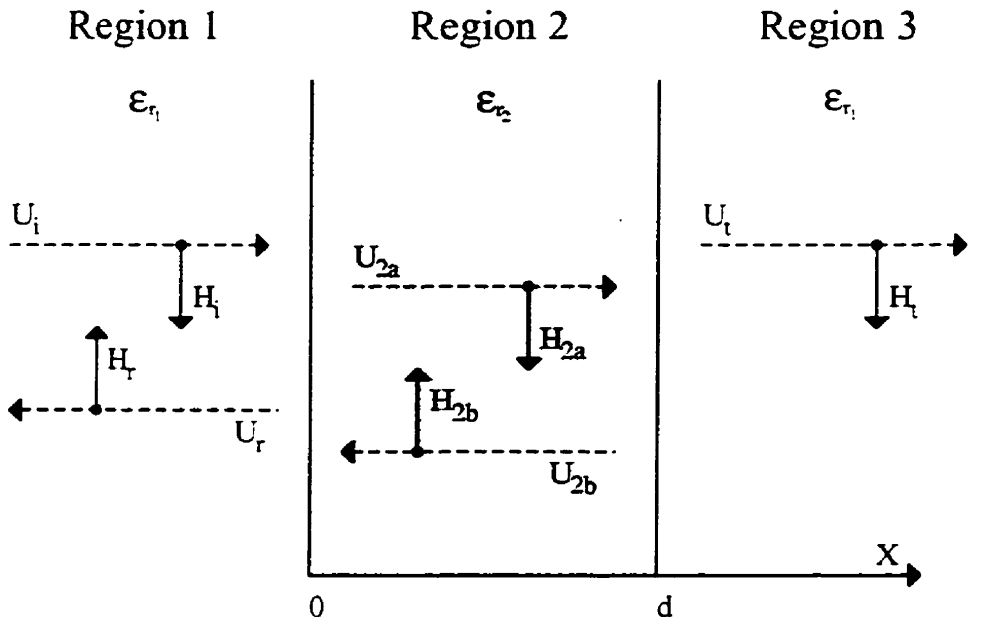

Figure 3.5: Normal incidence on a thin dielectric boundary schematic

$$\eta_1 = \sqrt{\frac{1}{\epsilon_{r_1}}}, \quad \eta_2 = \sqrt{\frac{1}{\epsilon_{r_2}}} \tag{3.2}$$

In Equation 3.3, β_1 and β_2 represent the phase constants of regions 1 and 2, where f is the frequency of interest and c is the speed of light.

$$\beta_1 = \frac{2\pi f\sqrt{\epsilon_{r_1}}}{c}, \quad \beta_2 = \frac{2\pi f\sqrt{\epsilon_{r_2}}}{c} \tag{3.3}$$

The reflection coefficient Γ is the ratio of the reflected wave E_r to the incident wave E_i, and is given in Equation 3.5. The transmission coefficient τ is no longer related to Γ by the expression in Section 3.2 due to the multiple reflections occurring between the bounding surfaces of the thin dielectric region. The expression for τ is

given in Equation 3.6. For both equations, d is the physical size of the dielectric boundary.

$$C = \left[\frac{\eta_1 + \eta_2}{\eta_1 - \eta_2}\right] e^{(2j\beta_2 d)} \tag{3.4}$$

$$\Gamma = \left[\frac{\eta_2(C+1) - \eta_1(C-1)}{\eta_2(C+1) + \eta_1(C-1)}\right] \tag{3.5}$$

$$\tau = \left\{C\left[\frac{\Gamma+1}{C+1}\right] e^{(-j\beta_2 d)} + \left[\frac{\Gamma+1}{C+1}\right] e^{(j\beta_2 d)}\right\} e^{(j\beta_1 d)} \tag{3.6}$$

The frequency content of the HPP-LGA and TLM incident pulses is shown in Figure 3.6. Although both pulses are Gaussian in nature, their calculated frequency content varies slightly due to differences in discretization schemes and due to the spatial averaging caused by the HPP-LGA sampling window. Using the expressions for the reflection coefficient Γ and transmission coefficient τ, the numerical values corresponding to the theoretical transmitted and reflected responses were based on the actual TLM or HPP-LGA initial Gaussian pulse for each individual simulation. This was necessary because the incident HPP-LGA pulses additionally varied slightly from one simulation to the next.

3.3.2 Results

A time-domain plot of the the sampled waveforms to the left and right of the dielectric region is shown in Figure 3.7. This plot corresponds to a single simulation of a 2 mm wide region (20 Δ_{LGA}, 2 Δ_{TLM}) with $\epsilon_r = 5.0$. The percentage error for the HPP-LGA and TLM simulations are shown in Figures 3.8 - 3.11. Given the analytical values from Equations 3.5 and 3.6, and the predicted values from the simulations,

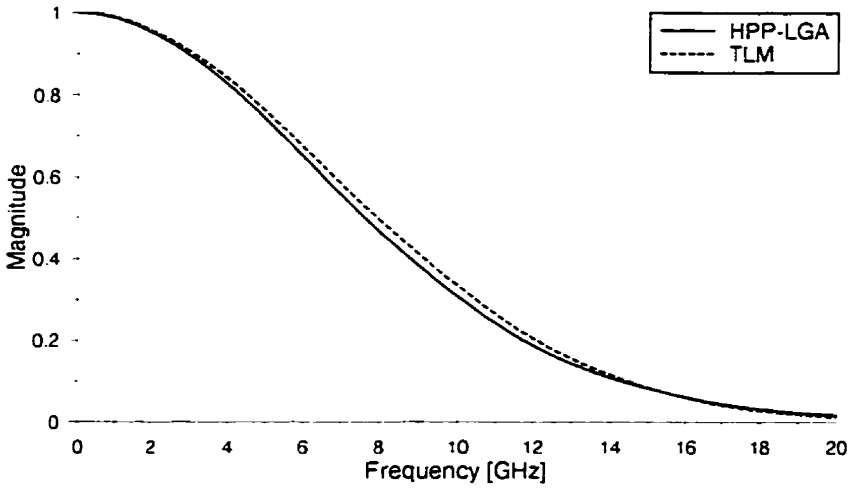

Figure 3.6: Frequency content of incident HPP-LGA and TLM Gaussian pulses

the percentage error was calculated by dividing the absolute difference between the predicted and analytical values by the analytical value. The reflection coefficient error for both methods was set to 0 at a frequency of 0 GHz.

The HPP-LGA reflected and transmitted errors are an order of magnitude larger than the TLM errors for the entire frequency range. The HPP-LGA reflected error is much larger than the HPP-LGA transmitted error, which is opposite to what was found in the study of Gaussian pulses normally incident on plane dielectric boundaries (Section 3.2). The large initial reflected error is due to the small values for the analytical reflection coefficient at low frequencies.

Other than the 1 mm simulation, errors remain under 10% for most of the frequency range with the exception of the 0 - 3 GHz range for the 3 mm reflected error. Errors may have been introduced in the waveform extraction process. Premature truncation of an HPP-LGA waveform will result in loss of frequency information, and

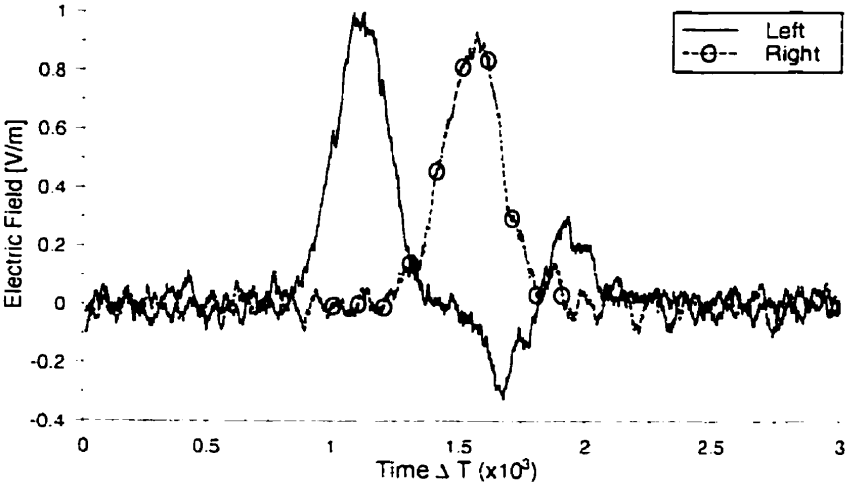

Figure 3.7: Un-averaged HPP-LGA time-domain waveforms to the left and right of a 2 mm $\epsilon_r = 5$ dielectric region

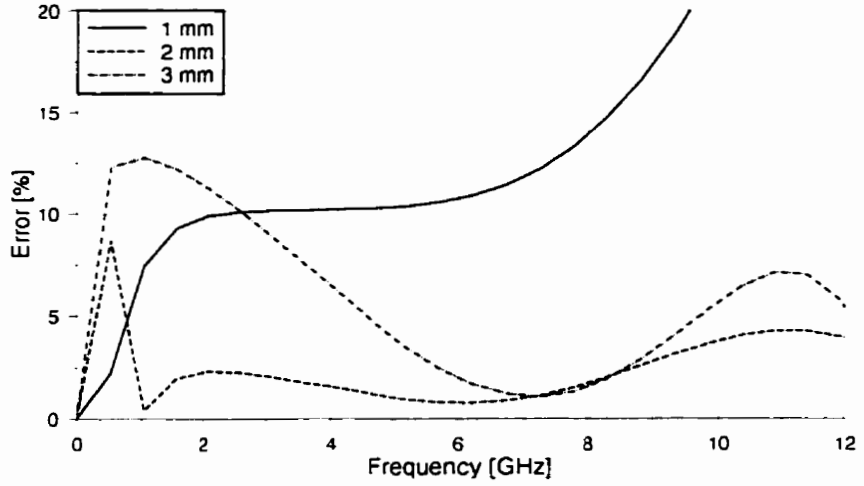

Figure 3.8: HPP-LGA reflected error for a thin $\epsilon_r = 5$ dielectric region

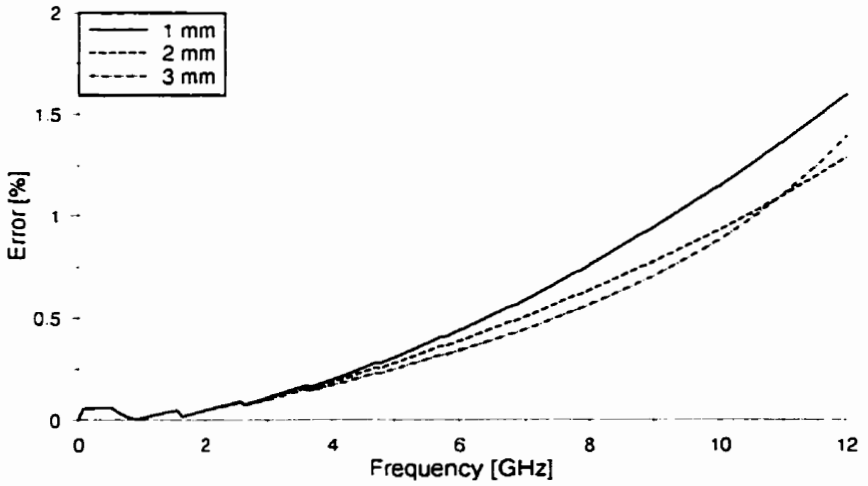

Figure 3.9: TLM reflected error for a thin $\epsilon_r = 5$ dielectric region

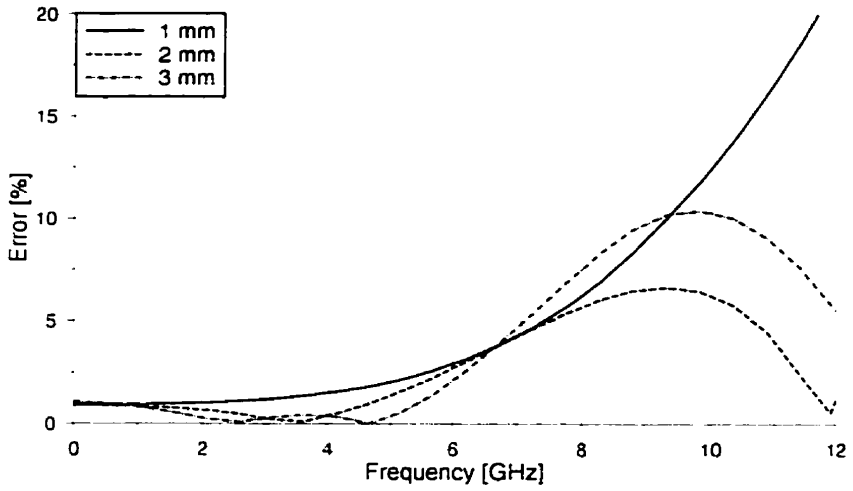

Figure 3.10: HPP-LGA transmitted error for a thin $\epsilon_r = 5$ dielectric region

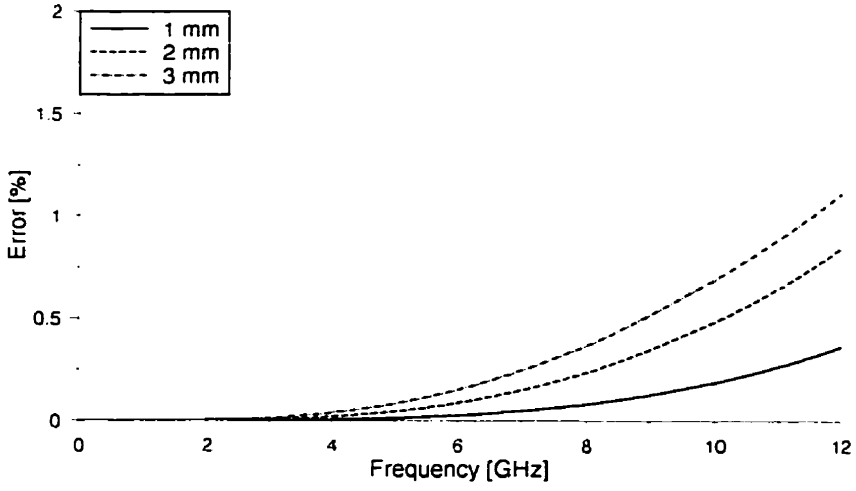

Figure 3.11: TLM transmitted error for a thin $\epsilon_r = 5$ dielectric region

this will show up as an error in the prediction of the reflection or transmission coefficient. This truncation occurs due to difficulty in determining where each waveform originates and terminates within the background noise.

Examination of Figure 3.12 shows that the initial difference between the predicted and analytical values is exaggerated by the division operation in the error calculation. If the differences in the predicted and simulated waveforms are examined instead of the percentage error, the predicted values are shown to be a little more accurate than initially shown. The HPP-LGA waveform differences have been arbitrarily normalized to the peak magnitude of the incident wave. For the sake of comparison, the TLM difference (normalized in a similar manner) peaks at 0.002, which is still an order of magnitude lower than the HPP-LGA results.

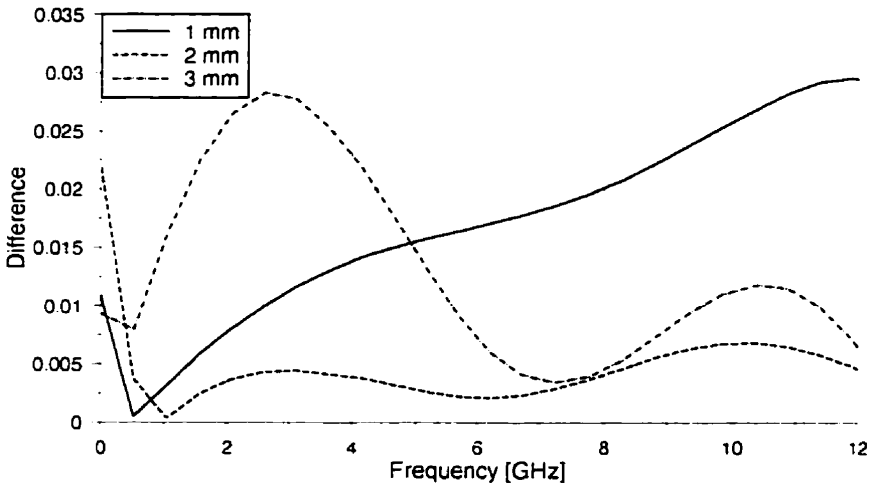

Figure 3.12: Difference between HPP-LGA predicted and analytical reflection coefficient for a thin $\epsilon_r = 5$ dielectric region

The findings in this study suggest that the ratio of HPP-LGA cells to TLM cells

should be higher than 10:1. General discretization rules suggest the minimum size which a fundamental cell should take, such as $1/10\lambda$ for TLM [5] and FDTD [4], and results in an effective and efficient use of computational resources. A discretization ratio should be found which will guarantee an acceptable error. This can be done in conjunction with a study on the effects of file averaging.

3.4 Circular Dielectric Models

Simple spheres are used extensively in the modelling of the human head in three dimensions as discussed in [20], [21] and [22]. This shape manifests itself in a myriad of other applications, but it is not easily modelled. Errors in discretization caused by trying to model a curved surface with a non-conformal grid are commonly referred to as *stair-stepping* errors. In this section the performance of HPP-LGA in predicting the scattering of Gaussian pulsed plane waves incident on circular dielectric objects of various geometry and permittivity is studied. TLM predictions are also provided for comparison. The graphs presented in this section are a small sampling of the extensive set which may be found in Appendices C - J.

Stair-stepping errors will cause predicted results for the system to differ from the true response because of the differences between the desired and actual surfaces, with a larger stair-stepping error associated with the TLM method because the coarser grid it uses. Therefore when comparing HPP-LGA and TLM curves together, the high spatial resolution of HPP-LGA will result in a slightly different system, and possibly different response.

3.4.1 Dielectric Cylinders

A $4096\,\Delta\ell \times 2048\,\Delta\ell$ HPP-LGA lattice was used to simulate the scattering of electric fields off of dielectric cylinders, organized as shown in Figure 3.13. Each lattice had a horizontal periodic boundary condition and a vertical ABC located at $x = 4090\Delta\ell$. A single Gaussian pulsed plane wave[2] with a magnitude of 15% and $\sigma = 200\Delta\ell$, propagating left to right, was used to excite the system. A dielectric cylinder with a radius of $100\Delta\ell$ and an $\epsilon_r = 5$ or 21 was located at $(x, y) = (1024, 1024)\Delta\ell$.

[2] As described in Section 2.3.

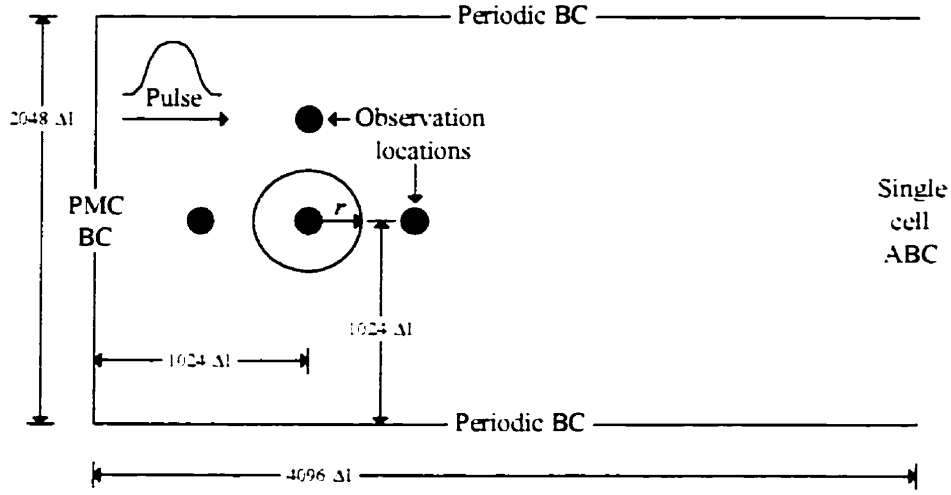

Figure 3.13: Dielectric cylinder simulation space schematic

The electric field at four locations in the lattice was sampled. Three windows were located along the horizontal axis of the dielectric cylinder, with the window to the left of the cylinder located at $(x, y) = (512, 1024)\Delta\ell$, a centre window at $(x, y) = (1024, 1024)\Delta\ell$, and a right window at $(x, y) = (1524, 1024)\Delta\ell$. An additional window was placed above the cylinder at $(x, y) = (1024, 1524)\Delta\ell$.

The radius of the sampling window was a function of its location. The three windows located in free-space had a radius of $50\Delta\ell$. The radius of the sampling window at the centre of the cylinder depended on the dielectric constant of the cylinder. The window inside the $\epsilon_r = 5$ cylinder had a radius of $25\Delta\ell$, while the window inside the $\epsilon_r = 21$ cylinder had a radius of $15\Delta\ell$. The calculated fields from 20 simulations were averaged to create the resulting waveform for each individual case. Figures 3.14 and 3.15 show the predicted HPP-LGA and TLM fields inside two dielectric cylinders, where HPP-LGA has been simplified to LGA in the legend of the graphs.

The electric field at the centre of an $\epsilon_r = 5$ dielectric cylinder is shown in Figure 3.14. The individual peaks of each curve are of similar magnitude, although the

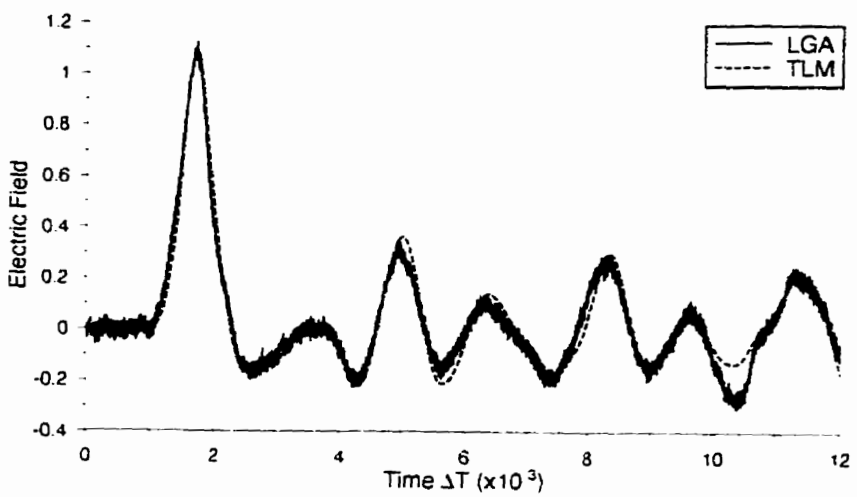

Figure 3.14: Averaged time-domain plot of electric field inside an $\epsilon_r = 5$ dielectric cylinder

HPP-LGA waveform varies significantly from the TLM waveform at approximately $10.000\Delta T$. The initial pulse at $1750\Delta T$ represents the portion of the incident Gaussian pulse which has been transmitted through the curved dielectric interface, and indicates the minute difference which the TLM stair-stepping errors have caused. The HPP-LGA pulse arrives slightly before of the TLM Gaussian pulse, and remains offset from the TLM waveform for the entire simulation, suggesting that this error is due to the window location differences. The $10.000\Delta T$ time value corresponds to the time at which a reflection from the initial pulse on the terminating HPP-LGA ABC arrives back at the centre of the cylinder.

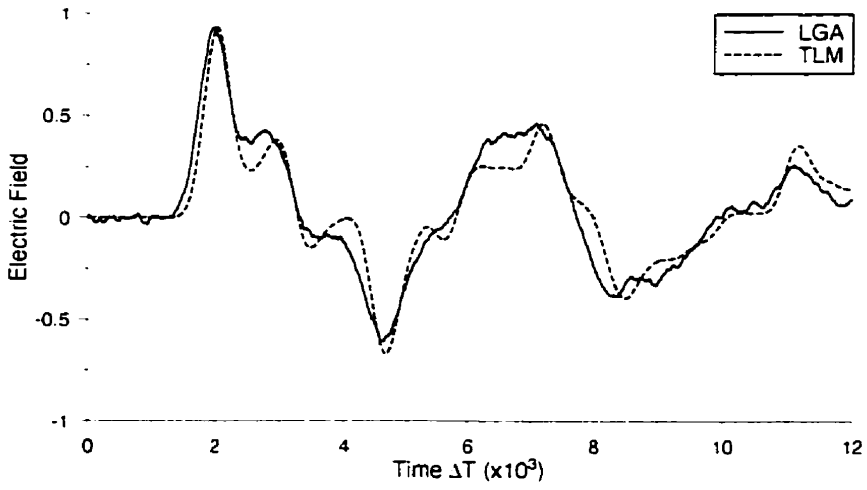

Figure 3.15: Averaged time-domain plot of electric field inside an $\epsilon_r = 21$ dielectric cylinder

Figure 3.15 presents the electric field inside an $\epsilon_r = 21$ dielectric cylinder. The increase in the dielectric constant of the cylinder has manifested itself into an increased temporal shift in the transmitted pulse as compared to Figure 3.14. The increased

dielectric constant will also amplify the TLM stair-stepping error, and increase the differences between the two systems. The fluctuations in the TLM prediction appear to have been averaged by the HPP-LGA window. This effect is most noticeable before $7.000\Delta T$.

3.4.2 Dielectric Annuli

An HPP-LGA lattice of size $4096\,\Delta\ell \times 2048\,\Delta\ell$ with a horizontal periodic boundary condition and a vertical ABC located at $x = 4090\Delta\ell$ was used in the simulation of the scattering of a electric fields off of dielectric annuli (rings) as shown in Figure 3.16. A single Gaussian pulsed plane wave, propagating left to right with a magnitude of 15% and $\sigma = 200\Delta\ell$, was used to excite the system. A dielectric annulus with an outer radius of $100\Delta\ell$ and inner radius of either $80\Delta\ell$ or $50\Delta\ell$ was located at $(x, y) = (1024, 1024)\Delta\ell$ with a dielectric constant of $\epsilon_r = 5.21$ or 85.

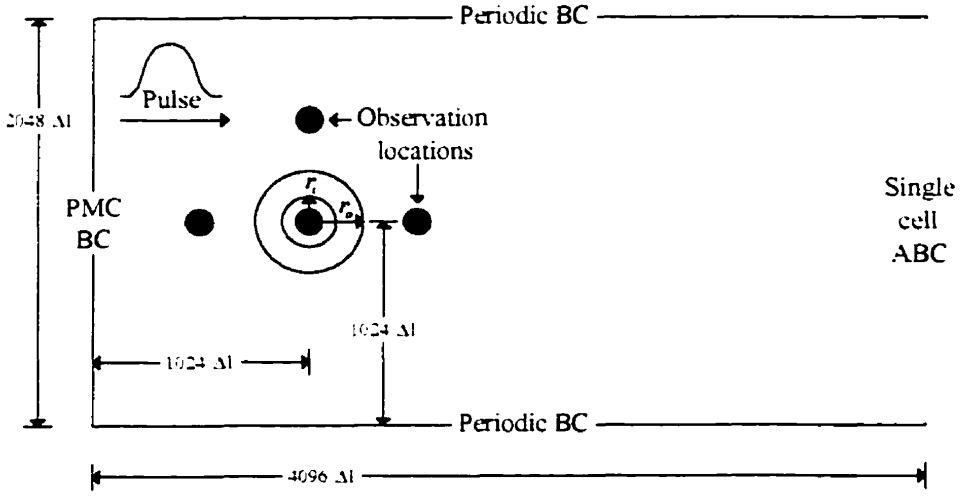

Figure 3.16: Dielectric annulus simulation space schematic

The time-domain scattered field-intensity was predicted at four points around and inside each annulus. The left sampling window was located at $(x, y) = (512, 1024)\Delta\ell$,

the window inside the annulus was located at $(x, y) = (1024, 1024)\Delta\ell$, the window above the annulus was located at $(x, y) = (1024, 512)\Delta\ell$ and the the window to the right of the annulus was located at $(x, y) = (1524, 1024)\Delta\ell$. All sampling window radii were $50\Delta\ell$. The calculated fields from 20 simulations were averaged to create the resulting waveform for each individual case. The results at the centre of an $\epsilon_r = 5$ and 85 annulus are shown in Figures 3.17 and 3.18.

Figure 3.17 shows the predicted electric field inside an $\epsilon_r = 5$ dielectric annulus with an inner radius 0.8 of the outer radius. The TLM and HPP-LGA curves are nearly identical in this simulation, with significant differences appearing after $10,000\Delta T$ due to reflections from the imperfect HPP-LGA ABC. Overall, the small discrepancies between the two curves can be attributed to the spatial averaging that occurs in the HPP-LGA method.

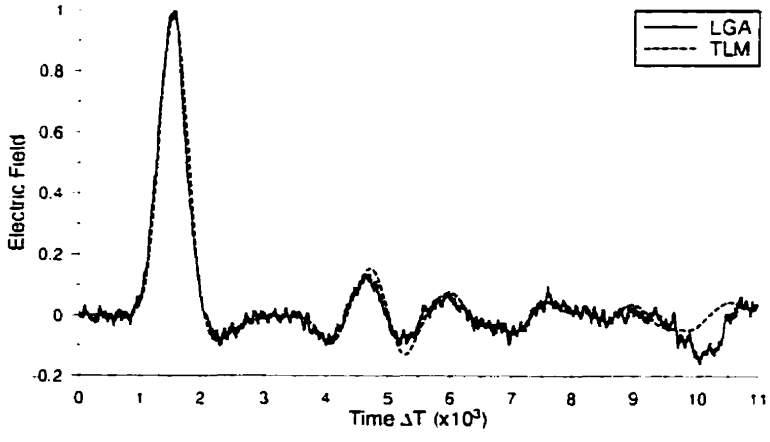

Figure 3.17: Averaged time-domain plot of electric field inside an $\epsilon_r = 5$ dielectric annulus ($R_i = 80\% R_o$)

The field inside an $\epsilon_r = 85$ annulus is shown in Figure 3.18, where the inner

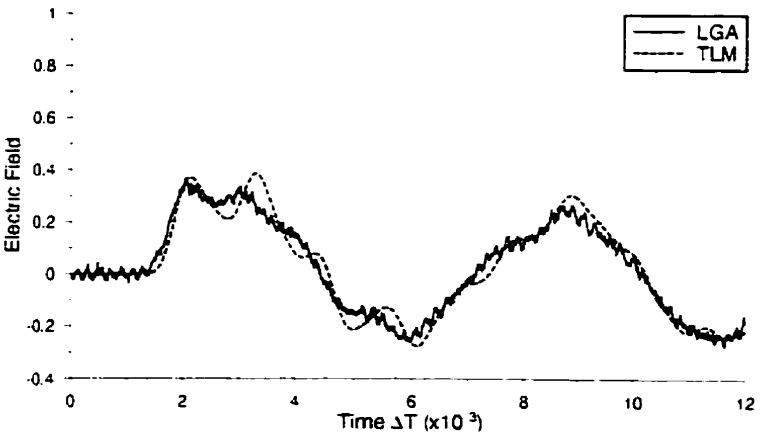

Figure 3.18: Averaged time-domain plot of electric field inside an $\epsilon_r = 85$ dielectric annulus ($R_i = 50\% R_o$)

radius is 0.5 of the outer. The spatial averaging in HPP-LGA once again appears to be averaging out the oscillations in the waveform as predicted by the TLM simulation, although the general shape of each waveform is similar. A difference between the HPP-LGA and TLM predictions is the contradiction which occurs at $3000\Delta T$ regarding a peak in the waveform. This discrepancy may be caused by the stair-stepping error present in the TLM model.

3.4.3 Discussion

Judgment of the performance of HPP-LGA relative to TLM based on the similarity of corresponding electric field curves should be made with the knowledge that the HPP-LGA and TLM electric fields were sampled at slightly different spatial locations. HPP-LGA field sampling windows were positioned $512\Delta\ell$ away from the centre of the circular model in various directions. In accordance with [19], a 10:1 HPP-LGA

cell to TLM cell discretization ratio was used, which resulted in the field sampling locations not matching up exactly.

Overall, the HPP-LGA and TLM curves appear to be predicting the same fields, but the spatial averaging present in HPP-LGA simulations often causes the high-frequency oscillations in the electric field to become dampened while retaining similar predictions of peak magnitudes. The two method's field sampling locations are not exactly at the same place, and this manifests itself into differences in when portions of the waveforms arrive. The presence of the HPP-LGA ABC causes errors near the end of the simulations relative to the strength of the field incident on it.

The incident HPP-LGA and TLM Gaussian pulses need to propagate through two curved dielectric interfaces before they reach the centre of each annulus. This will cause larger differences between the methods than in the simulations of the dielectric cylinders due to the stair-stepping errors present in the TLM discretization of the dielectric annuli.

3.5 Electric Field Distribution Inside a Dielectric Cylinder

In this section the steady-state electric field distribution inside a cylinder with a dielectric constant of $\epsilon_r = 21$ is predicted using HPP-LGA and TLM. To study the possible effects that the viscosity inherent in HPP-LGA may have on the field distribution, TLM simulations of cylinders with varying conductivity values are presented.

3.5.1 Background

The HPP-LGA calculation of field strength involves the spatial averaging of particles in a number of cells around a particular location, as explained in Section 2.1.2. To accomplish this for every cell in the the dielectric cylinder, the state of the complete lattice in the CAM-8 had to be stored to auxiliary memory on a workstation at each desired timestep, and then analyzed separately. Figure 3.19 summarizes the pre- and post-processing steps involved in the determination of the field density.

Pre- and post-processing are done on serial machines while only the simulation itself involves the CAM-8. Pre-processing involves creating an input pattern to be merged into the regular CAM-8 input file, and saving the attributes of each cell of the created pattern in auxiliary files which will be used in the post-processing stage. Simulation with the CAM-8 is a simple procedure, only slightly complicated by the need to output the complete state of the HPP-LGA lattice at various timesteps.

Post-processing involves identifying the area of interest in the lattice, and then computing the field strengths at each point and each timestep, using the necessary files created in the pre-processing stage. Once the field strengths have been determined at each timestep, the maximum field strength at each cell location is found by searching the timesteps for the maximum field at each particular cell. The goal of this HPP-LGA

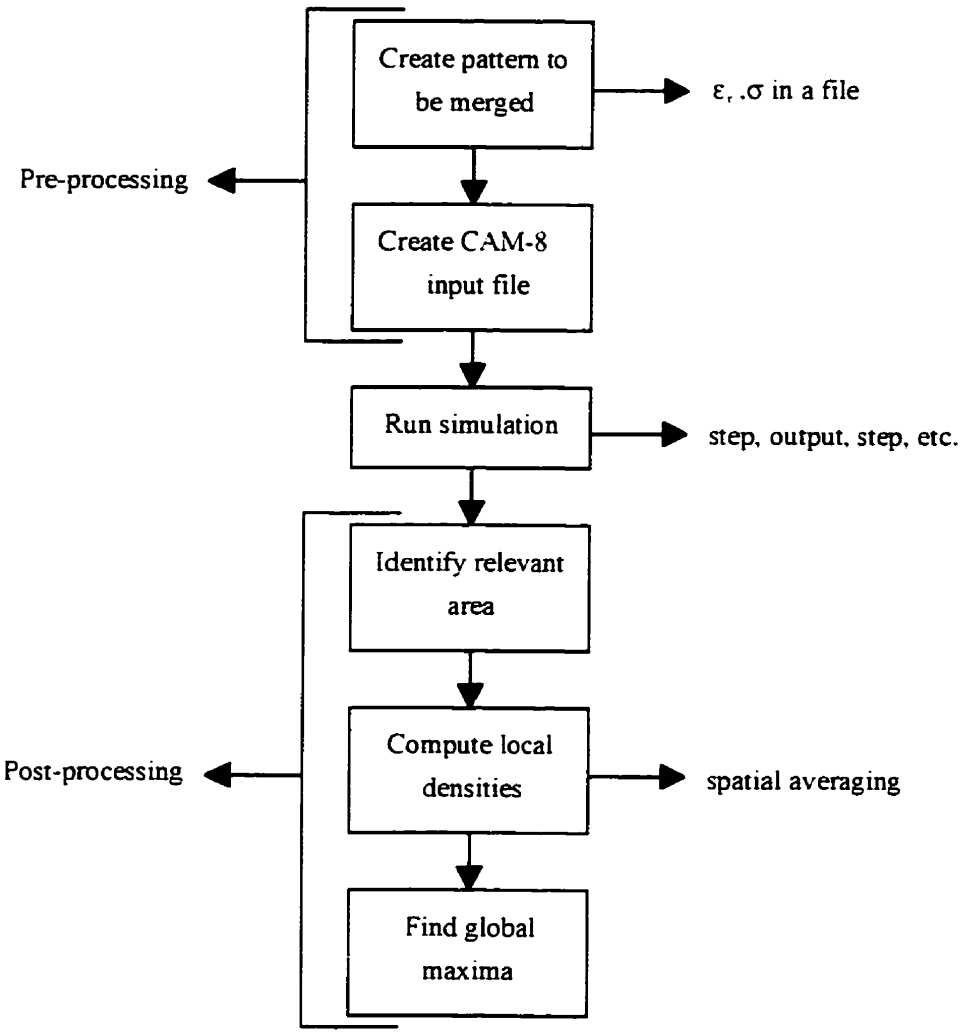

Figure 3.19: Computational steps for general HPP-LGA field distribution predictions

simulation can be defined as determining the maximum field at each point inside the dielectric cylinder in its steady state, over a complete period of the incident electric field.

Ideally, the state of the entire lattice at each timestep would be examined, but because of the amount of data that this represents the lattice is often sampled at a regular interval. This reduces the amount of data significantly although the predictions will not be as accurate as if each timestep was examined.

3.5.2 Geometry Description

The HPP-LGA simulation was performed in a $4096\,\Delta\ell \times 2048\,\Delta\ell$ lattice with a horizontal periodic boundary condition and a single cell ABC located at $4000\Delta\ell$. A continuous sinusoidal wave[3] with a magnitude of 10% and $\lambda_{BS} = 1024\Delta\ell$ was launched from the beginning of the lattice. An $\epsilon_r = 21$ dielectric cylinder with a radius of $145\Delta\ell$ was centered at $(x, y) = (3000, 1024)\Delta\ell$. The cylinder radius of $145\Delta\ell$ translates into $\frac{\lambda_{CS}}{5}$. The simulation was evolved for $15,000\Delta T$ to allow the wave transients to decay, and then 10 samples of the state of the lattice were taken, equally spaced at $100\Delta T$. The spatial window used to extract the field information at each cell inside the cylinder had a radius of $21\Delta\ell$.

Four TLM simulations were performed. The TLM cylinders were placed in a lattice of size $300\,\Delta\ell \times 210\,\Delta\ell$ with each cylinder located at $(x, y) = (226, 102)\Delta\ell$. The radius of the cylinders were $10\Delta\ell$, which corresponded to a size of 70.6 mm, and had conductivity values of $\sigma = 0.000\ \frac{S}{m}$, $0.009\ \frac{S}{m}$, $0.094\ \frac{S}{m}$ and $1.275\ \frac{S}{m}$.

[3] As discussed in Section 2.3.

3.5.3 Results

Lossless Dielectric Cylinders

Using the simulation parameters as described previously, and the method as described in Figure 3.19, the HPP-LGA predicted field distribution inside an $\epsilon_r = 21$ dielectric cylinder is shown in Figure 3.21. The TLM result is shown in Figure 3.22, with the wave incident on the right side of the cylinder in both figures. Each prediction has been normalized with respect to its largest value, with the image colour levels corresponding to the values as indicated in Figure 3.20.

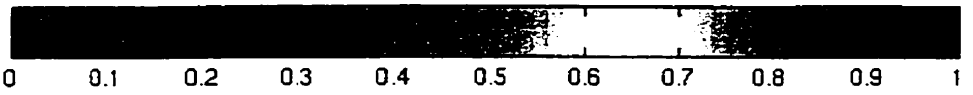

Figure 3.20: Colourbar and corresponding numerical values

The HPP-LGA and TLM predicted electric field distributions are in reasonable agreement with each other in both shape and magnitude. Both methods are symmetric about the horizontal axis and show signs of the incident wave at the right side of the cylinder. Areas of high field concentration exist on either side of centre, with the primary one located to the left. The circular HPP-LGA primary concentration varies slightly from the elliptical TLM prediction. The HPP-LGA secondary area of field concentration, located to the right of centre, has the same elliptical shape as the TLM prediction but lacks the concave form.

A major difference between the two predictions is the significant field level located at the left side of the TLM cylinder. This may be caused by the TLM stair-stepping error. The TLM discretization of the dielectric cylinder results in essentially an octagon with the flat surfaces slightly altered by a single cell at their centre. This model is very different than the HPP-LGA model, which more accurately represents

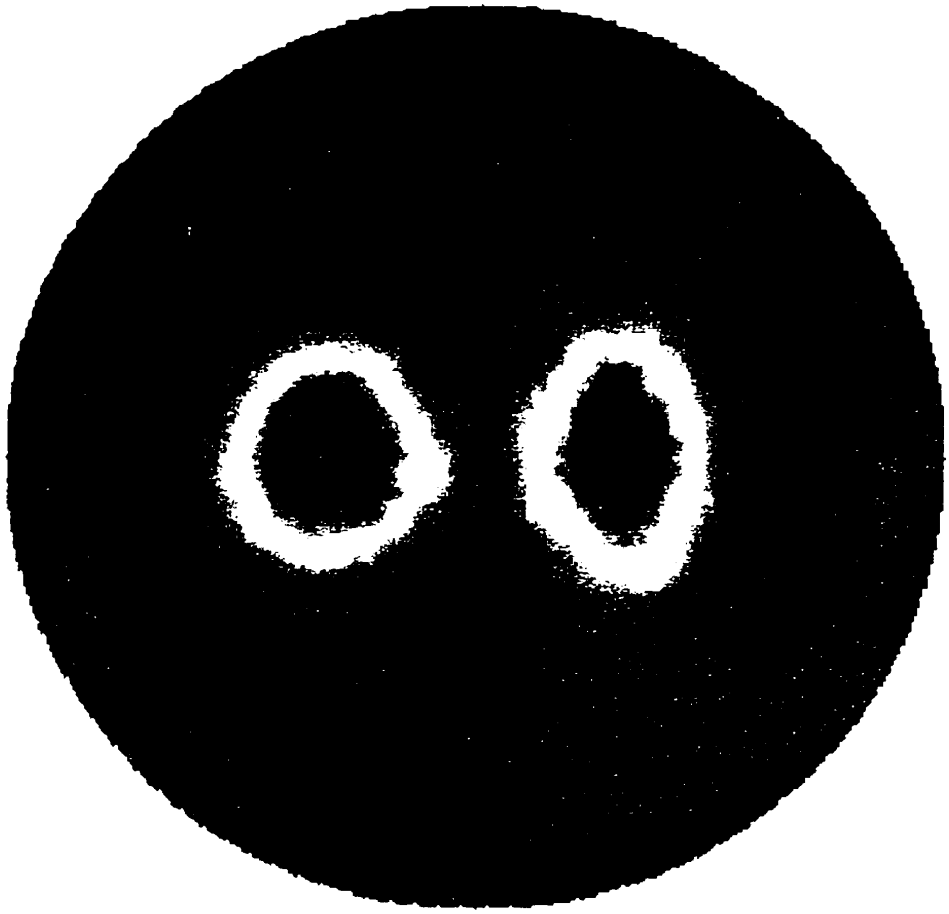

Figure 3.21: HPP-LGA predicted electric field distribution inside an $\epsilon_r = 21$ cylinder

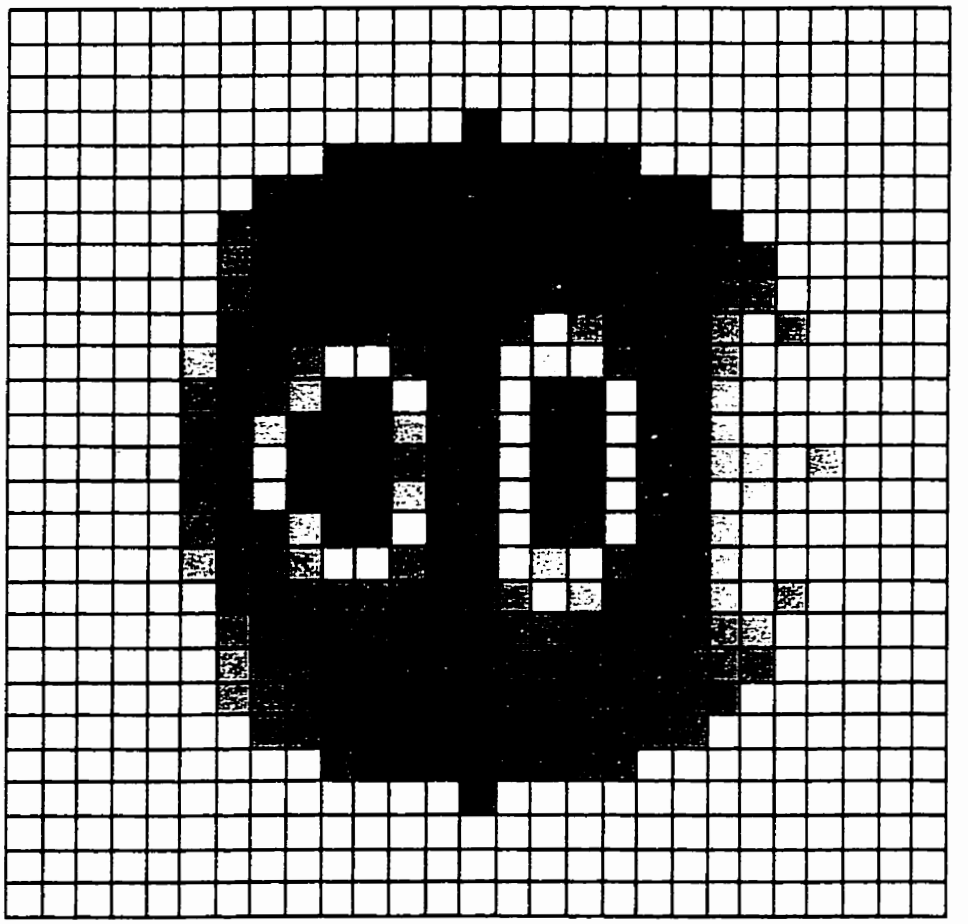

Figure 3.22: TLM predicted electric field distribution inside an $\epsilon_r = 21$ cylinder

the cylinder geometry as a direct consequence of the HPP-LGA high discretization ratio.

Lossy Dielectric Cylinders

In this section the effect on the distribution of the electric field inside a dielectric cylinder due to variations in conductivity is examined. This study was conducted in an effort to extrapolate the possible effects which the anisotropic viscosity in HPP-LGA may have in the prediction of electromagnetic wave phenomena.

The effect of including conductivity, σ, into Maxwell's curl equations[4] (Equations 3.7 and 3.8) results in an expression for the propagation constant γ which includes σ and ϵ.

$$\nabla \times \mathbf{E} = -j\omega\mu\mathbf{H} \tag{3.7}$$

$$\nabla \times \mathbf{H} = \mathbf{J} + j\omega\epsilon\mathbf{E} \tag{3.8}$$

$$= (\sigma + j\omega\epsilon)\mathbf{E} \tag{3.9}$$

The propagation constant as shown in Equation 3.10 consists of a real part α (attenuation constant), which represents an exponential decrease in wave amplitude with distance, and an imaginary part β (phase constant), which represents the radian phase shift as it propagates through the media [23].

$$\gamma = \alpha + j\beta \tag{3.10}$$

$$= j\omega\sqrt{\mu\epsilon}\sqrt{1 - j\frac{\sigma}{\omega\epsilon}} \tag{3.11}$$

[4]Assuming sinusoidal time variation.

The attenuation constant α is a function of the material conductivity (σ), permittivity ($\epsilon = \epsilon_r \epsilon_0$) , permeability ($\mu = \mu_r \mu_o$) and frequency of interest ($\omega = 2\pi f$). A material with $\sigma = 0$ does not have any loss inherent to it, and therefore $\alpha = 0$.

The additional TLM simulations dealing with the effects of variations in conductivity on the distribution of the electric field are shown in Figures 3.23, 3.24 and 3.25. Slight variations in conductivity do not appear to have a major effect on the distribution of the electric field inside the dielectric cylinders. Each simulation predicts essentially the same distribution. The two highest concentrations of electric field, located to the left and right of centre of the cylinder, are in similar sites despite the variations in conductivity. The primary concentration remains the same size and relative magnitude throughout the three simulations, while the intensity of the secondary concentration decreases as σ increases. The remaining field is more evenly distributed throughout the cylinder as σ increases.

With regards to the HPP-LGA method itself, the effect of viscosity on the distribution of fields in homogeneous dielectric models does not appear to be a major factor. There is little variation between the three TLM results and the HPP-LGA prediction.

A method of simulating the conductive properties of dielectric media has yet to be developed, and therefore the use of HPP-LGA in the simulation of electromagnetic wave phenomena is limited to interactions with low loss media. The electric field distribution inside a lossy dielectric cylinder was simulated, with $\sigma = 1.275 \frac{S}{m}$, with the TLM prediction shown in Figure 3.25.

The original field distribution as predicted by HPP-LGA in Figure 3.21 is very different from the $\sigma = 1.275\ \frac{S}{m}$ cylinder in Figure 3.25. The increased conductivity in the TLM cylinder has increased the magnitude of the attenuation factor, and this has caused the magnitude of the wave to decrease very quickly as it propagates through

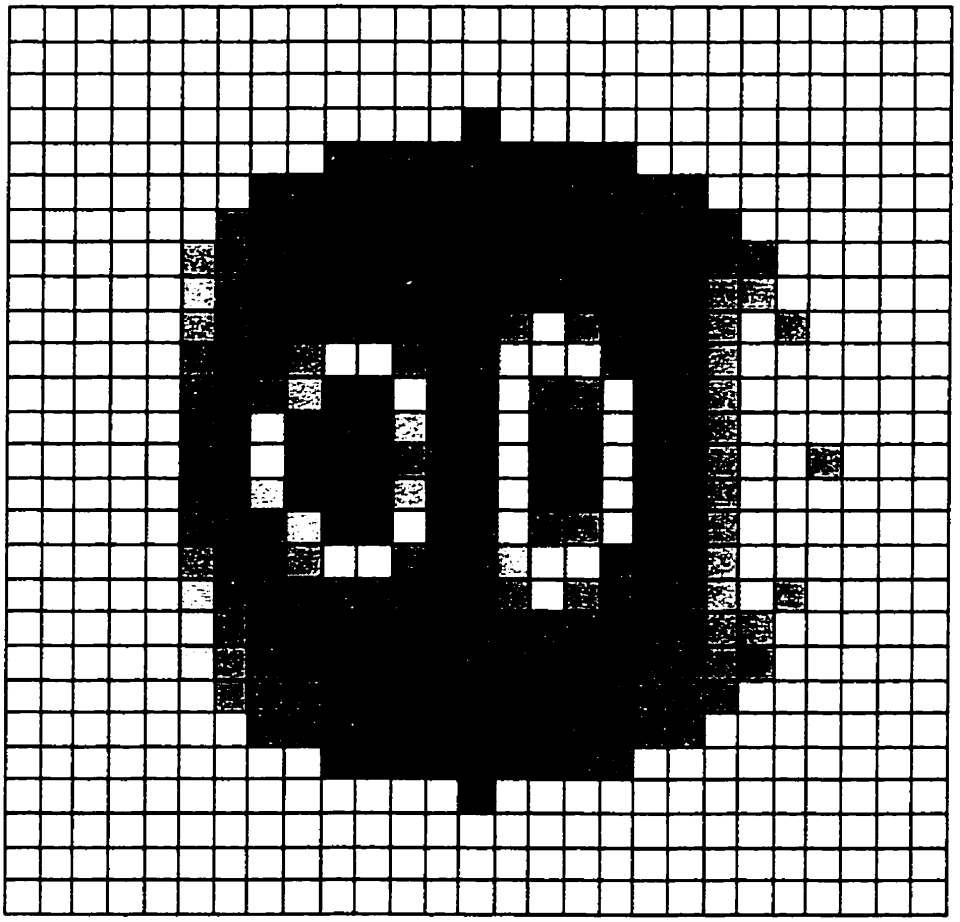

Figure 3.23: TLM predicted electric field distribution inside an $\epsilon_r = 21$, $\sigma = 0.009\ \frac{S}{m}$ cylinder

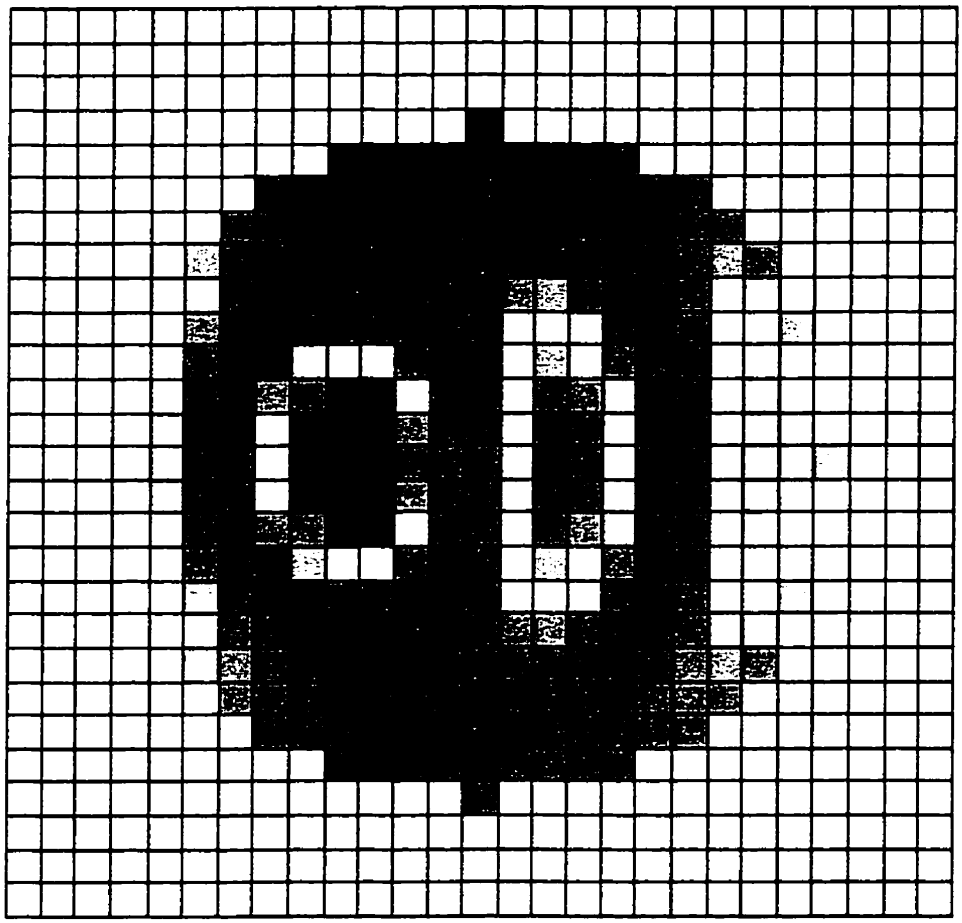

Figure 3.24: TLM predicted electric field distribution inside an $\epsilon_r = 21$, $\sigma = 0.094\ \frac{S}{m}$ cylinder

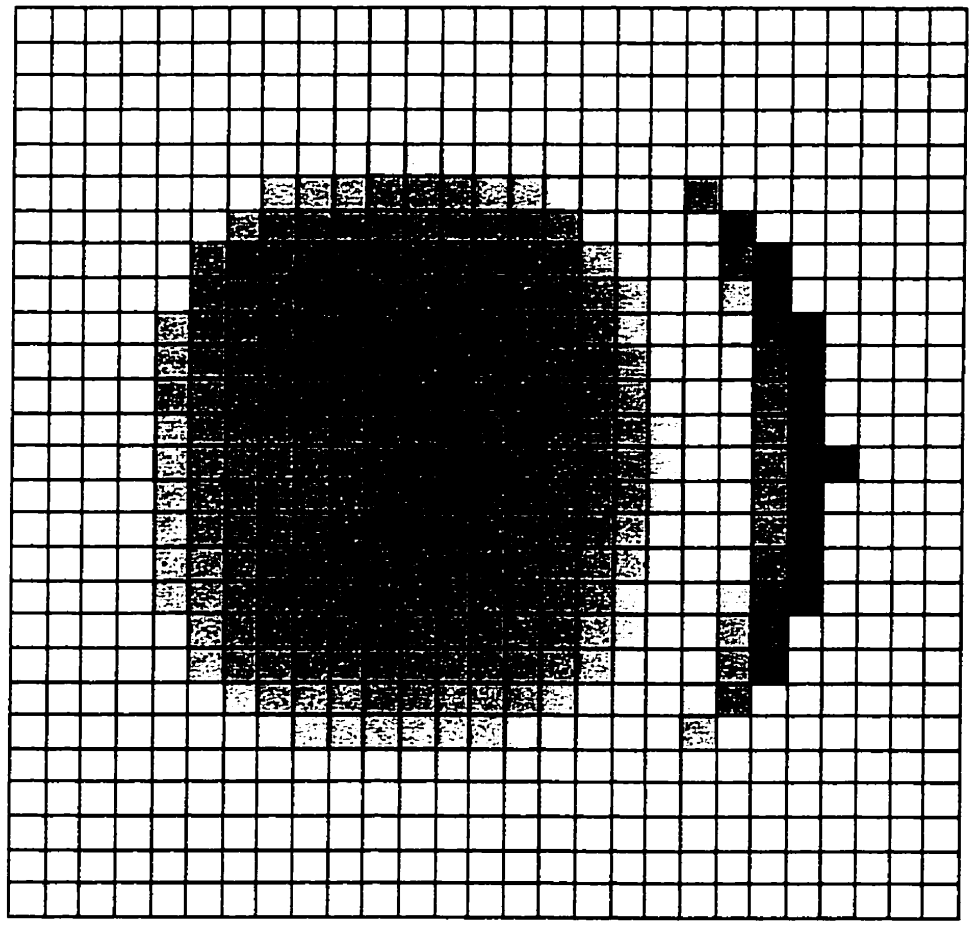

Figure 3.25: TLM predicted electric field distribution inside an $\epsilon_r = 21$, $\sigma = 1.275\ \frac{S}{m}$ cylinder

the cylinder.

Chapter 4

Wave Interaction With Biological Media

Regulatory codes regarding standards of safety for the use of radiating devices such as the Canadian Safety Code 6 [24] and the Federal Communications Commision's "Guidelines for Evaluating the Environmental Effects of Radiofrequency Radiation" [25] cannot cover all possible situations where humans, wireless devices and electronic equipment interact. For this reason it is important to have numerical and experimental methods with which electromagnetic fields which could be present in the human body can be pre-determined. With such information, the possible consequences from electromagnetic interaction between electronic devices, such as pacemakers, cellular phones and hearing aids, as well as the possible effects fields may have to the human body itself can be extrapolated.

This chapter describes the process involved in modelling and simulating a human torso using HPP-LGA. It also demonstrates limitations to the HPP-LGA method arising from the current inability to model lossy media. An early version of this study may be found in [26].

4.1 Body Model

The human body model used in the HPP-LGA simulation of biological media is shown in Figure 4.1. Provided by the University of Victoria [27], this model was initially discretized for use with the Finite-Difference Time-Domain (FDTD) method. Each cell has an approximate resolution of 3.33 mm, and the dimensions of the cross-section are 147×87. This model represents a horizontal cut through the chest of a human, just below the heart. The front of the body is placed at the top of the figure.

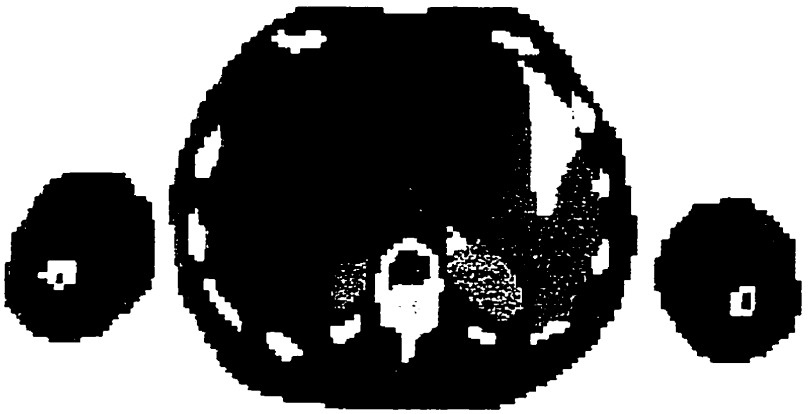

Figure 4.1: Theoretical cross section of human torso

Figure 4.2 is a cross-section of a real human body [28], and is provided as a comparison to the discretized model. While the overall shape of the FDTD model is similar to the real body image, small details present in the actual body are missing. Additionally, stair-stepping errors are present throughout the body model.

The FDTD body model was mapped to a larger lattice with an FDTD to HPP-LGA cell increase of 6:1. Although the HPP-LGA model is larger, the geometry and discretization of fine structures is no more accurate than the original because the original errors in discretization have been passed on to the larger mesh. It is will be shown later in this chapter (Section 4.4) how the high spatial resolution of HPP-LGA

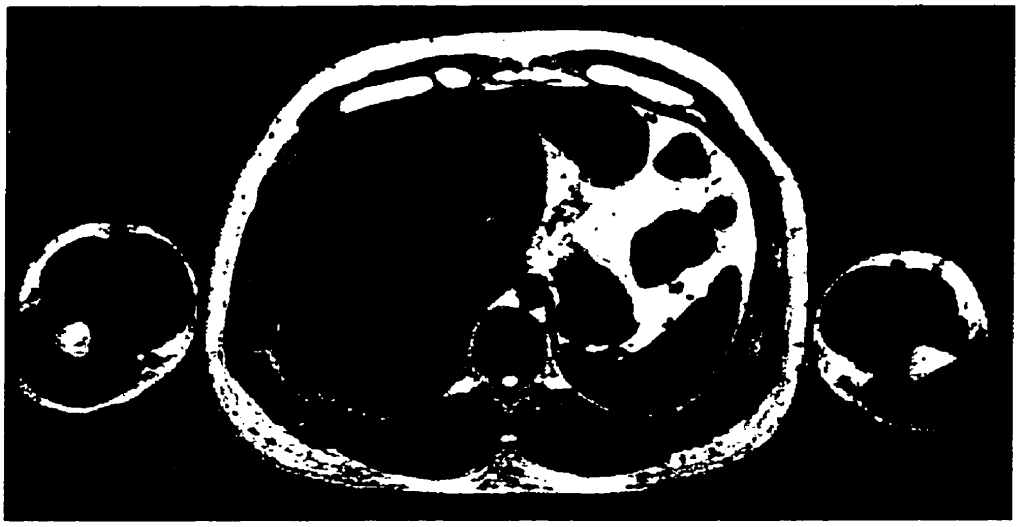

Figure 4.2: Actual cross-section of human torso

can be used to more accurately model fine structures. With the increase in size for the HPP-LGA model, each HPP-LGA cell has a resolution of 0.55 mm. Based on current studies into the relative cell sizes of TLM [19], FDTD [29] and HPP-LGA, the HPP-LGA model should have been increased to at least 15 times the original FDTD model size. A higher discretization was not used due to the relationship between cell size and continuous time-domain source frequency as explained in Section 2.3.2. It was also necessary to limit the overall size of the body with respect to the lattice because of the possible interaction of scattered fields with the body model across the periodic boundary, and from reflections from the truncating ABC boundary condition.

A labeled version of Figure 4.1 is provided in Figure 4.3, except for two omissions due to a lack of space. The spine, which is the white structure surrounding the spinal cord (3), has not been labeled. Additionally, bone marrow, which is contained in the chamber adjacent to the spinal cord, has been left out. Bone marrow can also be found in the bones of both arms (only one arm has been labeled). Identification of body parts can be done through Table 4.1 which contains the electrical parameters

used in analysis and simulation of the body, as found for a frequency of 915 MHz. The rest particle mixing ratios used to model the dielectric regions as described in Section 2.2.3 is also provided.

The highly inhomogeneous body model contains ϵ_r values ranging from 6.0 (adrenals and fat) up to 62.0 (blood, spleen and lessions[1]). From the point of view of dielectric constant, the right side of the body is comprised of a large region with $\epsilon_r = 43$. The left side of the body, essentially the liver, is slightly larger in size, and has a higher dielectric constant of $\epsilon_r = 48$. The body model is simulated at a frequency of 850 MHz. Although the dielectric properties of the various materials in the body are obtained for a frequency of 915 MHz, it is assumed that material properties are unaffected by the change in frequency.

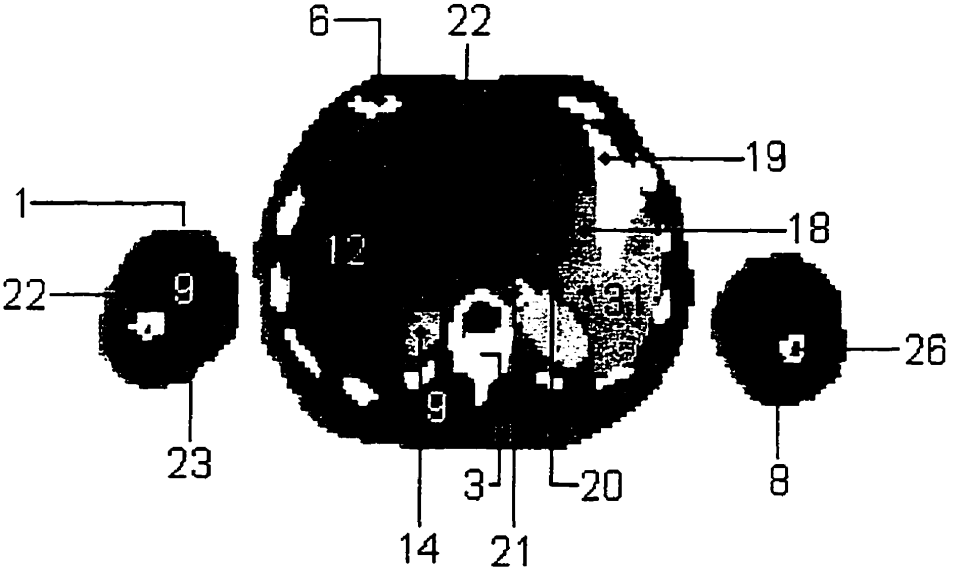

Figure 4.3: Labeled theoretical cross section of human torso

[1]A lession is defined as [30] "Any visible abnormality of the tissue" and may be described as "cancerous, gross ... bloody". For this reason it was assigned the same value as blood.

Table 4.1: Body materials: markers. ϵ_r. σ. ρ_g and mixture ratios

Material	Marker	ϵ_r	$\sigma \left[\frac{S}{m}\right]$	$\rho_g \left[10^3 \frac{kg}{m^3}\right]$	Mixture
skin	1	35.0	0.60	1.01	21.88% (7. 3)
spinal cord	3	49.0	1.10	1.04	43.75% (7. 3)
spine		8.0	0.11	1.81	18.75% (3. 1)
ribs	6	8.0	0.11	1.81	18.75% (3. 1)
long bones	8	8.0	0.11	1.81	18.75% (3. 1)
skeletal muscle	9	58.0	1.40	1.04	57.81% (7. 3)
liver	12	48.0	0.97	1.00	42.19% (7. 3)
kidney	14	43.0	0.90	1.00	34.38% (7. 3)
stomach	17	43.0	0.90	1.00	34.38% (7. 3)
small bowel	18	43.0	0.90	1.00	34.38% (7. 3)
colon	19	43.0	0.90	1.00	34.38% (7. 3)
pancreas	20	43.0	0.90	1.00	34.38% (7. 3)
adrenals	21	6.0	0.08	1.00	6.25% (3. 1)
fat	22	6.0	0.08	0.92	6.25% (3. 1)
blood	23	62.0	1.50	1.06	62.06% (7. 3)
bone marrow	26	42.0	0.80	1.00	32.81% (7. 3)
spleen	31	62.0	1.50	1.00	62.06% (7. 3)
lession	63	62.0	1.50	1.00	62.06% (7. 3)

Table 4.2 provides the sources for Table 4.1. The three sources are *Email.* which refers to [27]. *GAN* which refers to [31]. and *STU* which corresponds to [20]. Also included in Table 4.2 is an alternative mixture ratio for the body model using the Partial R_{Max} rest particles from Section 2.2.2. which will be discussed later in this chapter.

4.2 Specific Absorption Rate

One way to quantify the effects of exposure to electromagnetic fields on the human body is through the determination of the *Specific Absorption Rate* (SAR). The SAR can be established by measuring either the magnitude of the electric field $|E|$. or the temperature rise $\frac{\partial T}{\partial t}$ inside exposed tissue. The Specific Absorption Rate (SAR) as defined by the Health and Welfare Canada Safety Codes [24] is:

> The time derivative (rate) of the incremental energy (dW) absorbed by an incremental mass (dm) contained in a volume element (dV) of a given density (ρ_g).
>
> $$SAR = \frac{d}{dt}\left[\frac{dW}{dm}\right] = \frac{d}{dt}\left[\frac{dW}{\rho_g dV}\right] \tag{4.1}$$
>
> SAR is expressed in units of Watts per kilogram (W/kg). Also:
>
> $$SAR = \frac{|E_i|^2\sigma}{\rho_g} \tag{4.2}$$
>
> where: σ is the tissue conductivity (S/m). E_i is the rms electric field strength in the tissue (v/m) and ρ_g the mass density (kg/m^3).

The SAR is given as a measure of electromagnetic absorption over a region of the body. and after averaging over a predetermined amount of body mass. the resulting

Table 4.2: Body materials: information sources and alternative mixtures

Material	Marker	Source ϵ_r	Source σ	Source ρ_g	Alternative Mixture
skin	1	Email	Email	GAN	9.95% (5. 4)
spinal cord	3	Email	Email	GAN	29.27% (6. 5)
spine		Email	Email	GAN	50.00% (2. 1)
ribs	6	Estimate	Estimate	GAN	50.00% (2. 1)
long bones	8	Estimate	Estimate	GAN	50.00% (2. 1)
skeletal muscle	9	Email	Email	GAN	9.88% (7. 6)
liver	12	Email	Email	Estimate	17.56% (6. 5)
kidney	14	Email	Email	Estimate	72.59% (5. 4)
stomach	17	Estimate	Estimate	Estimate	72.59% (5. 4)
small bowel	18	Estimate	Estimate	Estimate	72.59% (5. 4)
colon	19	Estimate	Estimate	Estimate	72.59% (5. 4)
pancreas	20	Email	Email	Estimate	72.59% (5. 4)
adrenals	21	Estimate	Estimate	Estimate	16.67% (2. 1)
fat	22	Email	Email	GAN	16.67% (2. 1)
blood	23	Email	Email	GAN	23.23% (7. 6)
bone marrow	26	STU	STU	Estimate	64.76% (5. 4)
spleen	31	Email	Email	Estimate	23.23% (7. 6)
lession	63	Estimate	Estimate	Estimate	23.23% (7. 6)

values are compared to the various regulatory standards for compliance. The Canadian Safety Code [24] states that any method which can determine the SAR within $\pm 20\%$ may be used, analytical or experimental.

4.3 Simulation

Simulation of the body cross-section model was done on a $4096\Delta\ell \times 2048\Delta\ell$ lattice with a horizontal periodic boundary condition and an ABC at $4000\Delta\ell$. A continuous sinusoidal wave with a magnitude of 10% and $\lambda_{BS} = 1024\Delta\ell$ was launched from the beginning of the lattice, incident on the front of the body. A schematic of this simulation is shown in Figure 4.4.

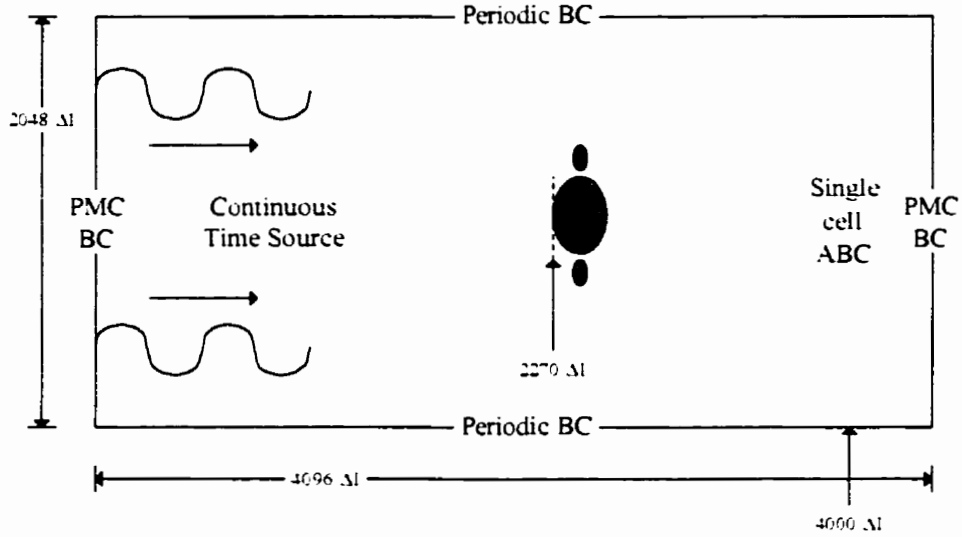

Figure 4.4: Wave interaction with biological media simulation space schematic

The front edge of the body was located at $2270\Delta\ell$. The simulation was evolved for $15,360\Delta T$ to allow the wave transients to decay, and then 11 samples of the state of the lattice were taken, equally spaced at $100\Delta T$. A circular window with a radius

of $21\Delta\ell$ was used to determine the field values at each cell inside the body. The conceptual steps used to obtain the field values are exactly the same as shown in Figure 3.19. The predicted electric field distribution is shown in Figure 4.5, with the field distribution corresponding to the colourbar as shown in Figure 3.20. As stated earlier, the front of the body is at the top of the figure.

Figure 4.5: HPP-LGA predicted electric field distribution for incident time harmonic wave ($f = 850MHz$)

There is a gradual increase in field density from the perimeter of the body model in towards the centre. The dielectric symmetry of the inner organs manifests itself in the field distribution of Figure 4.5. The fields on either side of the body are very similar, with an exception occurring near the front where the liver extends across centre. Regions of low field concentration correspond to bones and various pockets of fat throughout the body.

Of particular interest is the high concentration of fields at the back of the arms, and the horizontal band across the right arm. These fields may be due to reflections from the ABC, or perhaps scattered fields from the front of the body which have passed across the periodic boundary condition and transmitted into the arms.

The SAR is estimated by identifying each region and its σ and ρ_g as identified in Table 4.1, and using Equation 4.2. The resulting image is shown in Figure 4.6. It should be noted that while the body model as modelled by HPP-LGA is accurate with respect to the dielectric constants of the various materials, the conductive properties have not been included, and therefore the model is lossless (other than losses due to the viscosity intrinsic to the method itself).

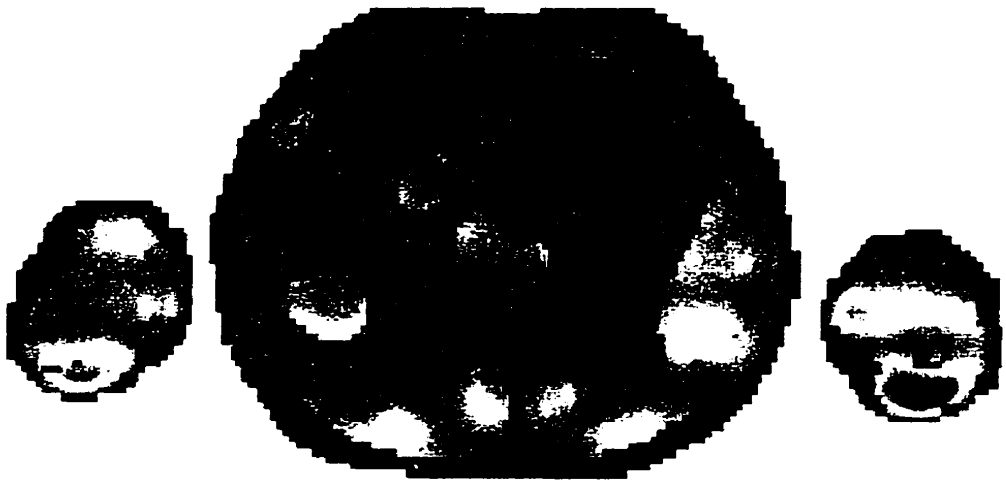

Figure 4.6: HPP-LGA predicted SAR for incident time harmonic wave ($f = 850MHz$)

The blocks of dielectric regions as mentioned earlier are more evident once σ has been introduced. Most of the hotspots predicted in the field distribution have disappeared, leaving some high fields in the spleen and back. The arms remain the site of the highest fields due to the high value of σ attributed to skeletal muscle.

4.4 Discussion

There are two significant reasons why the accuracy of the predicted electric field distribution should be questioned. The body model was increased to only 6 times its original size so that it would exist in a large open-spaced region and thus prevent scattered fields from interacting with the body model across the periodic boundary. As stated in Section 4.1, the body model should have been increased to at least 15 times its original size. Nevertheless, the fields at the rear of the arms suggest that the scattered fields have propagated across the periodic boundaries. It is interesting to note that the high fields at the back of the arms are similar to those found at the rear of the low conductivity TLM dielectric cylinders in Section 3.5.

The high spatial resolution of HPP-LGA is very useful for the modelling of complex geometrical structures. In addition to the circular nature of the basic body and arms models used in this chapter, there are many internal organs which are subject to stair-stepping errors. An example of the modelling capability of HPP-LGA is demonstrated in Figure 4.7, where two arm models are provided.

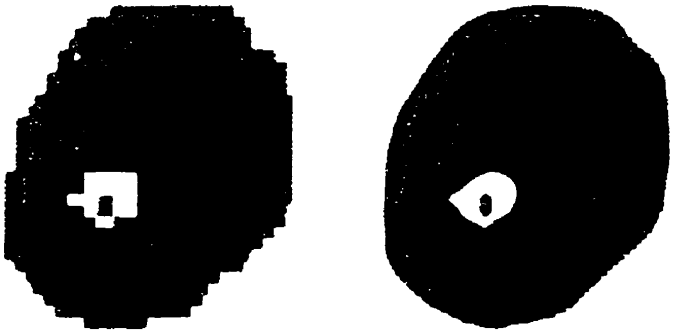

Figure 4.7: FDTD and LGA human arm discretization

The arm on the left is the original FDTD arm from Figure 4.1, while the right

arm is a smoothed version created by mapping the original arm to a lattice 8 times finer. The original discretization errors have been improved significantly as can seen in the contour of the skin around the arm.

The alternative mixtures as presented in Table 4.2 are possible improvements in the modelling of the human body dielectric values. By employing the measured Partial R_{Max} ϵ_r values as described in Section 2.1.4, the difference between two successive ϵ_r values is minimized. The alternative mixture formulation presented in Table 4.2 is presented as a possible improvement, since any particular mixture formulation has not been shown to be more accurate than any other. Before this particular mixture is implemented the theory regarding Partial R_{Max} rest-particles must be developed.

The effect of conductivity on the distribution of electric fields in dielectric cylinders was examined in Section 3.5. A mechanism for simulating the conductive properties of dielectric media has not yet been developed for HPP-LGA, and consequently it was found that for large values of σ, HPP-LGA was unable to produce accurate predictions.

The cylinder with $\epsilon_r = 21$ and $\sigma = 1.275$ was chosen such that the loss across it would be similar to a cylinder with the dielectric properties of the liver, as described in Table 4.1. The study of the field distribution of that particular dielectric cylinder highlights the importance of including the conductive properties of dielectric media.

Chapter 5

Conclusion

A Lattice-Gas Automaton (LGA) is an unconditionally stable discrete system in which particles with a small and finite number of states move about on a regular lattice. The dynamics of this system are governed by a reversible and deterministic rule which is applied to the entire system simultaneously. In this thesis the development of new models for the application of HPP-LGA to two-dimensional electromagnetic wave phenomena has been presented.

5.1 Major Results

1. The relationship between microscopic particle dynamics, fluid flow and two-dimensional electromagnetics was introduced and developed. The standard HPP-LGA model was presented with predictions of equilibria and propagation velocity verified by extensive simulations.

2. An alternative to the Adnani rest-particle model [7] was presented, which permitted the modelling of higher ϵ_r values in a more efficient manner. The neces-

sary modifications to the standard HPP-LGA model in order to model different propagation speeds was documented and verified.

3. The concept of rest-particle mixtures for the modelling of a continuous range of propagation speeds was also introduced and verified.

4. The implementation details of an HPP-LGA absorbing boundary condition (ABC) were presented and the ABC was numerically evaluated. It was found that while effective for normally incident waves, the basic and graded ABC appeared to perform poorly for other angles of incidence.

5.2 Applications of HPP-LGA

Validation of the performance of the HPP-LGA rest-particle model was accomplished through the study of the normal incidence of a Gaussian pulsed plane wave at a plane dielectric boundary, resulting in errors of less that 10% for all predictions. A HPP-LGA cell to TLM cell discretization ratio of 10:1 [19] was used for the study of the normal incidence of a Gaussian pulsed plane wave on a thin dielectric boundary, with the conclusion that the ratio was not sufficiently large. The minimization of stair-stepping errors associated with the modelling of circular dielectric regions resulted in reasonable agreement between HPP-LGA and TLM predictions of scattered electric fields from cylindrical objects. In spite of the low number of samples taken in the time-domain, the HPP-LGA predicted electric field distribution inside a dielectric cylinder agreed satisfactorily with a TLM prediction.

The high spatial resolution of HPP-LGA was used in the application of HPP-LGA to the modelling and simulation of electromagnetic wave interaction with biological media. Although the predicted results appear to have been corrupted by scattered

fields. they still demonstrate the applicability of HPP-LGA to this class of difficult problems.

5.3 Future Work

1. The theory regarding Partial R_{Max} rest-particles should be fully developed in order to provide more options for the modelling of propagation velocities through the mixing of rest-particle models. With the use of Partial R_{Max} rest-particles. the efficiency in the use of bits. and the overall number of available propagation velocities is increased. as was shown in Section 2.2.2.

2. Depending on the propagation velocity which is desired. there are a number of different ways in which it can be achieved through the mixing of rest-particle models. For large regions. the relative composition of the dielectric region is of low importance since the different mixtures will all perform equally with regards to the desired dynamics. As the size of the region decreases. the ratio of the respective rest-particles becomes of greater importance. It is therefore necessary that the various combinations of rest-particles be examined to find the most effective mixture for small regions.

3. More studies into discretization ratios for HPP-LGA to other methods should be conducted in order to take advantage of the work done in those fields. The 10:1 HPP-LGA to TLM ratio used in this thesis has provided poor results for thin dielectric regions. Further examination of the effects of sampling window sizes and time averaging are also recommended.

4. Prediction of electromagnetic fields without the ability to account for material conductivity values renders the HPP-LGA method ineffective in the application to problems dealing with lossy media. It is strongly recommended that a method

for simulating conductivity values be developed. with the harnessing of the viscosity inherent in the HPP-LGA method a strong candidate as introduced in [32].

5. The utility of a proper working absorbing boundary condition cannot be overstated. Without the ability to simulate a ABC which absorbs incident waves with a full range of angles. simulations will have to be performed in extremely large lattices. It is highly recommended that investigation into a more accurate ABC be conducted for the termination of the lattice in regions with or without rest-particles.

6. The HPP-LGA model as presented in this thesis needs to be altered for the application to computational electromagnetics with three-dimensional vector wave behaviour. This has already been accomplished with a TLM-style HPP-LGA implementation requiring 12 bits per HPP-LGA cell [33]. and a FDTD-style implementation requiring 24 bits per cell [34]. However. the high resolution of HPP-LGA models in two dimensions is a strength which becomes a liability when the model is extended to three dimensions. The amount of memory needed to simulate a problem with the single-bit HPP-LGA model increases by exponentially with the dimension of the problem [35]. It is therefore necessary to reduce the number of bits used so that problems can be simulated with a reasonable amount of resources.

7. When large sections of the lattice are being analyzed. as in field distribution predictions. the HPP-LGA method creates an incredible amount of data. Predictions will become increasingly accurate as the number of samples is increased. with the downside that the amount of data being produced quickly becomes difficult to manage. The processing of data as it is created would decrease the storage load placed on auxiliary memory. It is therefore recommended that the

real-time processing of HPP-LGA data be examined.

Appendix A

Binary Collision Operators

In order to derive the equilibrium particle concentrations for a lattice-gas, it must obey semi-detailed balance [7]. If we represent the transition from state s to state s' by a Boolean transition matrix A, a lattice-gas will obey semi-detailed balance if its transition matrix satisfies:

$$\sum_{s} A(s \rightarrow s') = 1 \tag{A.1}$$

The semi-detailed balance condition ensures that every output configuration is equally likely to occur. The more general condition of detailed balance as expressed in Equation A.2, ensures that forward and backward transitions occur with equal probability.

$$A(s \rightarrow s') = A(s' \rightarrow s) \tag{A.2}$$

Criteria A.1 should not be confused with the conservation of probability, expressed in Equation A.3.

$$\sum_{s'} A(s \rightarrow s') = 1 \tag{A.3}$$

For an n-bit HPP-LGA model, the microscopic collision details can be specified by a 2^n by 2^n Boolean transition matrix. Figure 2.8 shows all 16 possible configurations for a 4-bit HPP-LGA cell. Each input configuration leads to exactly one output configuration, which is denoted by a 1. Except for the HPP-LGA collision, all input configurations lead to themselves as output configurations.

The dynamics of a HPP-LGA can also be completely described by a set of boolean equations known as Binary Collision Operators (BCOs). BCOs can be viewed as a algebraic representation of the Boolean transition matrix. If $b_i(\mathbf{x}, t)$ represents the presence or absence of a particle (denoted by a 1 or a 0), then the presence of a particle in an adjacent cell at the next time step can be expressed as:

$$b_i(\mathbf{x} + \mathbf{c}^i, t + \Delta t) = b_i(\mathbf{x}, t) + C_i[\mathbf{b}(\mathbf{x}, t)] \qquad i = 1, 2, 3, 4 \tag{A.4}$$

where $b_i(\mathbf{x}, t)$ represents the presence or absence of a particle propagating in one of the four directions, represented by velocity state i, in cell $\mathbf{x}$ at time t. $C_i[\mathbf{b}(\mathbf{x}, t)]$ is the microscopic collision operator for direction i, which examines the cell for HPP-LGA collisions. Its input is $\mathbf{b}(\mathbf{x}, t)$, which is a vector of all the particles in cell $\mathbf{x}$ at time t. With this information it is possible to determine $b_i(\mathbf{x} + \mathbf{c}^i, t + \Delta t)$ which is the presence or absence of a particle propagating in direction i, in cell $\mathbf{x} + \mathbf{c}^i$ at the next time-step $(t + \Delta t)$. The following sections present the BCOs for HPP-LGA rules involving 0, 1, 2, 3 and 7 rest-particles.

A.1 Equations for 0 Rest Particles

$$b_N(t + \Delta t) = b_N + C_N$$

$$= b_N + \overline{b_N b_S} b_E b_{W\cdot} - b_N b_S \overline{b_E b_{W\cdot}} \quad (A.5)$$

$$b_S(t+\Delta t) = b_S + C_S$$

$$= b_S + \overline{b_N b_S} b_E b_{W\cdot} - b_N b_S \overline{b_E b_{W\cdot}} \quad (A.6)$$

$$b_E(t+\Delta t) = b_E + C_E$$

$$= b_E + b_N b_S \overline{b_E b_{W\cdot}} - \overline{b_N b_S} b_E b_{W\cdot} \quad (A.7)$$

$$b_{W\cdot}(t+\Delta t) = b_{W\cdot} + C_{W\cdot}$$

$$= b_{W\cdot} + b_N b_S \overline{b_E b_{W\cdot}} - \overline{b_N b_S} b_E b_{W\cdot} \quad (A.8)$$

$$C_E + C_N + C_{W\cdot} + C_S = 0$$

$$C_E - C_{W\cdot} = 0$$

$$C_N - C_S = 0 \quad (A.9)$$

A.2 Equations for 1 Rest Particle

$$b_N(t+\Delta t) = b_N + C_N$$

$$= b_N + \overline{b_N b_S} b_E b_{W\cdot} - b_N b_S \overline{b_E b_{W\cdot}}$$

$$+ \overline{b_N b_S b_E b_{W\cdot}} b_R + b_N b_S b_E b_{W\cdot} \overline{b_R} \quad (A.10)$$

$$b_S(t+\Delta t) = b_S + C_S$$

$$= b_S + \overline{b_N b_S} b_E b_{W\cdot} - b_N b_S \overline{b_E b_{W\cdot}}$$

$$+ \overline{b_N b_S b_E b_{W\cdot}} b_R + b_N b_S b_E b_{W\cdot} \overline{b_R} \quad (A.11)$$

$$b_E(t+\Delta t) = b_E + C_E$$

$$= b_E + b_N b_S \overline{b_E b_{W\cdot}} - \overline{b_N b_S} b_E b_{W\cdot}$$

$$+ \overline{b_N b_S b_E b_{W\cdot}} b_R + b_N b_S b_E b_{W\cdot} \overline{b_R} \quad (A.12)$$

$$
\begin{aligned}
b_{W\cdot}(t+\Delta t) &= b_{W\cdot} + C_{W\cdot} \\
&= b_{W\cdot} + b_N b_S \overline{b_E b_{W\cdot}} - \overline{b_N b_S} b_E b_{W\cdot} \\
&\quad + \overline{b_N b_S b_E b_{W\cdot}} b_R + b_N b_S b_E b_{W\cdot} \overline{b_R} \qquad \text{(A.13)} \\
b_R(t+\Delta t) &= b_R + C_R \\
&= b_R + b_N b_S b_E b_{W\cdot} \overline{b_R} - \overline{b_N b_S b_E b_{W\cdot}} b_R \qquad \text{(A.14)}
\end{aligned}
$$

$$
\begin{aligned}
C_E + C_N + C_{W\cdot} + C_S + 4C_R = 0 \\
C_E - C_{W\cdot} = 0 \\
C_N - C_S = 0 \qquad \text{(A.15)}
\end{aligned}
$$

A.3 Equations for 2 Rest Particles

$$
\begin{aligned}
b_N(t+\Delta t) &= b_N + C_N \\
&= b_N + \overline{b_N b_S} b_E b_{W\cdot} - b_N b_S \overline{b_E b_{W\cdot}} \\
&\quad + \overline{b_N b_S b_E b_{W\cdot} b_{R_1}} b_{R_2} \\
&\quad + \overline{b_N b_S b_E b_{W\cdot}} b_{R_1} \overline{b_{R_2}} \\
&\quad - b_N b_S b_E b_{W\cdot} \overline{b_{R_1} b_{R_2}} \\
&\quad - b_N b_S b_E b_{W\cdot} b_{R_1} \overline{b_{R_2}} \qquad \text{(A.16)} \\
b_S(t+\Delta t) &= b_S + C_S \\
&= b_S + \overline{b_N b_S} b_E b_{W\cdot} - b_N b_S \overline{b_E b_{W\cdot}} \\
&\quad + \overline{b_N b_S b_E b_{W\cdot} b_{R_1}} b_{R_2} \\
&\quad + \overline{b_N b_S b_E b_{W\cdot}} b_{R_1} \overline{b_{R_2}} \\
&\quad - b_N b_S b_E b_{W\cdot} \overline{b_{R_1} b_{R_2}}
\end{aligned}
$$

$$- b_N b_S b_E b_W b_{R_1} \overline{b_{R_2}} \tag{A.17}$$

$$\begin{aligned} b_E(t+\Delta t) &= b_E + C_E \\ &= b_E + b_N b_S \overline{b_E b_W} - \overline{b_N b_S} b_E b_W \\ &\quad + \overline{b_N b_S b_E b_W b_{R_1}} b_{R_2} \\ &\quad + \overline{b_N b_S b_E b_W} b_{R_1} \overline{b_{R_2}} \\ &\quad - b_N b_S b_E b_W \overline{b_{R_1} b_{R_2}} \\ &\quad - b_N b_S b_E b_W b_{R_1} \overline{b_{R_2}} \end{aligned} \tag{A.18}$$

$$\begin{aligned} b_W(t+\Delta t) &= b_W + C_W \\ &= b_W + b_N b_S \overline{b_E b_W} - \overline{b_N b_S} b_E b_W \\ &\quad + \overline{b_N b_S b_E b_W b_{R_1}} b_{R_2} \\ &\quad + \overline{b_N b_S b_E b_W} b_{R_1} \overline{b_{R_2}} \\ &\quad - b_N b_S b_E b_W \overline{b_{R_1} b_{R_2}} \\ &\quad - b_N b_S b_E b_W b_{R_1} \overline{b_{R_2}} \end{aligned} \tag{A.19}$$

$$\begin{aligned} b_{R_1}(t+\Delta t) &= b_{R_1} + C_{R_1} \\ &= b_{R_1} + b_N b_S b_E b_W \overline{b_{R_1} b_{R_2}} \\ &\quad + \overline{b_N b_S b_E b_W b_{R_1}} b_{R_2} \\ &\quad - \overline{b_N b_S b_E b_W} b_{R_1} \overline{b_{R_2}} \\ &\quad - b_N b_S b_E b_W b_{R_1} \overline{b_{R_2}} \end{aligned} \tag{A.20}$$

$$\begin{aligned} b_{R_2}(t+\Delta t) &= b_{R_2} + C_{R_2} \\ &= b_{R_2} + b_N b_S b_E b_W b_{R_1} \overline{b_{R_2}} \\ &\quad + \overline{b_N b_S b_E b_W b_{R_1}} b_{R_2} \end{aligned} \tag{A.21}$$

$$C_E + C_N + C_W + C_S + 4C_{R_1} + 8C_{R_2} = 0$$

$$C_E - C_W = 0$$
$$C_N - C_S = 0 \tag{A.22}$$

A.4 Equations for 3 Rest Particles

$$\begin{aligned}
b_N(t+\Delta t) &= b_N + C_N \\
&= b_N + \overline{b_N b_S} b_E b_W - b_N b_S \overline{b_E b_W} \\
&\quad + \overline{b_N b_S b_E b_W} b_{R_1} b_{R_2} \\
&\quad + \overline{b_N b_S b_E b_W} b_{R_1} \overline{b_{R_2}} \\
&\quad + \overline{b_N b_S b_E b_W} b_{R_1} b_{R_2} \\
&\quad - b_N b_S b_E b_W \overline{b_{R_1} b_{R_2}} \\
&\quad - b_N b_S b_E b_W b_{R_1} \overline{b_{R_2}} \\
&\quad - b_N b_S b_E b_W \overline{b_{R_1}} b_{R_2} \qquad \text{(A.23)} \\
b_S(t+\Delta t) &= b_S + C_S \\
&= b_S + \overline{b_N b_S} b_E b_W - b_N b_S \overline{b_E b_W} \\
&\quad + \overline{b_N b_S b_E b_W} b_{R_1} b_{R_2} \\
&\quad + \overline{b_N b_S b_E b_W} b_{R_1} \overline{b_{R_2}} \\
&\quad + \overline{b_N b_S b_E b_W} b_{R_1} b_{R_2} \\
&\quad - b_N b_S b_E b_W \overline{b_{R_1} b_{R_2}} \\
&\quad - b_N b_S b_E b_W b_{R_1} \overline{b_{R_2}} \\
&\quad - b_N b_S b_E b_W \overline{b_{R_1}} b_{R_2} \qquad \text{(A.24)} \\
b_E(t+\Delta t) &= b_E + C_E \\
&= b_E + b_N b_S \overline{b_E b_W} - \overline{b_N b_S} b_E b_W \\
&\quad + \overline{b_N b_S b_E b_W} b_{R_1} b_{R_2}
\end{aligned}$$

$$
\begin{aligned}
&+ \overline{b_N b_S b_E b_W} \cdot b_{R_1} \overline{b_{R_2}} \\
&+ \overline{b_N b_S b_E b_W} \cdot b_{R_1} b_{R_2} \\
&- b_N b_S b_E b_W \cdot \overline{b_{R_1} b_{R_2}} \\
&- b_N b_S b_E b_W \cdot b_{R_1} \overline{b_{R_2}} \\
&- b_N b_S b_E b_W \cdot \overline{b_{R_1}} b_{R_2} \qquad \text{(A.25)}
\end{aligned}
$$

$$
\begin{aligned}
b_W(t+\Delta t) &= b_W - C_W \\
&= b_W + b_N b_S \overline{b_E b_W} - \overline{b_N b_S} b_E b_W \\
&\quad + \overline{b_N b_S b_E b_W} \cdot b_{R_1} b_{R_2} \\
&\quad + \overline{b_N b_S b_E b_W} \cdot b_{R_1} \overline{b_{R_2}} \\
&\quad + \overline{b_N b_S b_E b_W} \cdot b_{R_1} b_{R_2} \\
&\quad - b_N b_S b_E b_W \cdot \overline{b_{R_1} b_{R_2}} \\
&\quad - b_N b_S b_E b_W \cdot b_{R_1} \overline{b_{R_2}} \\
&\quad - b_N b_S b_E b_W \cdot \overline{b_{R_1}} b_{R_2} \qquad \text{(A.26)}
\end{aligned}
$$

$$
\begin{aligned}
b_{R_1}(t+\Delta t) &= b_{R_1} + C_{R_1} \\
&= b_{R_1} + b_N b_S b_E b_W \cdot \overline{b_{R_1} b_{R_2}} \\
&\quad + \overline{b_N b_S b_E b_W} \cdot b_{R_1} b_{R_2} \\
&\quad + b_N b_S b_E b_W \cdot \overline{b_{R_1}} b_{R_2} \\
&\quad - \overline{b_N b_S b_E b_W} \cdot b_{R_1} \overline{b_{R_2}} \\
&\quad - b_N b_S b_E b_W \cdot b_{R_1} \overline{b_{R_2}} \\
&\quad - \overline{b_N b_S b_E b_W} \cdot b_{R_1} b_{R_2} \qquad \text{(A.27)}
\end{aligned}
$$

$$
\begin{aligned}
b_{R_2}(t+\Delta t) &= b_{R_2} + C_{R_2} \\
&= b_{R_2} + b_N b_S b_E b_W \cdot b_{R_1} \overline{b_{R_2}} \\
&\quad + \overline{b_N b_S b_E b_W} \cdot b_{R_1} b_{R_2} \qquad \text{(A.28)}
\end{aligned}
$$

$$
\begin{aligned}
C_E + C_N + C_W + C_S + 4C_{R_1} + 8C_{R_2} &= 0 \\
C_E - C_W &= 0 \\
C_N - C_S &= 0
\end{aligned}
\tag{A.29}
$$

A.5 Equations for 7 Rest Particles

$$
\begin{aligned}
b_N(t+\Delta t) &= b_N + C_N \\
&= b_N + \overline{b_N b_S} b_E b_W - b_N b_S \overline{b_E b_W} \\
&\quad + \overline{b_N b_S b_E b_W} b_{R_1} \overline{b_{R_2} b_{R_3}} \\
&\quad + \overline{b_N b_S b_E b_W} b_{R_1} b_{R_2} \overline{b_{R_3}} \\
&\quad + \overline{b_N b_S b_E b_W} b_{R_1} b_{R_2} \overline{b_{R_3}} \\
&\quad + \overline{b_N b_S b_E b_W} \overline{b_{R_1} b_{R_2}} b_{R_3} \\
&\quad + \overline{b_N b_S b_E b_W} b_{R_1} \overline{b_{R_2}} b_{R_3} \\
&\quad + \overline{b_N b_S b_E b_W} b_{R_1} b_{R_2} b_{R_3} \\
&\quad + \overline{b_N b_S b_E b_W} b_{R_1} b_{R_2} b_{R_3} \\
&\quad - b_N b_S b_E b_W \overline{b_{R_1} b_{R_2} b_{R_3}} \\
&\quad - b_N b_S b_E b_W b_{R_1} \overline{b_{R_2} b_{R_3}} \\
&\quad - b_N b_S b_E b_W \overline{b_{R_1}} b_{R_2} \overline{b_{R_3}} \\
&\quad - b_N b_S b_E b_W b_{R_1} b_{R_2} \overline{b_{R_3}} \\
&\quad - b_N b_S b_E b_W \overline{b_{R_1} b_{R_2}} b_{R_3} \\
&\quad - b_N b_S b_E b_W b_{R_1} \overline{b_{R_2}} b_{R_3} \\
&\quad - b_N b_S b_E b_W \overline{b_{R_1}} b_{R_2} b_{R_3} \\
b_S(t+\Delta t) &= b_S + C_S
\end{aligned}
\tag{A.30}
$$

$$
\begin{aligned}
&= b_S + \overline{b_N b_S} b_E b_W - b_N b_S \overline{b_E b_W} \\
&\quad + \overline{b_N b_S b_E b_W} b_{R_1} \overline{b_{R_2} b_{R_3}} \\
&\quad + \overline{b_N b_S b_E b_W} b_{R_1} b_{R_2} \overline{b_{R_3}} \\
&\quad + \overline{b_N b_S b_E b_W} b_{R_1} b_{R_2} \overline{b_{R_3}} \\
&\quad + \overline{b_N b_S b_E b_W} b_{R_1} b_{R_2} b_{R_3} \\
&\quad + \overline{b_N b_S b_E b_W} b_{R_1} \overline{b_{R_2}} b_{R_3} \\
&\quad + \overline{b_N b_S b_E b_W} \overline{b_{R_1}} b_{R_2} b_{R_3} \\
&\quad + \overline{b_N b_S b_E b_W} b_{R_1} b_{R_2} b_{R_3} \\
&\quad - b_N b_S b_E b_W \overline{b_{R_1} b_{R_2} b_{R_3}} \\
&\quad - b_N b_S b_E b_W b_{R_1} \overline{b_{R_2} b_{R_3}} \\
&\quad - b_N b_S b_E b_W \overline{b_{R_1}} b_{R_2} \overline{b_{R_3}} \\
&\quad - b_N b_S b_E b_W b_{R_1} b_{R_2} \overline{b_{R_3}} \\
&\quad - b_N b_S b_E b_W \overline{b_{R_1} b_{R_2}} b_{R_3} \\
&\quad - b_N b_S b_E b_W b_{R_1} \overline{b_{R_2}} b_{R_3} \\
&\quad - b_N b_S b_E b_W \overline{b_{R_1}} b_{R_2} b_{R_3} \qquad \text{(A.31)}
\end{aligned}
$$

$$
\begin{aligned}
b_E(t + \Delta t) &= b_E + C_E \\
&= b_E + b_N b_S \overline{b_E b_W} - \overline{b_N b_S} b_E b_W \\
&\quad + \overline{b_N b_S b_E b_W} b_{R_1} \overline{b_{R_2} b_{R_3}} \\
&\quad + \overline{b_N b_S b_E b_W} b_{R_1} b_{R_2} \overline{b_{R_3}} \\
&\quad + \overline{b_N b_S b_E b_W} b_{R_1} b_{R_2} \overline{b_{R_3}} \\
&\quad + \overline{b_N b_S b_E b_W} b_{R_1} b_{R_2} b_{R_3} \\
&\quad + \overline{b_N b_S b_E b_W} b_{R_1} \overline{b_{R_2}} b_{R_3} \\
&\quad + \overline{b_N b_S b_E b_W} \overline{b_{R_1}} b_{R_2} b_{R_3} \\
&\quad + \overline{b_N b_S b_E b_W} b_{R_1} b_{R_2} b_{R_3}
\end{aligned}
$$

$$
\begin{aligned}
&- b_N b_S b_E b_W \cdot \overline{b_{R_1} b_{R_2} b_{R_3}} \\
&- b_N b_S b_E b_W \cdot b_{R_1} \overline{b_{R_2} b_{R_3}} \\
&- b_N b_S b_E b_W \cdot \overline{b_{R_1}} b_{R_2} \overline{b_{R_3}} \\
&- b_N b_S b_E b_W \cdot b_{R_1} b_{R_2} \overline{b_{R_3}} \\
&- b_N b_S b_E b_W \cdot \overline{b_{R_1} b_{R_2}} b_{R_3} \\
&- b_N b_S b_E b_W \cdot b_{R_1} \overline{b_{R_2}} b_{R_3} \\
&- b_N b_S b_E b_W \cdot \overline{b_{R_1}} b_{R_2} b_{R_3} \qquad \text{(A.32)}
\end{aligned}
$$

$$
\begin{aligned}
b_W \cdot (t + \Delta t) &= b_W \cdot + C_W \cdot \\
&= b_W \cdot + b_N b_S \overline{b_E b_W} - \overline{b_N b_S} b_E b_W \cdot \\
&\quad + \overline{b_N b_S b_E b_W} \cdot b_{R_1} \overline{b_{R_2} b_{R_3}} \\
&\quad + \overline{b_N b_S b_E b_W} \cdot \overline{b_{R_1}} b_{R_2} \overline{b_{R_3}} \\
&\quad + \overline{b_N b_S b_E b_W} \cdot b_{R_1} b_{R_2} \overline{b_{R_3}} \\
&\quad + \overline{b_N b_S b_E b_W} \cdot \overline{b_{R_1} b_{R_2}} b_{R_3} \\
&\quad + \overline{b_N b_S b_E b_W} \cdot b_{R_1} \overline{b_{R_2}} b_{R_3} \\
&\quad + \overline{b_N b_S b_E b_W} \cdot \overline{b_{R_1}} b_{R_2} b_{R_3} \\
&\quad + \overline{b_N b_S b_E b_W} \cdot b_{R_1} b_{R_2} b_{R_3} \\
&\quad - b_N b_S b_E b_W \cdot \overline{b_{R_1} b_{R_2} b_{R_3}} \\
&\quad - b_N b_S b_E b_W \cdot b_{R_1} \overline{b_{R_2} b_{R_3}} \\
&\quad - b_N b_S b_E b_W \cdot \overline{b_{R_1}} b_{R_2} \overline{b_{R_3}} \\
&\quad - b_N b_S b_E b_W \cdot b_{R_1} b_{R_2} \overline{b_{R_3}} \\
&\quad - b_N b_S b_E b_W \cdot \overline{b_{R_1} b_{R_2}} b_{R_3} \\
&\quad - b_N b_S b_E b_W \cdot b_{R_1} \overline{b_{R_2}} b_{R_3} \\
&\quad - b_N b_S b_E b_W \cdot \overline{b_{R_1}} b_{R_2} b_{R_3} \qquad \text{(A.33)} \\
b_{R_1}(t + \Delta t) &= b_{R_1} + C_{R_1}
\end{aligned}
$$

$$
\begin{aligned}
&= b_{R_1} + b_N b_S b_E b_W \overline{b_{R_1} b_{R_2} b_{R_3}} \\
&\quad + b_N b_S b_E b_W \overline{b_{R_1}} b_{R_2} \overline{b_{R_3}} \\
&\quad + b_N b_S b_E b_W \overline{b_{R_1} b_{R_2}} b_{R_3} \\
&\quad + b_N b_S b_E b_W \overline{b_{R_1}} b_{R_2} b_{R_3} \\
&\quad + \overline{b_N b_S b_E b_W b_{R_1}} b_{R_2} \overline{b_{R_3}} \\
&\quad + \overline{b_N b_S b_E b_W b_{R_1} b_{R_2}} b_{R_3} \\
&\quad + \overline{b_N b_S b_E b_W b_{R_1}} b_{R_2} b_{R_3} \\
&\quad - \overline{b_N b_S b_E b_W} b_{R_1} \overline{b_{R_2} b_{R_3}} \\
&\quad - \overline{b_N b_S b_E b_W} b_{R_1} b_{R_2} \overline{b_{R_3}} \\
&\quad - \overline{b_N b_S b_E b_W} b_{R_1} \overline{b_{R_2}} b_{R_3} \\
&\quad - \overline{b_N b_S b_E b_W} b_{R_1} b_{R_2} b_{R_3} \\
&\quad - b_N b_S b_E b_W b_{R_1} \overline{b_{R_2} b_{R_3}} \\
&\quad - b_N b_S b_E b_W b_{R_1} b_{R_2} \overline{b_{R_3}} \\
&\quad - b_N b_S b_E b_W b_{R_1} \overline{b_{R_2}} b_{R_3} \qquad \text{(A.34)}
\end{aligned}
$$

$$
\begin{aligned}
b_{R_2}(t+\Delta t) &= b_{R_2} + C_{R_2} \\
&= b_{R_2} + b_N b_S b_E b_W b_{R_1} \overline{b_{R_2} b_{R_3}} \\
&\quad + b_N b_S b_E b_W b_{R_1} \overline{b_{R_2}} b_{R_3} \\
&\quad + \overline{b_N b_S b_E b_W b_{R_1} b_{R_2}} b_{R_3} \\
&\quad - \overline{b_N b_S b_E b_W b_{R_1}} b_{R_2} b_{R_3} \\
&\quad - \overline{b_N b_S b_E b_W b_{R_1}} b_{R_2} \overline{b_{R_3}} \\
&\quad - b_N b_S b_E b_W b_{R_1} b_{R_2} \overline{b_{R_3}} \qquad \text{(A.35)}
\end{aligned}
$$

$$
\begin{aligned}
b_{R_3}(t+\Delta t) &= b_{R_3} + C_{R_3} \\
&= b_{R_3} + b_N b_S b_E b_W b_{R_1} b_{R_2} \overline{b_{R_3}} \\
&\quad - \overline{b_N b_S b_E b_W b_{R_1} b_{R_2}} b_{R_3} \qquad \text{(A.36)}
\end{aligned}
$$

$$C_E + C_N + C_W + C_S + 4C_{R_1} + 8C_{R_2} + 16C_{R_3} = 0$$
$$C_E - C_W = 0$$
$$C_N - C_S = 0 \qquad (A.37)$$

Appendix B

CAM-8 16+ Bit Experiments and Look-Up Table Switching

It is often necessary to switch look-up tables (LUTs) and bits because the 16-bits which the fundamental CAM-8 cell is based on is not enough to represent all of the structures which are needed. This appendix will describe the methods used for implementing large experiments in the CAM-8. This process involves the assiging of subcells and switching between different LUTs. It is assumed that the reader is familiar with the basics of programming the CAM-8 using CAM-8 Forth [36].

There are three parts to creating 16+ bit experiments. First one needs to define different subcells of information which are to be switched in and out. Next, rules need to be defined which will operate on the different subcells. Finally, the data needs to be loaded in the correct fashion. The following example is taken directly from an *.exp* file which was used to run some of the cylinder experiments.

The data needs to be broken up into subcells, which can be of varying size. In the following example, thisis accomplished through two 8-bit subcells. The design process involves deciding how the data is going to be broken up, while making sure

that the data which needs to be there for decisions (such as boundary conditions, rest-particle markers) is there.

The bits in the subcells themselves are defined as would normally be defined for a regular 16-bit case, except that subcells are differentiated from each other by the header *0 subcell:* or *1 subcell:*.

```
0 subcell:

0 0 == north
1 1 == south
2 2 == east
3 3 == west

0 3 == particles

etc...

12 12 == count_north
13 13 == count_south
14 14 == count_east
15 15 == count_west

12 15 == moving_count

 0  7 == subcell_zero_low
 8 15 == subcell_zero_high

1 subcell:

 8  8 == source_marker
 9  9 == source_bits

10 10 == abc
11 11 == pmc

12 12 == random_north
13 13 == random_south
14 14 == random_east
```

```
15 15 == random_west

12 15 == random_numbers

 0  7 == subcell_one_low
 8 15 == subcell_one_high
```

The rules are defined in a normal manner, and reference wharever bits are to be used for them. The construction of the 16-bit space takes place in a different part of the experiment file, and in the initial loading of the data. One therefore has comments of the following type:

```
define-rule hpp-moving-rule
various rules according to CAM-8 FORTH...
end-rule

define-rule hpp-boundaries-rule
various rules according to CAM-8 FORTH...
end-rule

: clear-events  run no-scan new-count ;

define-step init-step
scan-format 25 ecl!
lut-data hpp-boundaries-rule switch-luts
clear-events
site-src lut rest_markers field site
event-src lut
lut-src site
display site
end-step
this is when-starting
```

It is important to have the correct rule in the line `lut-data hpp-boundaries-rule switch-` such that the subcell data combination which is active when the data is initially loaded will be the correct one.

The data and lut switching occurs in the definition of the hpp step as follows:

```
: hpp-step

\ *** Subcell 0 - Low  = active ***
\ *** Subcell 1 - High = active ***


lut-data hpp-boundaries-rule switch-luts

kick random_north   field  3 x 13 y
random_south   field     7 x  5 y
random_east    field     1 x 17 y
random_west    field 13 x  5 y
source_bits    field    -1 x  7 y
run

assemble-cell subcell_one_high field  remove
subcell_zero_high field add

\ *** Subcell 0 - Low  = active ***
\ *** Subcell 0 - High = active ***

lut-data hpp-moving-rule switch-luts

kick north  field   -1 y
south  field    1 y
east   field    1 x
west   field   -1 x
run new-count

run no-scan new-count

                #modules 0
        ?do
                select i module
                event read i countbuf
        loop

select all

assemble-cell subcell_zero_high field remove
```

```
subcell_one_high field add

\ *** Subcell 0 - Low  = active ***
\ *** Subcell 1 - High = active ***

step
```

The subcell construction process begins with data being loaded into the CAM-8. Data is split into files which correspond to the subcells as defined above. in this case `subcell_1.pat` and `subcell_2.pat`. Although the first 8-bits of *subcell 1* as defined above do not exist (they are not defined in the initial definition stage). it is necessary to define them so that the data from different subcells are not overwritten. The foundation of this process is the **assemble-cell** command. Using this command 8-bit subcells can be removed and added from the full 16-bit cell. The following section of code illustrates this concept.

```
: Initialize

[""] subcell_1.pat file>cam

assemble-cell  subcell_zero_low field remove
subcell_zero_high field remove
subcell_one_low  field add
subcell_one_high field add


[""] subcell_2.pat file>cam

\ ***  Subcell 1 - Low  = active  ***
\ ***  Subcell 1 - High = active  ***

assemble-cell subcell_one_low field  remove
subcell_zero_low field add

\ ***  Subcell 0 - Low  = active  ***
\ ***  Subcell 1 - High = active  ***
```

Appendix C

Dielectric Disk: $\epsilon_r = 5$

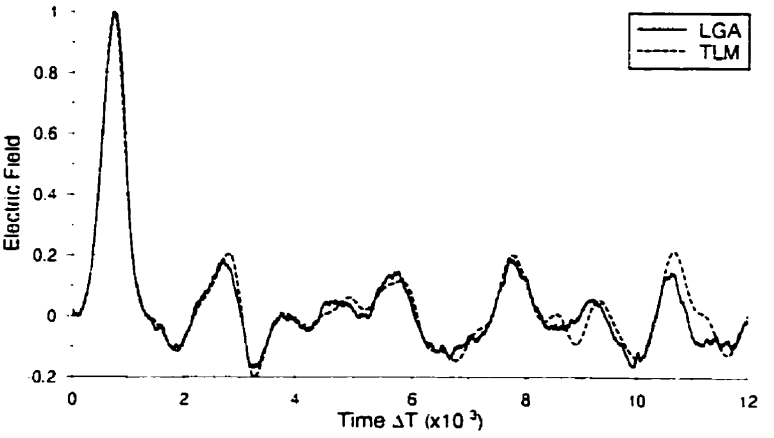

Figure C.1: Average time-domain plot of electric field to the left of an $\epsilon_r = 5$ dielectric disk

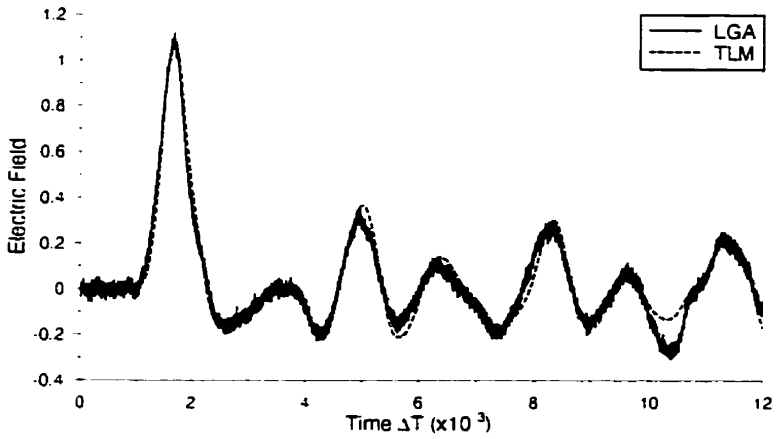

Figure C.2: Average time-domain plot of electric field inside an $\epsilon_r = 5$ dielectric disk

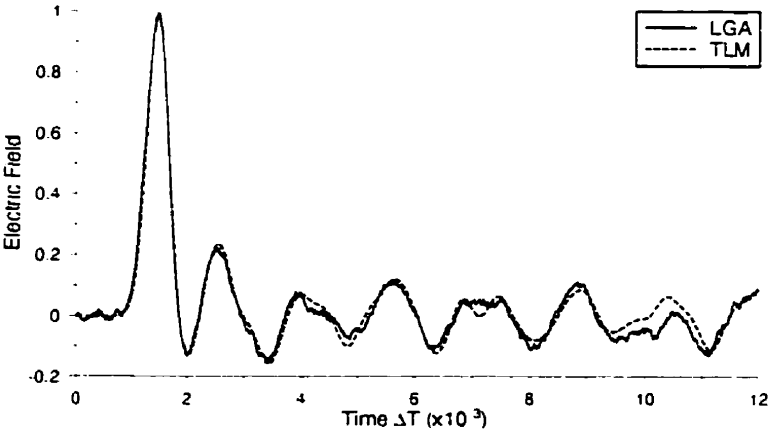

Figure C.3: Average time-domain plot of electric field above an $\epsilon_r = 5$ dielectric disk

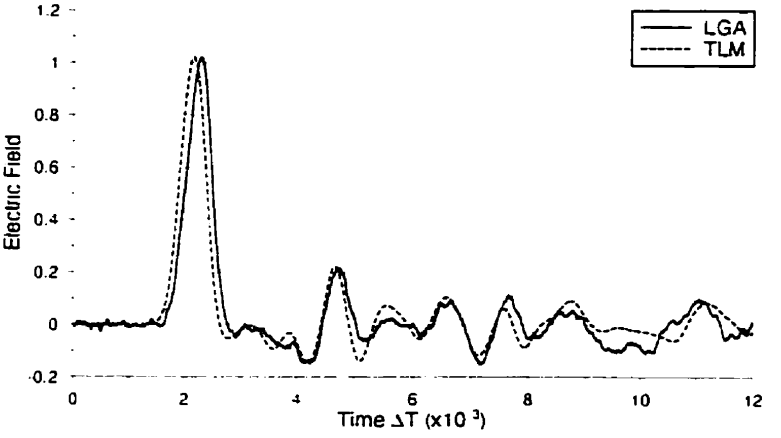

Figure C.4: Average time-domain plot of electric field to the right of an $\epsilon_r = 21$ dielectric disk

Appendix D

Dielectric Disk: $\epsilon_r = 21$

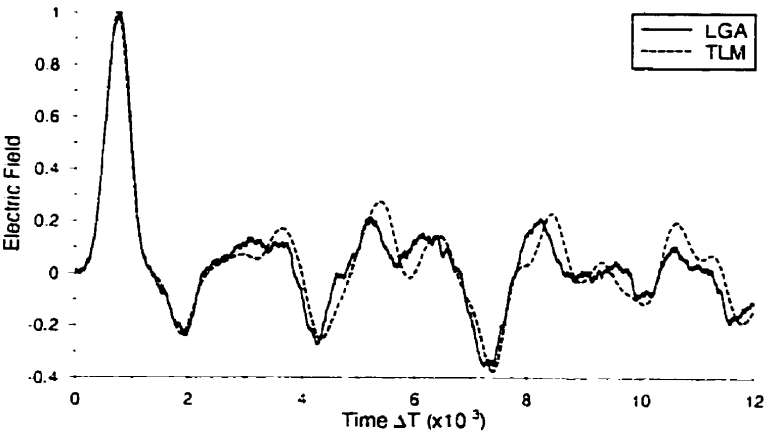

Figure D.1: Average time-domain plot of electric field to the left of an $\epsilon_r = 21$ dielectric disk

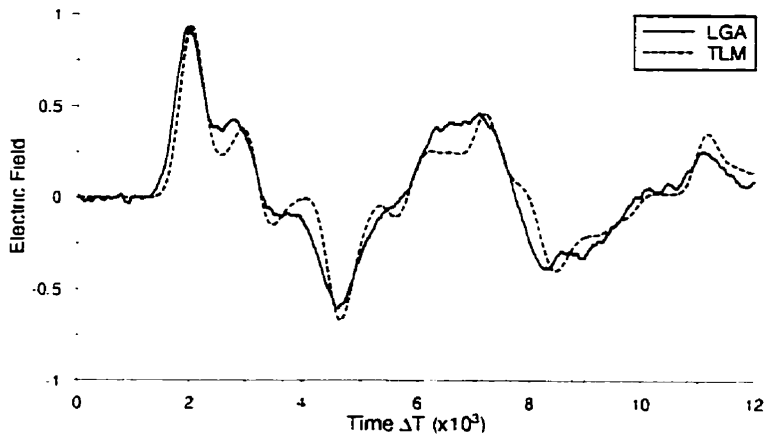

Figure D.2: Average time-domain plot of electric field inside an $\epsilon_r = 21$ dielectric disk

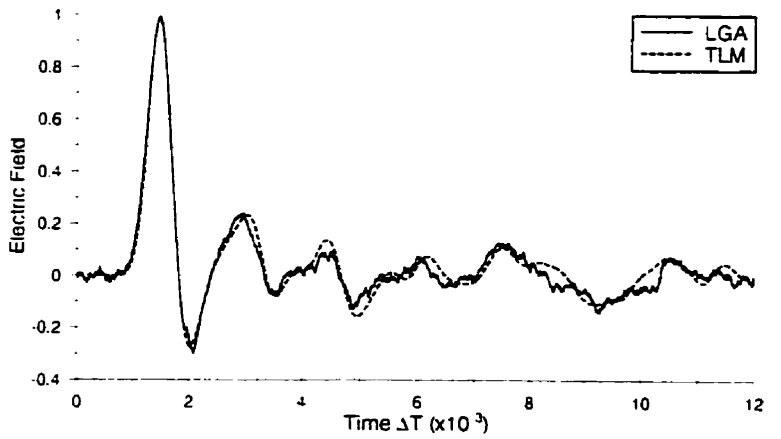

Figure D.3: Average time-domain plot of electric field above an $\epsilon_r = 21$ dielectric disk

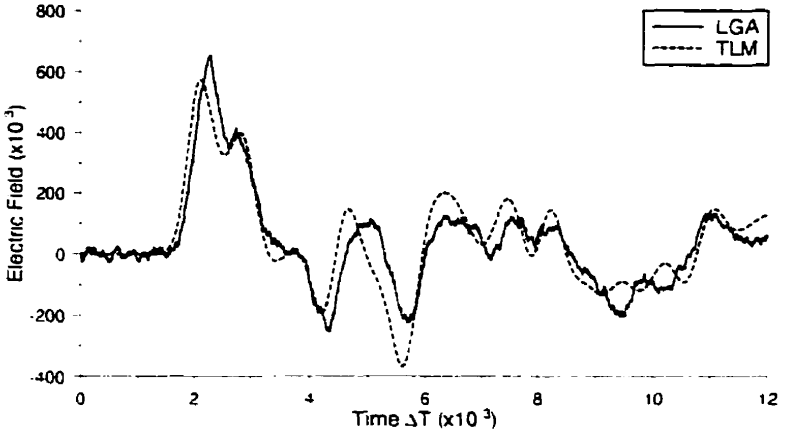

Figure D.4: Average time-domain plot of electric field to the right of an $\epsilon_r = 21$ dielectric disk

Appendix E

Dielectric Annulus: $\epsilon_r = 5$, $R_i = 50\% R_o$

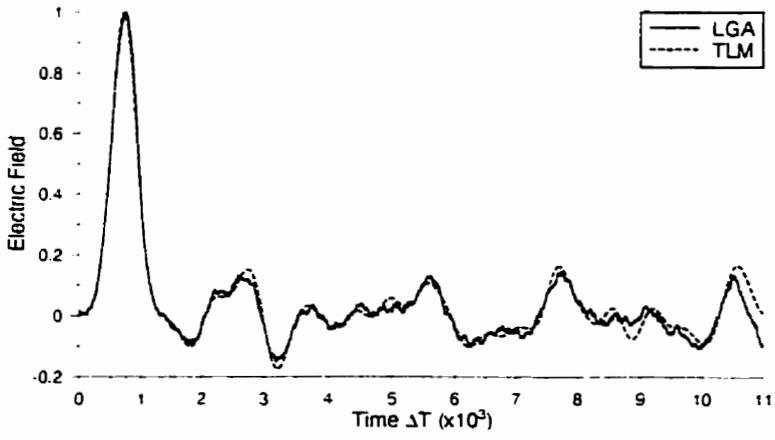

Figure E.1: Average time-domain plot of electric field to the left of an $\epsilon_r = 5$ dielectric annulus ($R_i = 50\% R_o$)

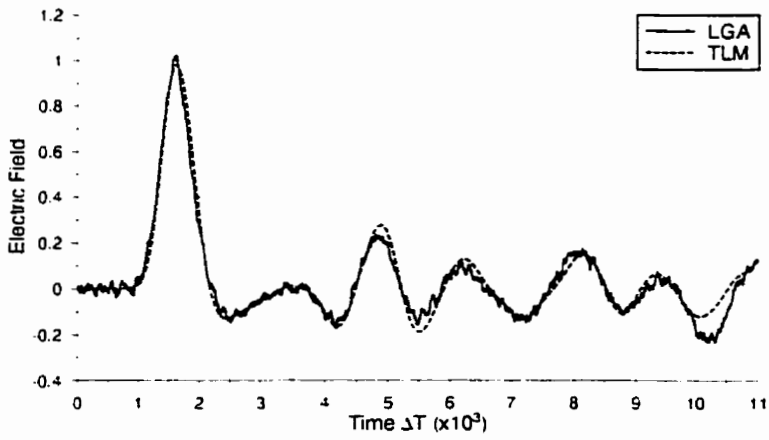

Figure E.2: Average time-domain plot of electric field inside an $\epsilon_r = 5$ dielectric annlus ($R_i = 50\% R_o$)

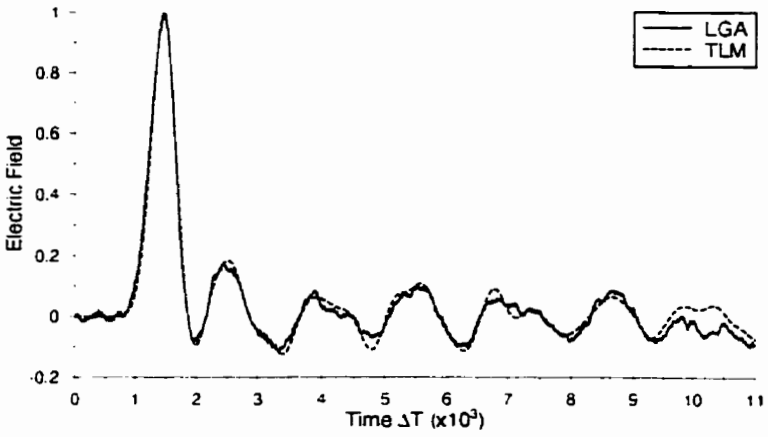

Figure E.3: Average time-domain plot of electric field above an $\epsilon_r = 5$ dielectric annlus ($R_i = 50\% R_o$)

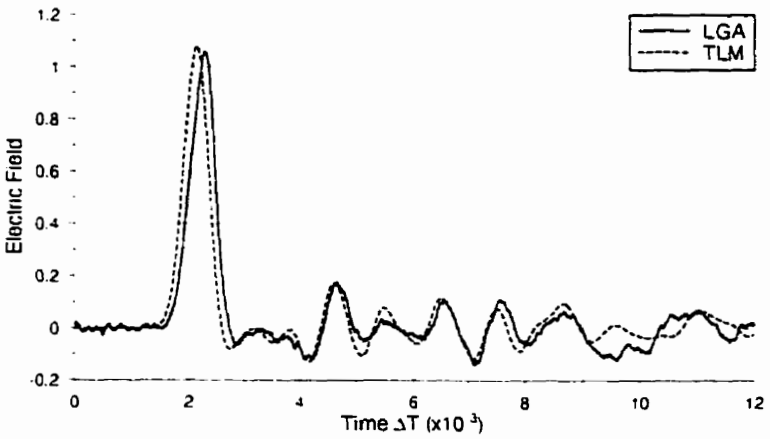

Figure E.4: Average time-domain plot of electric field to the left of an $\epsilon_r = 5$ dielectric annlus ($R_i = 50\% R_o$)

Appendix F

Dielectric Annulus: $\epsilon_r = 5$, $R_i = 80\% R_o$

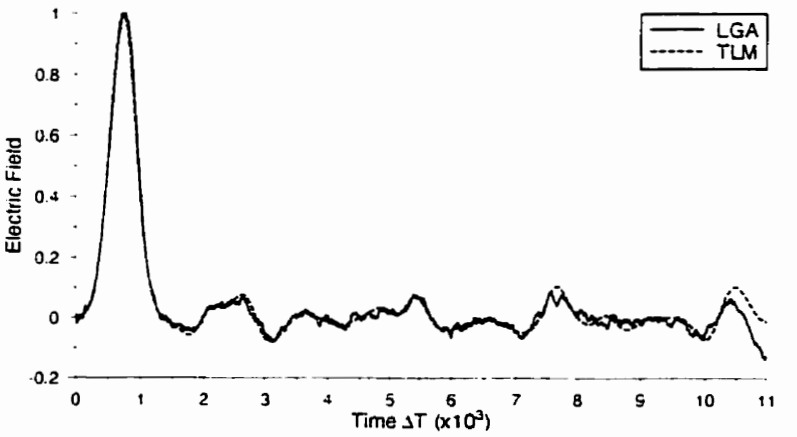

Figure F.1: Average time-domain plot of electric field to the left of an $\epsilon_r = 5$ dielectric annulus ($R_i = 80\% R_o$)

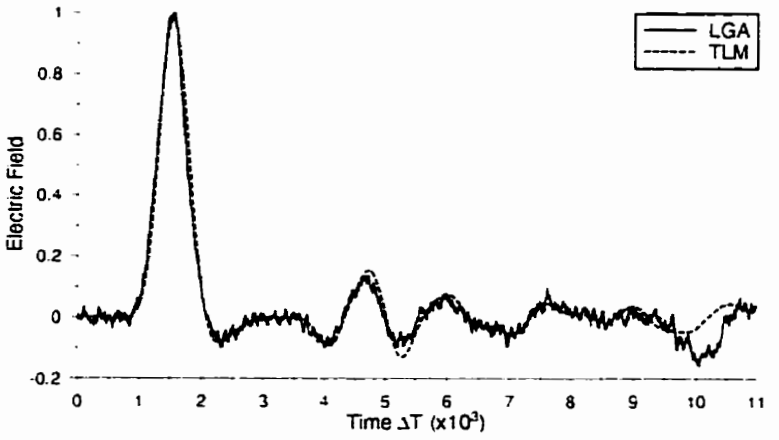

Figure F.2: Average time-domain plot of electric field inside an $\epsilon_r = 5$ dielectric annlus ($R_i = 80\% R_o$)

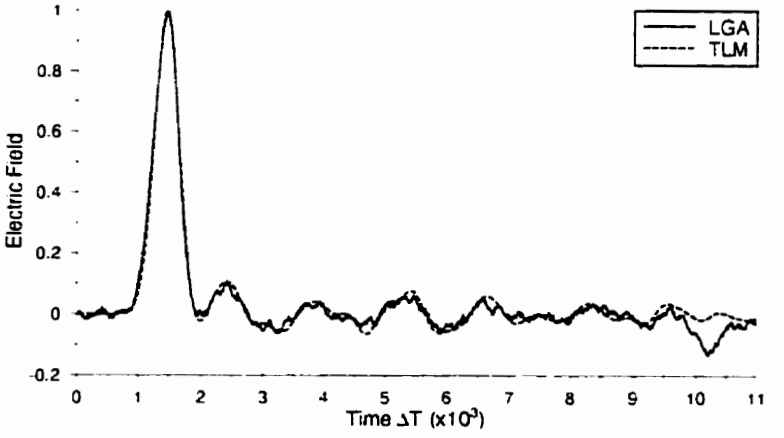

Figure F.3: Average time-domain plot of electric field above an $\epsilon_r = 5$ dielectric annlus ($R_i = 80\% R_o$)

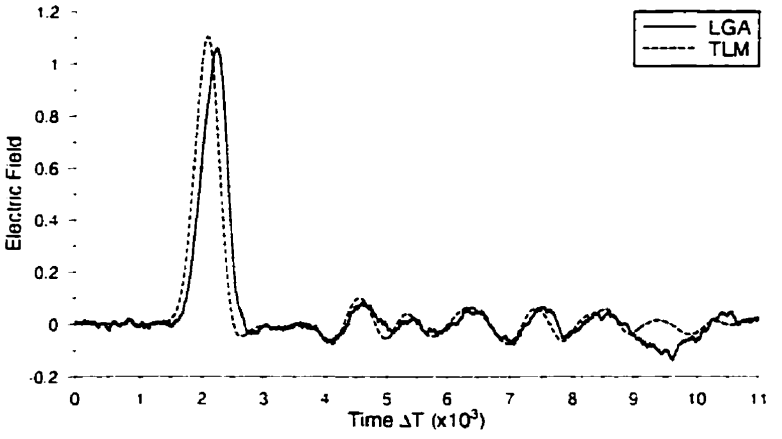

Figure F.4: Average time-domain plot of electric field to the right of an $\epsilon_r = 5$ dielectric annlus ($R_i = 80\% R_o$)

Appendix G

Dielectric Annulus: $\epsilon_r = 21$, $R_i = 50\% R_o$

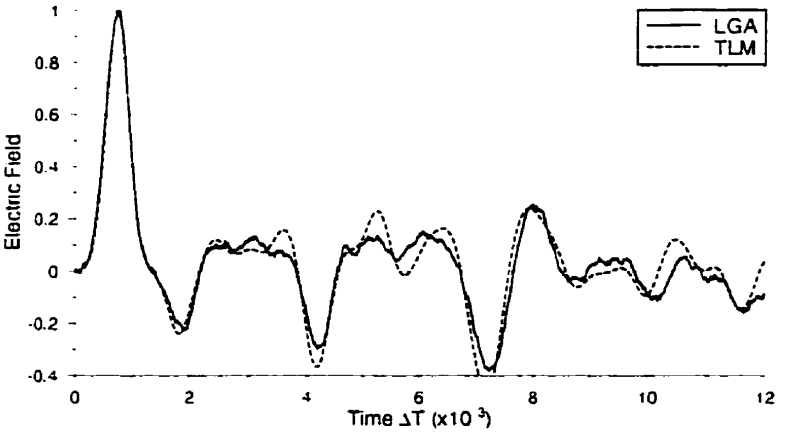

Figure G.1: Average time-domain plot of electric field to the left of an $\epsilon_r = 21$ dielectric annulus ($R_i = 50\% R_o$)

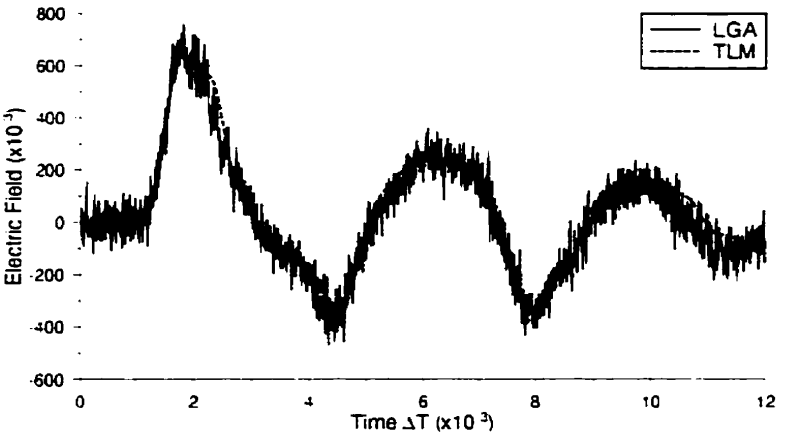

Figure G.2: Average time-domain plot of electric field inside an $\epsilon_r = 21$ dielectric annlus ($R_i = 50\% R_o$)

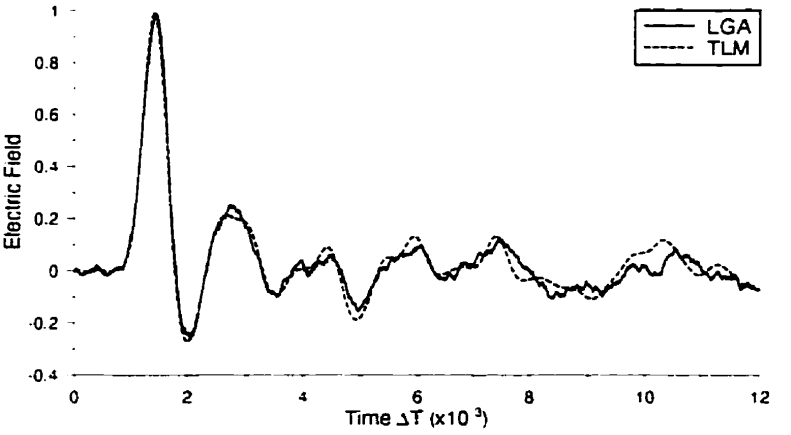

Figure G.3: Average time-domain plot of electric field above an $\epsilon_r = 21$ dielectric annlus ($R_i = 50\% R_o$)

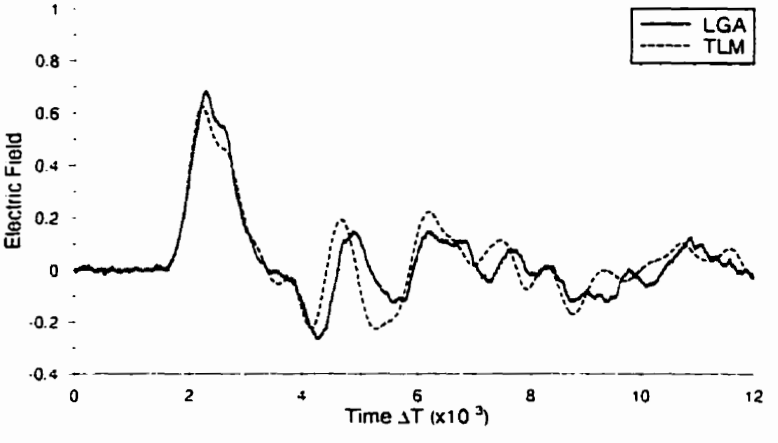

Figure G.4: Average time-domain plot of electric field to the right of an $\epsilon_r = 21$ dielectric annlus ($R_t = 50\% R_o$)

Appendix H

Dielectric Annulus: $\epsilon_r = 21$, $R_i = 80\% R_o$

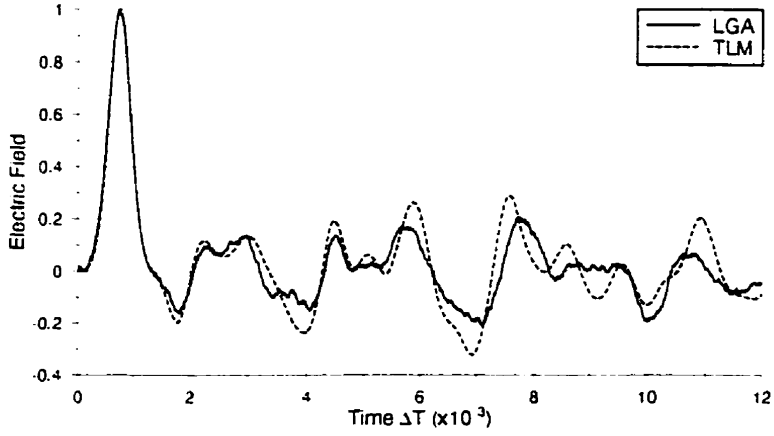

Figure H.1: Average time-domain plot of electric field to the left of an $\epsilon_r = 21$ dielectric annlus ($R_i = 80\% R_o$)

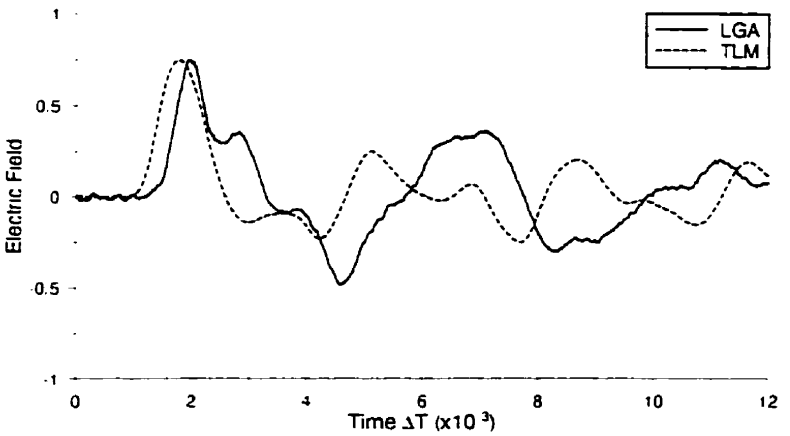

Figure H.2: Average time-domain plot of electric field inside an $\epsilon_r = 21$ dielectric annlus ($R_i = 80\% R_o$)

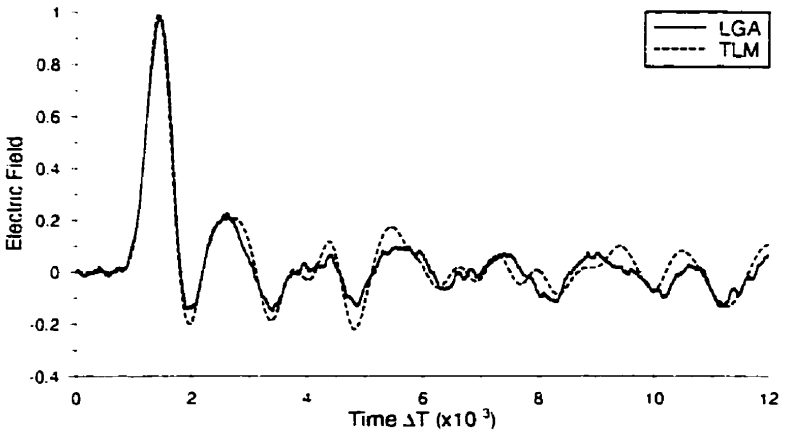

Figure H.3: Average time-domain plot of electric field above an $\epsilon_r = 21$ dielectric annlus ($R_i = 80\% R_o$)

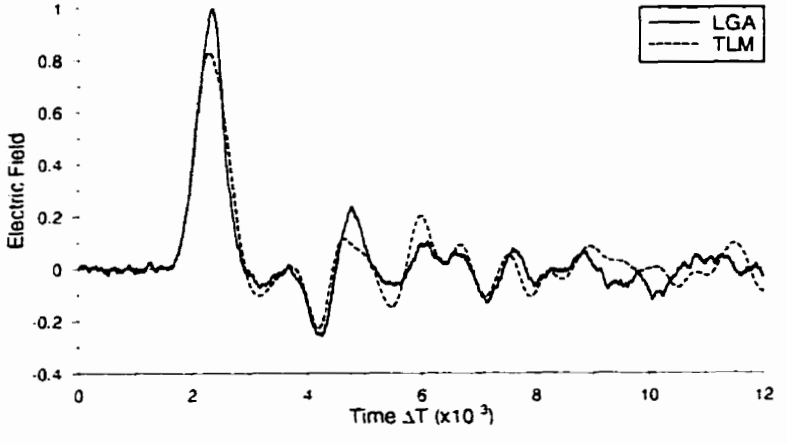

Figure H.4: Average time-domain plot of electric field to the right of an $\epsilon_r = 21$ dielectric annlus ($R_i = 80\% R_o$)

Appendix I

Dielectric Annulus: $\epsilon_r = 85$, $R_i = 50\% R_o$

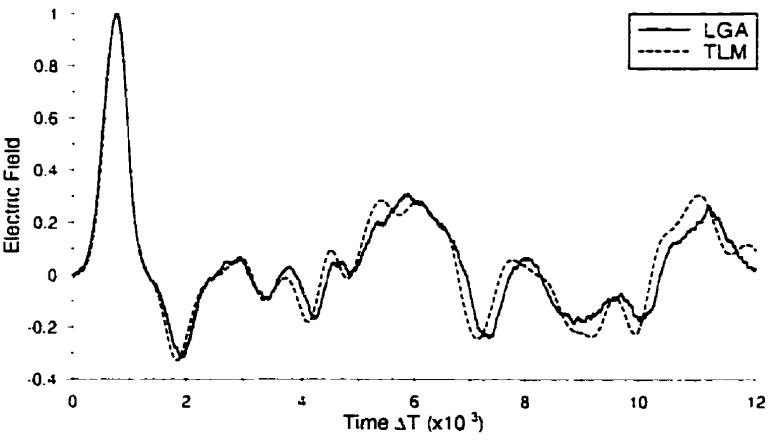

Figure I.1: Average time-domain plot of electric field to the right of an $\epsilon_r = 85$ dielectric annlus ($R_i = 50\% R_o$)

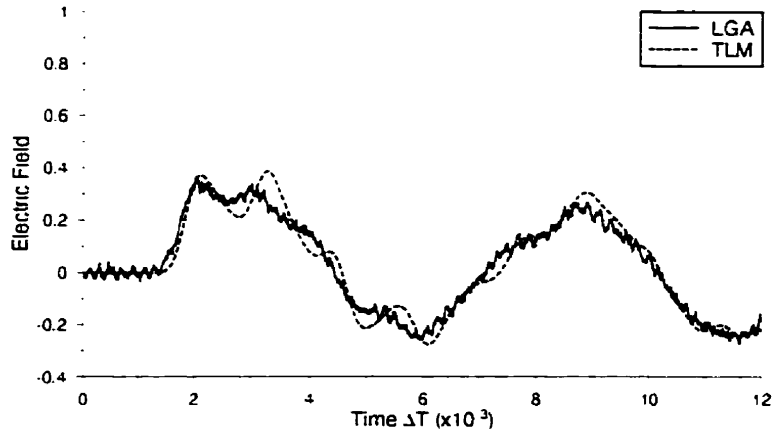

Figure I.2: Average time-domain plot of electric field inside an $\epsilon_r = 85$ dielectric annlus ($R_t = 50\% R_o$)

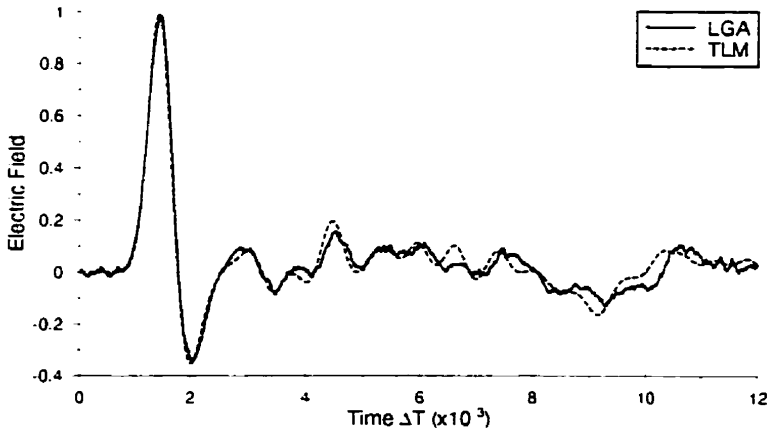

Figure I.3: Average time-domain plot of electric field above an $\epsilon_r = 85$ dielectric annlus ($R_t = 50\% R_o$)

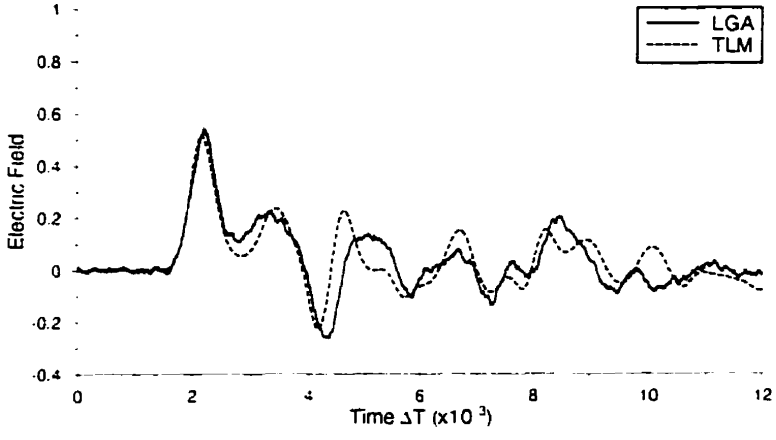

Figure I.4: Average time-domain plot of electric field to the left of an $\epsilon_r = 85$ dielectric annulus ($R_i = 50\% R_o$)

Appendix J

Dielectric Annulus: $\epsilon_r = 85$, $R_i = 80\% R_o$

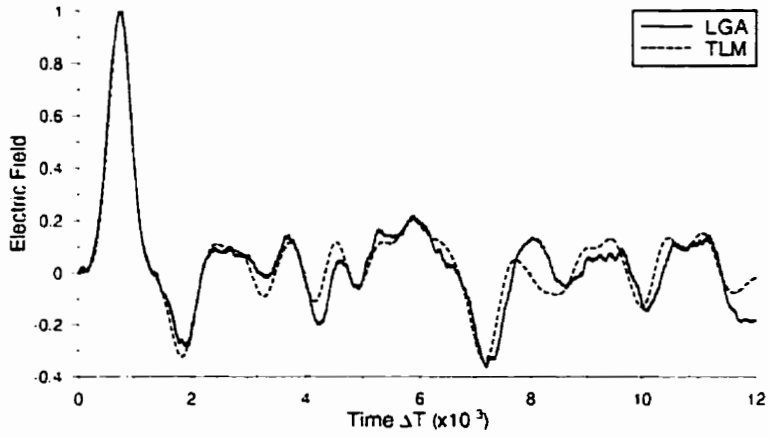

Figure J.1: Average time-domain plot of electric field to the left of an $\epsilon_r = 85$ dielectric annulus ($R_i = 80\% R_o$)

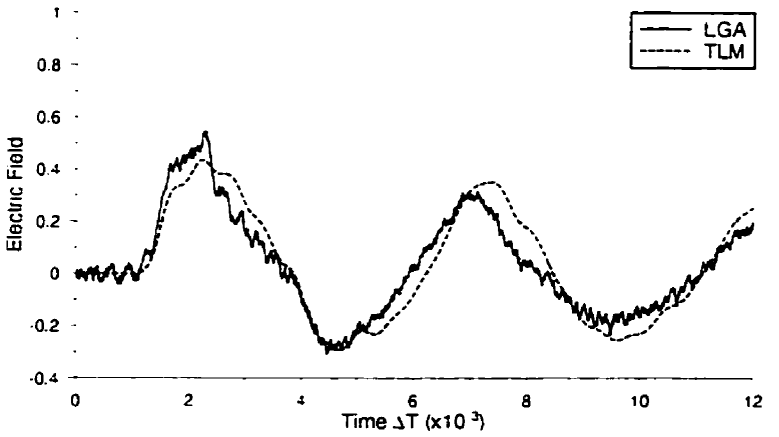

Figure J.2: Average time-domain plot of electric field inside an $\epsilon_r = 85$ dielectric annlus ($R_i = 80\% R_o$)

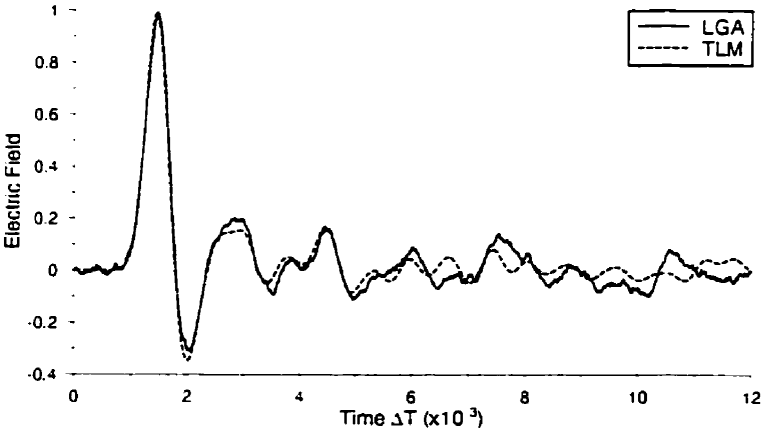

Figure J.3: Average time-domain plot of electric field above an $\epsilon_r = 85$ dielectric annlus ($R_i = 80\% R_o$)

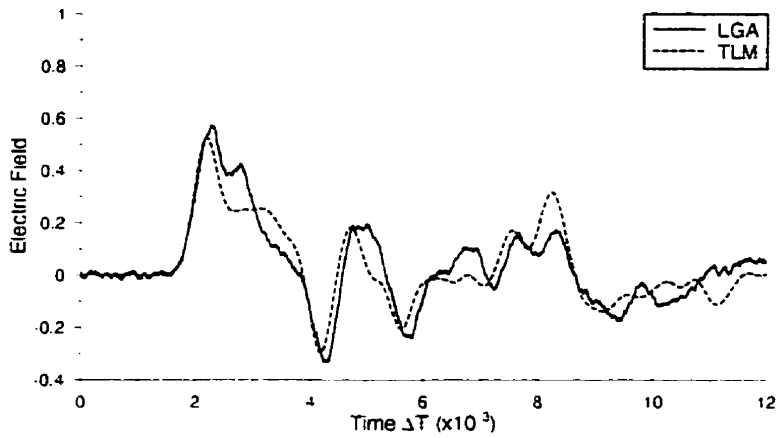

Figure J.4: Average time-domain plot of electric field to the right of an $\epsilon_r = 85$ dielectric annlus ($R_i = 80\% R_o$)

Appendix K

Theoretical and Simulated Equilibrium Concentrations

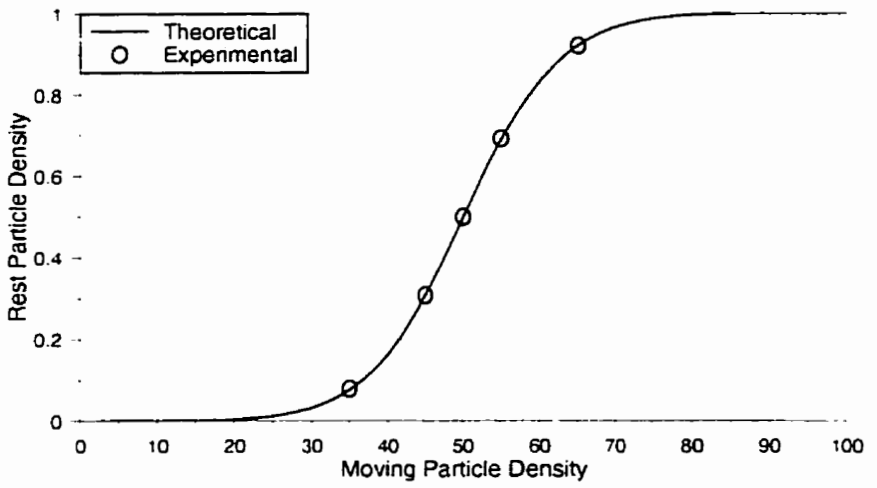

Figure K.1: One Rest Particle Intialization (Mass = $4m$)

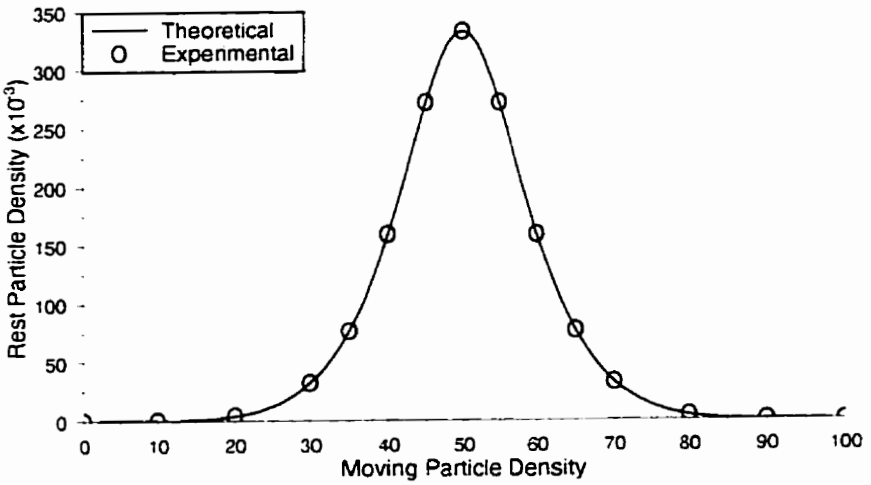

Figure K.2: Two Rest Particle Intialization (Mass = $4m$)

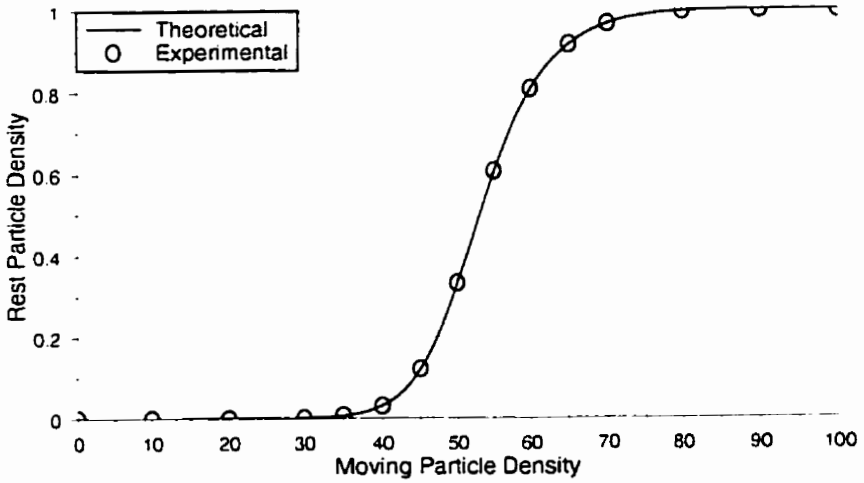

Figure K.3: Two Rest Particle Intialization (Mass = $8m$)

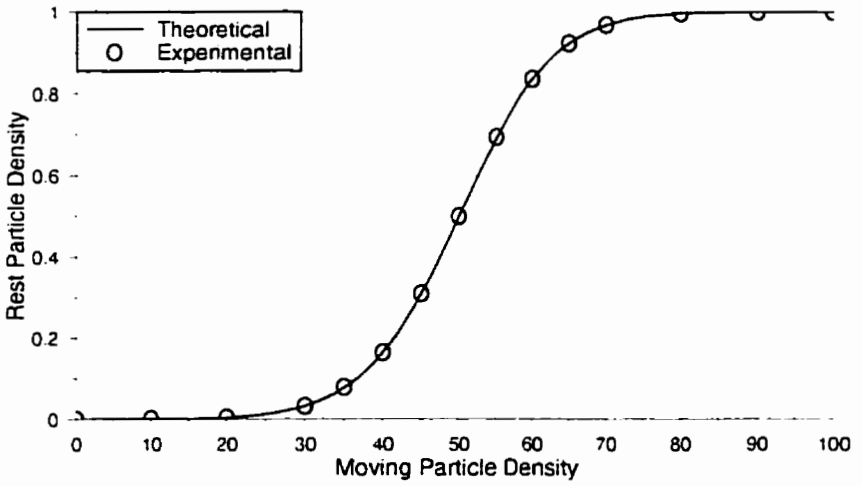

Figure K.4: Three Rest Particle Intialization (Mass = $4m$)

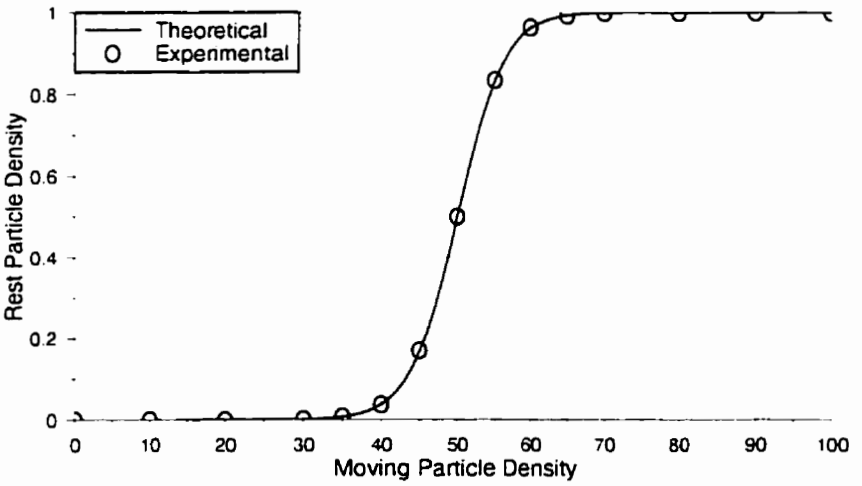

Figure K.5: Three Rest Particle Intialization (Mass = $8m$)

References

[1] Norman Margolus. CAM-8: A computer architechture based on cellular automata. Technical report. MIT Laboratory For Computer Science. Cambridge Massachusetts. December 1993.

[2] Bruce Smith. *Cellular Automata Methods in Mathematical Physics.* PhD thesis. MIT. 1994.

[3] Neil Simons. Michel Cuhaci. Nikhil Adnani. and Greg Bridges. On the potential use of cellular automata machines for electromagnetic field solution. *International Journal of Numerical Modeling : Electric Networks. Devices and Fields.* volume 8: pages 301 -312. 1995.

[4] Karl S. Kunz and Raymond Luebbers. *The finite difference time domain method for electromagnetics.* CRC Press. 1993.

[5] Christos Christopoulos. *Transmission-line modeling method: TLM.* IEEE/OUP Series on Electromagnetic Wave Theory. IEEE Press in assiciation with Oxford University Press. 1995.

[6] J Hardy. O de Pazzis. and Y Pomeau. Molecular dynamics of a classical lattice gas: Transport properties and time correlation functions. *Phys. Rev.* A. pages 1949–1961. 1976.

[7] Nikhil Adnani. Cellular automata models for the two dimensional scalar wave equation. MSc thesis. Electrical engineering. University of Manitoba. Winnipeg. Manitoba. May 1996.

[8] M. Hénon. On the relation between lattice gases and cellular automata. In R. Monaco. editor. *Discrete Kinetic Theory. Lattice Gas Dynamics and Foundations of Hydrodynamics.* pages 160-161. Torino. Italy. September 1988. Institue for Scientific Interchange. World Scientific.

[9] Neil Simons. *Development and Application of Differential-Equation Based Numerical Techniques to Electromagnetic Scattering and Radiation Problems.* PhD thesis. Univeristy of Manitoba. 1994.

[10] Stephen Wolfram. Cellular automaton fluids 1: Basic theory. In Gary D. Doolen. editor. *Lattice Gas Methods for Partial Differential Equations.* Santa Fe Institute Studies In The Science of Complexity. pages 19–73. Addison-Wesley Publishing Company. 1990.

[11] Uriel Frisch. Brosl Hasslacher. and Yves Pomeau. Lattice-gas automata for the navier-stokes equation. *Phys. Rev. Letters.* volume 56: pages 1505-1508. 1986.

[12] K. U. Ingard. *Fundamentals of Waves and Oscillations.* chapter 12. pages 343-365. Cambridge University Press. 1988.

[13] Stephen Wolfram and James Salem. Thermodynamics and hydrodynamics of cellular automata. In *Cellular Automata and Complexity: Collected Papers.* part one: primary papers. pages 259-265. Addison-Wesley Publication Company. 1994.

[14] Dominique d'Humieres and Pierre Lallemand. Numerical simulations of hydrodynamics with lattice gas automata in two dimensions. In Doolen et al.. editor.

Lattice Gas Methods for Partial Differential Equations. SFI SISOC. Addison-Wesley Publishing Co., 1990.

[15] Joanne R. Treurniet and Neil R. Simons. Interger lattice gas automata for the numerical solution of electromagnetic problems. Technical Report CRC-RP-98-001. Communications Research Centre. January 1998.

[16] Greg Bridges and Neil Simons. Multi-bit lattice gas automaton for computational electromagnetics. In *URSI Conference Program and Abstracts*. page 266. Montreal. Quebec. August 1997.

[17] G. Bridges. N. Simons. D. Cule. M. Zhang. and M. Cuhaci. Application of the lattice gas automata technique to modelling wave interactions with biological media. In *IEEE International Conference on Antennas and Propagation*. UK. April 1997.

[18] D. Givoli. Non-reflecting boundary conditions. *Journal of Computational Physics*. pages 1-29. 1991.

[19] D. Cule. N.R.S Simons. G.E. Bridges. J. LoVetri. and M. Cuhaci. Investigation of geometrically small features with numerical solutions to electromagnetic field problems. In *ANTEM Conference Proceedings*. pages 223-226. Montreal. Quebec. August 1996. ISBN-0-9692563-5-3.

[20] Michal Okoniewski and Maria Stuchly. A study of the handset antenna and human body interaction. *IEEE Transactions on Microwave Theory and Techniques*. volume 44 (number 10): pages 1855-1863. October 1996.

[21] Volker Hombach. Klaus Meier. Michael Burkhardt. Eberhard Kuhn. and Niels Kuster. The dependence of EM energy absoption upon human head modeling at

900MHz. *IEEE Transactions on Microwave Theory and Techniques*. volume 44: pages 1865–1873. October 1996.

[22] Klaus Meier. Volker Hombach. Ralf Kastle. Roger Yew-Siow Tay. and Niels Kuster. The dependence of electromagnetic energy absorption upon human-head modeling at 1800MHz. *IEEE Transactions on Microwave Theory and Techniques*. volume 45 (number 11): pages 2058–2062. November 1997.

[23] William H. Hayt Jr. *Engineering Electromagnetics*. McGraw-Hill Series in Electrical Engineering. McGraw-Hill Book Company. fifth edition. 1989.

[24] M. A. Stuchly. D. L. Johnson. H. P. Maharaj. D. A. Morison. and P. Neufeld. Limits of exposure to radiofrequency fields at frequencies from 10KHz–300GHz. Safety Codes H46-2/90-160E. Health and Welfare Canada. 1991. Safety Code 6.

[25] Commissioners James H. Quello and Rachelle B. Chong. Guidelines for evaluating the environmental effects of radiofrequency radiation. Technical report. Federal Communications Commision. 1996.

[26] D. Cule. M. Zhang. N. Simons. G. Bridges. and M. Cuhaci. Wave interaction with heterogeneous dielectric objects using lattice gas automata. In *URSI Conference Program and Abstracts*. page 265. Montreal. Quebec. August 1997.

[27] Michal Okoniewski and Kris Caputa. Personal correspondence. February 1996. University of Victoria.

[28] National Library of Medicine. The visible human project. World Wide Web. www.nlm.nih.gov/research/visible/visible_human.html.

[29] Neil Simons and Riaz Suisanshian. Personal Correspondence. July 1997. Communications Research Centre.

[30] Walter D. Glanze Kenneth N. Anderson. Lois E. Anderson. editor. *Dic Mosley's Medical. Nursing & Allied Health Dictionary.* volume 1. 5th edition. 1997.

[31] Om P. Gandhi. Gianluca Lazzi. and Cynthia M. Furse. Electromagnetic absorption in the human head and neck for mobile telephones at 835 and 1900MHz. *IEEE Transactions on Microwave Theory and Techniques.* volume 44 (number 10): pages 1884-1897. October 1996.

[32] N. Adnani. M. Zhang. D. Cule. N. Simons. G. Bridges. and M. Cuhaci. Modeling wave mechanics using lattice gas automata. In *ANTEM Conference Proceedings.* pages 203-210. Montreal. Quebec. August 1996.

[33] M. Zhang. G. Bridges. and N. Simons. A 3D vector model for computational electromagnetics. In *ANTEM Conference Proceedings.* Ottawa. Ontario. August 1998.

[34] Neil Simons. Application of lattice gas automata to the solution of electromagnetic field problems. In *6th International Conference on Discrete Models for Fluid Dynamics.* Boston. Massachusetts. August 1996.

[35] Neil Simons. Greg Bridges. Dino Cule. Ming Zhang. and Michel Cuhaci. Sources of error within lattice gas automata simulation electromagnetic field problems. In *Progress in Applied Computational Electromagnetics Meeting.* volume 2. Monteray. California. 1997.

[36] Micheal Biafore. Notes on CAM-8 forth. Technical report. MIT Laboratory for Computer Science. Cambridge. Massachusetts. 1993.

IMAGE EVALUATION
TEST TARGET (QA-3)

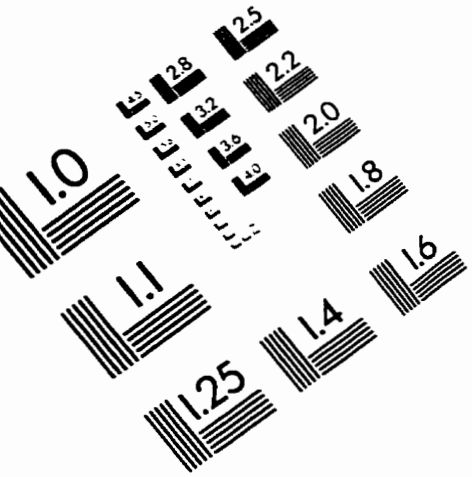

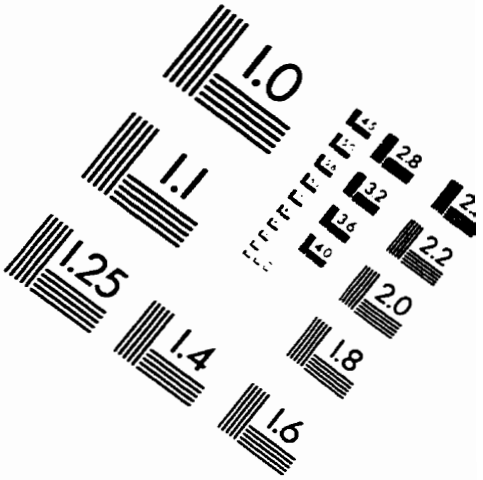

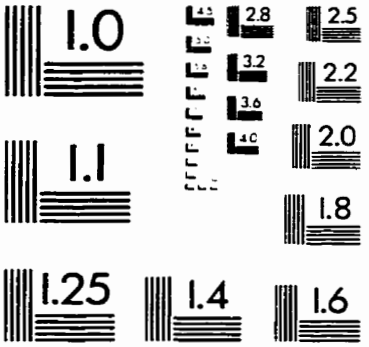

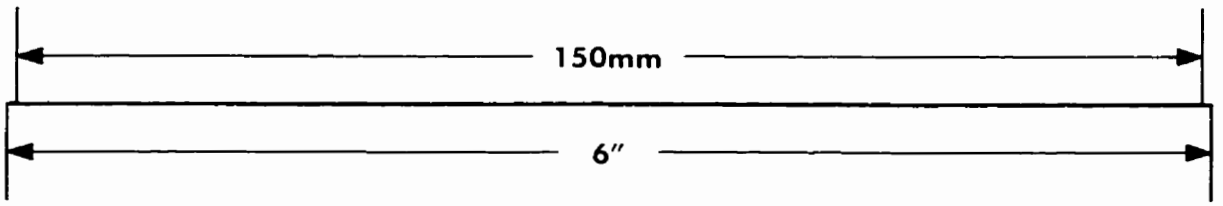

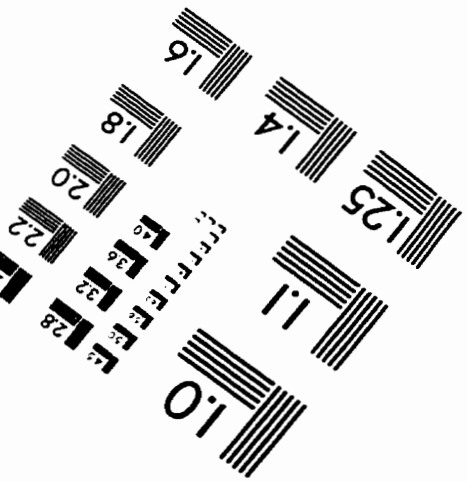

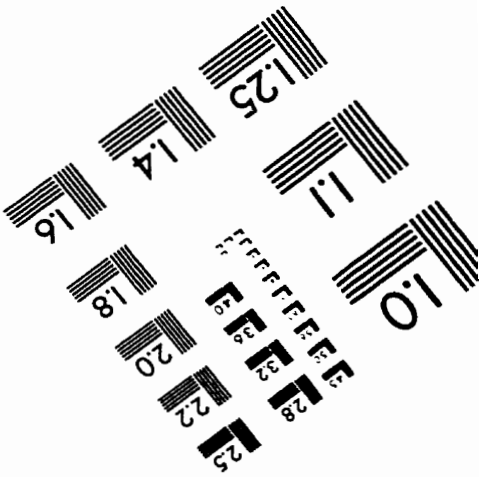

APPLIED IMAGE, Inc
1653 East Main Street
Rochester, NY 14609 USA
Phone: 716/482-0300
Fax: 716/288-5989